UNIVERSITY OF CALIFORNIA
RIVERSIDE

Quantification of Changes of Intensity and Attenuation Coefficient During Neural Activity Using Optical Coherence Tomography

A Dissertation submitted in partial satisfaction
of the requirements for the degree of

Doctor of Philosophy

in

Bioengineering

by

Md. Monirul Hasan

March 2018

Dissertation Committee:
Dr. B. Hyle Park, Chairperson
Dr. Xiaoping Hu
Dr. Joshua Morgan

The Dissertation of Md. Monirul Hasan is approved:

_____

_____

_____

Committee Chairperson

University of California, Riverside

ACKNOWLEDGEMENTS

First, I would like to thank Dr. B. Hyle Park for his guidance in last four and half years. He always encouraged me to explore new ideas and provided valuable suggestions to achieve the positive results. This work would not have been possible without his continued guidance and support.

I would like to thank my dissertation committee members, Dr. Xiaoping Hu and Dr. Joshua Morgan, for their time to review my work and useful feedback. I would also like to thank my oral qualifying committee members, Dr. Maxim Bazhenov, Dr. Devin K. Binder, Dr. Victor G. J. Rodgers, and Dr. Dimitrios Morikis for reviewing my proposal and guiding me to achieve it.

My lab works would not be possible without the support my lab members. I would like to thank my friend Dr. Rezuanul Haque for his support especially during my first year. I was able to grasp fundamental of OCT, Matlab, C++ and other projects work quickly. I would also like to thank Dr. Shahidul Islam for his support on various projects. Dr. Koji Hirota and Minh Tong were great friends, and it was fun to work with you guys especially building the new OCT system. Thank you, Christian Oh, for helping on designing new system. Thank you, Dr. Carissa Rodriguez, for helping me to understand Matlab code. Thank you, Dr. Michael C. Oliveira, Dr. Melissa Eberle, Danielle Ornelas, Junze Liu, Jorge Sanchez, Jason Qiu, Jasmine Shah and Patrick Gregory for your support on different projects. You guys are amazing.

I would like to acknowledge the funding sources that contributed to the work, which includes the NIH R00 EB007241, NIH R01 NS081243, CAL-BRAIN 349329, NIH R21 EY026441 and NIH U01 EY025501 and seed funding from the UCR office of research and development. I would also like to thank the UCR's Earle C. Anthony travel grant to attend SPIE Photonics West conferences.

Last but most importantly, I want to thank my family members who supported me through their advice and prayer from 12000 miles away. I want to thank my mom for inspiring me to start my Ph.D. journey. You were always by my side in my bad or good days. Your guidance helped me to stay on course. Thank you, dad, for your support from far away from me. Nurul mama was always supportive. I would like to thank Tamim, Siraz mama, Soto khala, Boro khala, Nani, and Dadi for keeping me in your prayer. Most importantly, I would like to thank my lovely wife, Zannatul Firdous Bonna for her relentless support. You shared both pain and joy in last 6 years starting from the application for grad school to finish it. Without your support, I could not do my works. Finally, I want to thank Riverside Bangladeshi Community to make my life colorful in America.

Md. Monirul Hasan

Riverside, California

To my dear mom
For lifelong dedication, love, care and support

ABSTRACT OF THE DISSERTATION

Quantification of Changes of Intensity and Attenuation Coefficient During Neural Activity Using Optical Coherence Tomography

by

Md. Monirul Hasan

Doctor of Philosophy, Graduate Program in Bioengineering
University of California, Riverside, March 2018
Dr. B. Hyle Park, Chairperson

The nervous system, which receives information through the electrical signal to coordinate and disseminate information about the body and its environment, is an assembly of neurons. Current methods of detection of neural activity are based on electrophysiology, which requires direct or near direct contact, or fluorescence-based techniques, which require the introduction of reporter molecules, raising a concern of toxicity. Optical coherence tomography(OCT) detects neural activity by taking advantage of intrinsic structural changes that accompany neural activity without any exogenous agents. The phase-resolved OCT detected 10-30 nm swelling of axon during neural activity from the functionally stimulated compound eye of the horseshoe crab(limulus) by utilizing the phase-resolved measurement. There was a decrease of backscattered intensity during propagation of action potential due to change of scattering as well. Further study on in vitro murine brain slice showed the changes of the phase (or thickness change) as well as a decrease of back-reflected intensity during propagation of action potential. Above studies with pr-OCT were performed without scanning because scanning introduced phase noise,

and the desired signal was buried under noise for the signal to noise ratio of 25~30 dB. However, spectral domain OCT was used to capture 3D volumetric intensity images during the neural activity in in vitro seizure mouse model after a period of baseline data. The average intensity of the hippocampal brain slice decreased by 10~18% from baseline during neural activity. Although intensity can separate neural activity from non-neural activity with 97.27% specificity and 97.60% sensitivity, it varies from experiment to experiment. Attenuation coefficient(μ), which quantifies how strongly a sample scatters and absorbs light is a constant for a sample, can solve the problem. During neural activities, there was a 10~15% decrease of μ. For both intensity and μ based method, there was a spatial correlation between optical changes and gold standard electrophysiology. Finally, quantified OCT intensity detected a localized action potential from CA1 of the hippocampal brain slice during ripple activation and -1% intensity threshold separated activity from non-activity.

Table of Contents

List of Figures

Introduction

The nervous system is an assembly of neurons that receives information, analyzes it, and makes decisions. Although neurons are not good inherent conductors of electricity, they generate electrical signals based on flow of ions across their plasma membrane to coordinate, disseminate, and acquire information about the body and its environment. Therefore, understanding neural activity is an important part of neurobiological research. Electrophysiology has been the gold standard for decades for study of neural activity but its resolution and invasiveness limit its applicability for intact brain structures. Multi-electrode arrays or depth-encoded electrodes have limited density and fixed geometries. Fluorescence imaging, although increasingly common in many neural circuits, requires the introduction of reporter molecules into the cells of interest, raising concerns about cellular toxicity. To introduce them in specific location is challenging because of involvement of invasive procedure in most cases, which can limit application of these contrast agents. Samples with genetically-encoded fluorescent markers do not have these limitations. However, genetically modified markers are not readily available for all animal strains and this restricts their application to specific animal models only. The goal of this research is to detect neural activity without exogenous agents using optical coherence tomography(OCT) to take advantage of intrinsic structural changes that accompany neural activity for label-free optical detection and localization of action potential propagation.

This dissertation is organized in six chapters. Chapter 1 introduces OCT in detail. This chapter explains the principle and mathematical representation of OCT, especially

spectral domain OCT (SD-OCT) and phase-resolved SD-OCT. Later, this chapter discusses the applications of OCT in neuroimaging.

Chapter 2 discusses the detection of neural activity using backscattered intensity as a biomarker in in vitro brain slice. During neural activity, intensity decreases from baseline due to change of scattering of the brain tissue. There is a spatial correlation in hippocampal brain slices between OCT intensity and electrophysiology. This method can separate large-scale neural activity from non-neural activity with 97.27% specificity and 97.60% sensitivity.

Chapter 3 refines intensity based approach for detection of neural activity. There is a variation of intensity from experiment to experiment but attenuation coefficient is the properties of tissue, and it is constant for same type of tissue. Therefore, the improved approach is to use attenuation coefficient as a biomarker to detect neural activity. During neural activities, there is a 10~15% decrease of attenuation coefficient. There is a spatial correlation in hippocampus region between % change of attenuation coefficient and electrophysiology. This method can separate large-scale neural activity from non-neural activity with 99.5% specificity and 95% sensitivity.

Chapter 4 discusses the detection of action potential on functionally stimulated optic nerve of compound eye of horseshoe crab. The diameter of the axons of horseshoe crab are on the order of mammalian axons, and pr-SD-OCT can detect swelling of neurons during propagation of action potential. As there is no electrical stimulation, the data is free

from electrical stimulation artifacts. The swelling of axon is in correlation with axon potential propagation.

Chapter 5 focuses on detection of neural activities on faster time scale using phase-resolved measurement of OCT in in vitro murine brain slice. The epileptiform of activity model was used for generation of neural activity, and OCT signals were acquired from one location of the CA3 region of hippocampus. pr-SD-OCT can detect swelling of neurons during propagation of action potential.

Chapter 6 address on the detection of neural activity on localized area of CA1 of hippocampus of murine brain slice for sharp wave ripple. Sharp waves(SPWs) are large amplitude negative wave in CA1 stratum radiatum associated with a fast-oscillatory pattern (110-220 Hz) of the local field potential(LFP) in the CA1 pyramidal layer, known as “ripples”. During ripple propagation, OCT intensity decreases to 2% from baseline, a threshold at -%1 intensity can indicate ripple activation.

The dissertation concludes with a summary of the overall findings of this study and highlights the significant achievements that can lead to future research studies.

Chapter 1: Introduction of Optical Coherence Tomography

1.1.Optical coherence tomography(OCT)

Optical Coherence Tomography, first demonstrated by Huang et. al. in 1991[1], is an emerging optical imaging technique that can capture high resolution, cross-sectional images of microstructure of biological tissues by measuring the magnitude and echo time delay of backscattered light [1]. The basic principle of the OCT system is described below in addition to a brief description of different modalities of this imaging technique.

1.2.Principle of OCT

There are several types of imaging systems now used for different applications [2]. The first-generation OCT system was time domain OCT(TD-OCT). In principle, TD-OCT is analogous to ultrasound imaging. In ultrasound, a sound pulse is directed into a tissue, and the amplitude and echo time delay of the back-reflected sound yields information about different tissue structures due to its varied acoustic properties. In TD-OCT, back-reflected light from tissue structure yields similar information of optical properties. The principle difference in detection schemes between ultrasound and TD-OCT is that the speed of sound is much lower than the speed of light.

TD-OCT is based on low-coherence interferometry, a powerful technique for measuring the magnitude and echo time delay of backscattered light with very high sensitivity. Different versions of low-coherence interferometry were used to study biological tissue non-invasively[3-5]. It uses Michelson interferometer to perform

correlation or interference between light that is backscattered from the tissue and the light that has traveled a known distance or time delay through a reference arm.

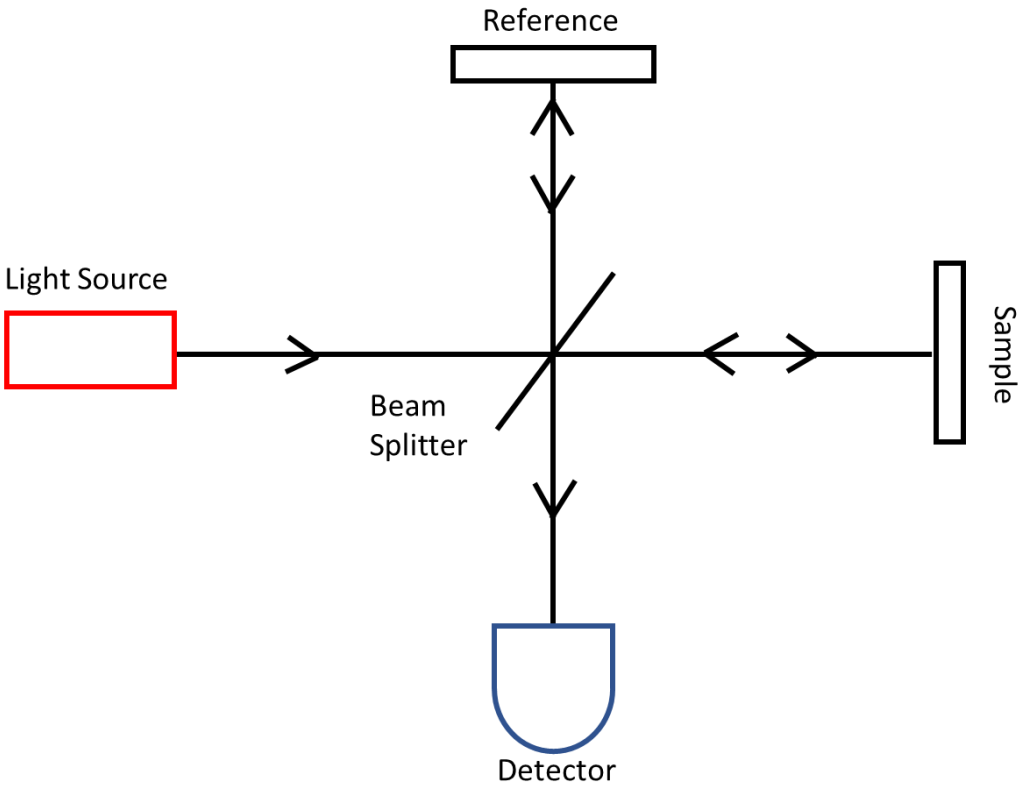

Figure 1.1 Michelson interferometer consist of 4 arms. A light source sends light on beam splitter, which split the light to sample and reference arm, and reflected light from both arms makes interference, which is detected by detector.

Figure 1.1 shows the schematic of a simple Michelson interferometer. An interferometer measures the field of light rather than its intensity. The incident light source is divided into two parts by beam splitter. One part of light travels through a sample arm and the other part onto reference arm. The backscattered light from both sample and reference arms is combined to make interference, and detector measures it.

David Huang and James Fujimoto first developed TD-OCT in 1991 and demonstrated tomographic imaging of peripapillary area of retina and coronary artery[1]. A Michelson interferometer is used as described above, and the interferometric modulation of the output intensity is detected by the photodetector when reference and sample arm delays are nearly matched. The detector output is demodulated to yield an envelope of the interferometric signal, which is then digitized (AD) and stored in computer. These detected interference patterns are used to extract information to produce the structural image of the sample.

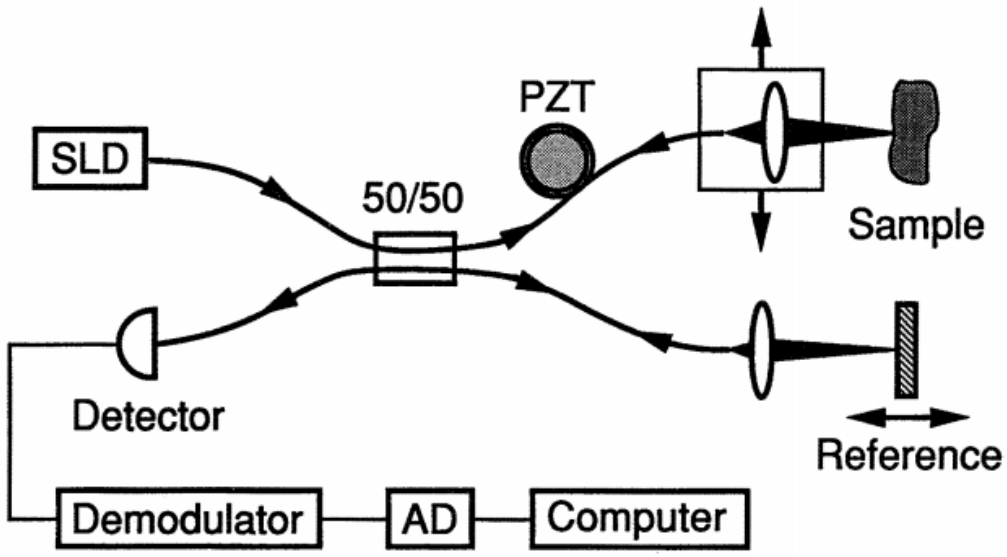

Figure 1.2 Schematic of basic TD-OCT system based on Michelson interferometer [1].

The axial resolution of the system, assuming a Gaussian spectrum, is given by[1]:

$$l_c = \frac{2\ln(2)}{\pi}\frac{\lambda_0^2}{\Delta\lambda}$$

where λ_0 and $\Delta\lambda$ are the central wavelength and the bandwidth respectively. The axial resolution depends on laser properties only. For central wavelength of 804 nm and bandwidth of 170 nm, the axial resolution is 1.67 µm. The lateral resolution depends on the diffraction limited spot size of the focused beam. The diffraction limited minimum spot size is inversely proportional to the numerical aperture of the beam. The lateral resolution is[2]:

$$\Delta x = \frac{4\lambda}{\pi}\frac{f}{d}$$

where d is the spot size of the beam of the objective lens and f is the focal length. Hence, there is no direct connection between axial and lateral resolution. But the lateral resolution is related to depth of field, which is two times the Rayleigh range. The depth of the field(b) is:

$$b = \frac{\pi\,\Delta x^2}{\lambda}$$

Increasing the lateral resolution will decrease the depth of penetration. The second-generation of the OCT system was the spectral domain OCT(SD-OCT).

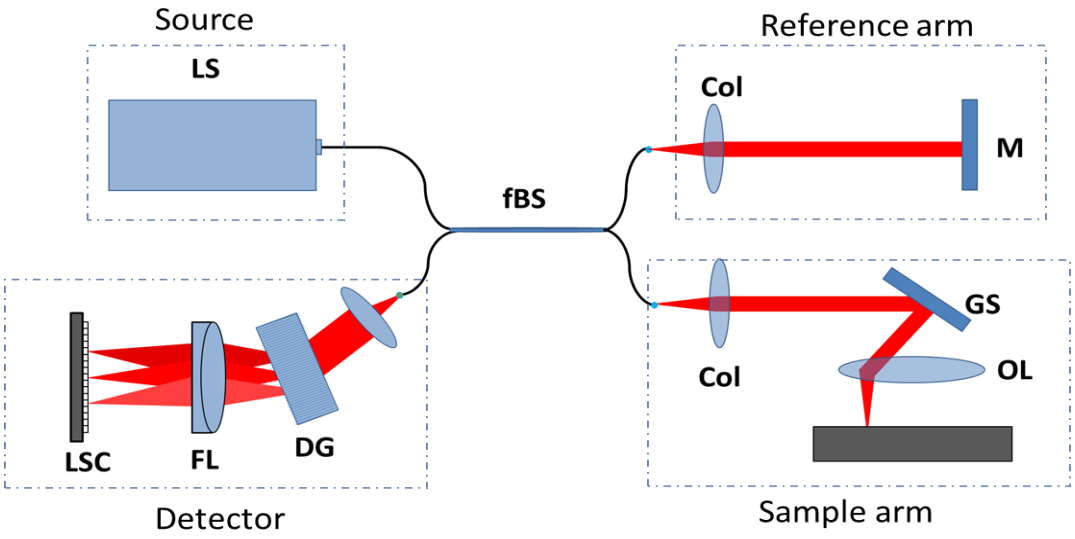

Figure 1.3 Schematic diagram of SD-OCT system. LS: light source, M: mirror, GS: galvo scanner, Col: collimator, OL: objective lens, DG: Diffraction grating, FL: focusing lens, LSC: line scan camera

1.2.1.Spectral domain OCT

SD-OCT was first demonstrated by Fercher et al. in 1995 but advantage of it was not recognized until 2003[6-8]. de Boer et al. reported a SNR gain of several hundredfold in SD-OCT over TD-OCT. Choma et al. reported a sensitivity advantage of 20-30 dB over TD-OCT. R. Leitgeb et al. found a large sensitivity advantage over TD-OCT and achieved more than 80 dB system sensitivity even in low light. There are two important differences between TD-OCT and SD-OCT: reference arm of SD-OCT remains stationary and the interference patterns are dispersed by diffraction grating before detected by charged couple device(CCD). A typical SD-OCT is shown in Figure 1.3 consist of 4 parts. The light is sent to a fiber beam splitter, which splits the light between the reference and sample arms. The sample arm consists of a scanning mirror, which controls the scanning pattern of light. The backscattered light from the reference and sample arm combined in the fiber to make

interference patterns. The detector arm has a diffraction grating, which splits the light by wavelength, then a focusing lens is used to project the light on a line scan camera.

Mathematical expression for OCT

The Michelson interferometer measures the field of light rather than its intensity. The incident light is divided into sample beam E_S and reference beam E_R. The electric field at the output of the interferometer is the sum of the sample and reference fields, $E_S + E_R$, and the detector measures the intensity of the output. The intensity, I_D at the detector can be expressed as[9]:

$$I_D(k,\omega) = \frac{\rho}{2}\langle|E_S + E_R|\rangle^2 \tag{1.1}$$

where ρ represents detector sensitivity, k is the wavenumber ($\frac{2\pi}{\lambda}$) and ω is the angular frequency ($2\pi\upsilon$). Here, λ is the wavelength of the light and υ is the frequency of the light. If the polychromatic plane wave is used as a source for illumination, then incident beam's electric field can be expressed as $E_i = s(k,\omega)e^{i(kz-\omega t)}$. Here, $s(k,\omega)$ is the amplitude of electric field. Assuming the beam splitter's splitting ratio of 0.5, the expression of reference and sample arm can be written in term of incident light as:

$$E_R = \frac{E_i}{\sqrt{2}}\, r_R e^{i2kz_R} \tag{1.2}$$

$$E_S = \frac{E_i}{\sqrt{2}}\left[r_S(z_S) \otimes e^{i2kz_S}\right] \tag{1.3}$$

Here, the distance from beamsplitter to sample to the detector is z_S and beamsplitter to reference arm to the detector is z_R. Note that factor 2 in the exponential term accounts for light traveling roundtrip from beamsplitter, and $\otimes$ represents convolution. In general, the sample beam axis $r_S(z_S)$ is continuous resulting from a continuous varying refractive index of the sample. If we assume a series of N discrete real delta function reflections of the form $r_S(z_S) = \sum_{n=1}^{N} r_{Sn}\,\delta(z_S - z_{Sn})$, each reflection is characterized by its electric field reflectivity $r_{S1}, r_{S2}\ldots\ldots$, and pathlength from the beamsplitter of $z_{S1}, z_{S2}\ldots..$

The equation (1.1) can be rewritten as:

$$I_D(k,\omega) = \frac{\rho}{2}\langle (E_R + E_s)(E_R + E_s)^* \rangle \tag{1.4}$$

For z=0 at the surface of the beamsplitter, and expanding $I_D(k,\omega)$, we find,

$$I_D(k,\omega) = \frac{\rho}{2}\langle \left| \frac{s(k,\omega)}{\sqrt{2}}\, r_R\, e^{i(2kz_R - \omega t)} + \frac{s(k,\omega)}{\sqrt{2}} \sum_{n=1}^{N} r_{Sn}\, e^{i(2kz_{Sn} - \omega t)} \right|^2 \rangle \tag{1.5}$$

Since υ oscillates much faster than the sampling rate of practical detectors, we can eliminate any terms dependent upon angular frequency $\omega = 2\pi\upsilon$ from the expanded form of the equation of (1.5),

$$
\begin{aligned}
I_D(k) = \frac{\rho}{4}[S(k)(R_R + R_{S1} + R_{S2} + \cdots)] \\
&+ \frac{\rho}{4}\left[S(k)\sum_{n=1}^{N}\sqrt{R_R R_{Sn}}\,(e^{i2k(z_R - z_{Sn})} + e^{-i2k(z_R - z_{Sn})})\right] \\
&+ \frac{\rho}{4}\left[S(k)\sum_{n\neq m=1}^{N}\sqrt{R_{Sn}R_{Sm}}\,(e^{i2k(z_{Sn} - z_{Sm})}\right. \\
&\left. + e^{-i2k(z_{Sn} - z_{Sm})})\right]
\end{aligned}
\tag{1.6}
$$

The power spectral of the light source, $S(k) = \langle |s(k,w)|^2 \rangle$. Further simplification of the equation (1.6) results the detector current as a function of wavenumber as:

$$
\begin{aligned}
I_D(k) = \frac{\rho}{4}[S(k)(R_R + R_{S1} + R_{S2} + \cdots \ldots)] \\
&+ \frac{\rho}{2}\left[S(k)\sum_{n=1}^{N}\sqrt{R_R R_{Sn}}\,(\cos[2k(z_R - z_{Sn})])\right] \\
&+ \frac{\rho}{2}\left[S(k)\sum_{n\neq m=1}^{N}\sqrt{R_{Sn}R_{Sm}}\;(\cos[2k(z_{Sn} - z_{Sm})])\right]
\end{aligned}
\tag{1.7}
$$

The first part of the equation (1.7) is independent of the path difference between reference and sample arm referred as “DC terms”. The middle part depends on source wavenumber and pathlength difference between sample and reference arm for each sample reflector. This is the most important part, defined as “Cross-correlation terms”, and proportional to square root of sample reflectivity. The third term represents the interference between different sample reflectors referred as “autocorrelation”.

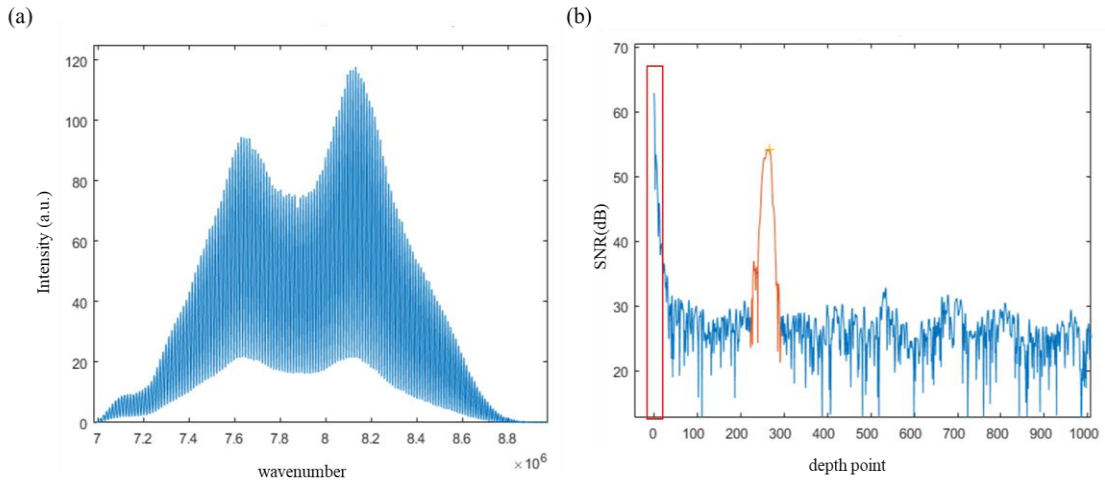

Figure 1.4 Detected spectrum and depth profile from a mirror. (a) detected wavenumber varying spectrum from line scan camera. (b) depth profile. The red box shows the autocorrelation noise at the top of the image.

In SD-OCT, all spectral components of $I_D(k)$ are captured simultaneously by a detector array (Figure 1.2a). Inverse Fourier Transform of $I_D(k)$ provides sample reflectivity profile. The inverse Fourier transform of equation (1.7) calculated as:

$$\begin{aligned} i_D(z) = \frac{\rho}{8}\left[\gamma(z)[R_R + R_{S1} + R_{S2} + \cdots]\right] \\ + \frac{\rho}{4}\left[\gamma(z) \otimes \sum_{n=1}^{N} \sqrt{R_R R_{Sn}}\,(\delta(z \pm 2(z_R - z_{Sn})))\right] \\ + \frac{\rho}{8}\left[\gamma(z) \otimes \sum_{n \neq m=1}^{N} \sqrt{R_{Sn} R_{Sm}}\,(\delta(z \pm 2(z_{Sn} - z_{Sm})))\right] \end{aligned} \tag{1.8}$$

Here, $\gamma(z)$ is the inverse Fourier transform $S(k)$. The first terms of the equation (1.8) are "DC terms" as there is no path length information. The middle terms are the "Cross-correlation terms" which has desired sample filed reflectivity profile $\sqrt{R_S(z_S)} =$

$\sum_{n=1}^{N}\sqrt{R_{Sn}}\,\delta(z_S - z_{Sn})$. The third part is the "auto-correlation terms". Now applying the shifting properties of the delta function during convolution, we get:

$$\begin{aligned} i_D(z) = \frac{\rho}{8}\left[\gamma(z)[R_R + R_{S1} + R_{S2} + \cdots]\right] \\ + \frac{\rho}{4}\sum_{n=1}^{N}\sqrt{R_R R_{Sn}}\left[\gamma[2(z_R - z_{Sn})] + \gamma[-2(z_R - z_{Sn})]\right] \\ + \frac{\rho}{8}\sum_{n\neq m=1}^{N}\sqrt{R_{Sn}R_{Sm}}\left[\gamma[2(z_{Sn} - z_{Sm})]\right. \\ \left. + \gamma[-2(z_{Sn} - z_{Sm})]\right] \end{aligned} \tag{1.9}$$

This is the equation of an "A-scan". Figure 1.4b shows the A-scan (depth profile) of a mirror. This depth profile was generated by removing DC part from the spectrum. The top red box is the auto-correlation noise terms of the image and the mirror is in between depth point 250 and 300.

1.2.2.Phase-resolved OCT

In phase-resolved SD-OCT, the phase variation can be calculated from $I_D(k)$ in equation (1.7). The phase can be calculated as:

$$\varphi(z) = tan^{-1}\left(\frac{Im[i_D(z)]}{re[i_D(z)]}\right) \tag{1.10}$$

This phase can be utilized to detect small thickness change in the sample. The phase has common mode noise which can be eliminated by subtracting phase from two reflecting

points (one point is the reference point at position, z_{ref}, another point is the desired point, z_n). The phase difference at any time, t can be calculated as:

$$\Delta\varphi(z_n) = \varphi(z_n) - \varphi(z_{ref}) \tag{1.11}$$

where depth point, n=1, 2,….

Common mode noise can be eliminated without reference point by subtracting phase of two depth points at time t,

$$\Delta\varphi(z_n) = \varphi(z_n) - \varphi(z_{n-1}) \tag{1.12}$$

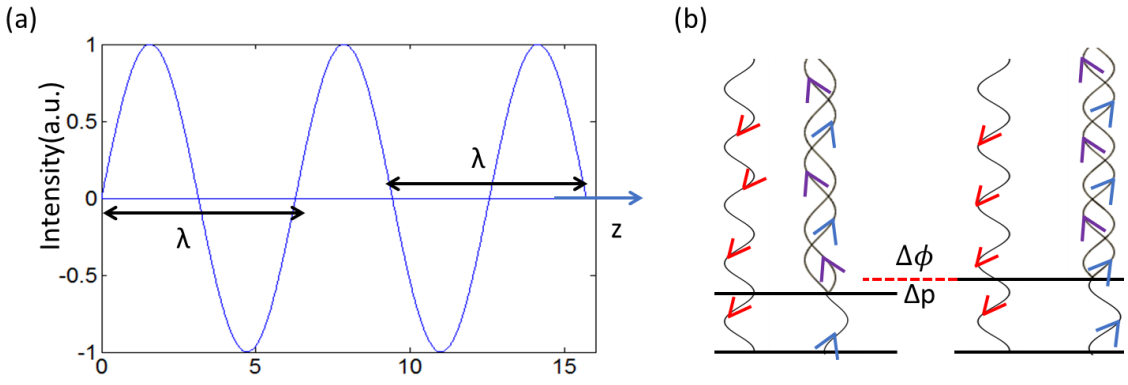

Figure 1.5 Relation between phase difference and path difference. (a) A wave changes phase of 2π after passing a distance equal to its wavelength, λ. (b) for a phase difference of Δϕ, light beam crosses a path difference of 2Δp for the OCT system

The phase difference can be converted to path difference. If a wave is moving along the x-axis, then it changes by a phase of 2π for path changes of λ (Figure 1.5a). Hence, for $\Delta\varphi$ phase difference, the path difference Δp can be found by:

$$\Delta p = \frac{\lambda}{2\pi}\Delta\varphi \tag{1.13}$$

For phase-resolved OCT, light reaches to a depth position of a sample, and return i.e. it crosses twice path length for a phase difference (Figure 1.5b). Hence, path difference or the thickness change of a sample can be calculated as:

$$\Delta p = \frac{\lambda}{4\pi}\Delta\varphi \tag{1.14}$$

The fundamental limitation of detection of minimum thickness change arise from signal-to-noise ratio(SNR) of a measurement. For a shot noise limited system, noise can be modeled as a random vector, and the minimum detectable phase difference[10, 11] is given by:

$$\sigma_{\Delta\varphi} = \frac{1}{\sqrt{SNR}} \tag{1.15}$$

For high SNR, the system is more sensitive to detect thickness change.

1.3.Applications of OCT

Since 1991, OCT has been using as a major imaging system in the research of various fields such as ophthalmology[12-30], neuroimaging[31, 32], cardiology[17, 33-37], dental imaging[38-43], dermatology[14, 44-47], developmental biology[48, 49], tissue engineering[50-53], nanodevices[27, 49, 54], materials[55-59] etc. OCT is a point scanning based imaging system but can acquire cross-sectional imaging by scanning in other direction. It can also acquire video rate imaging from tissue[14, 60-64], thus it has potential applications where real-time imaging is required.

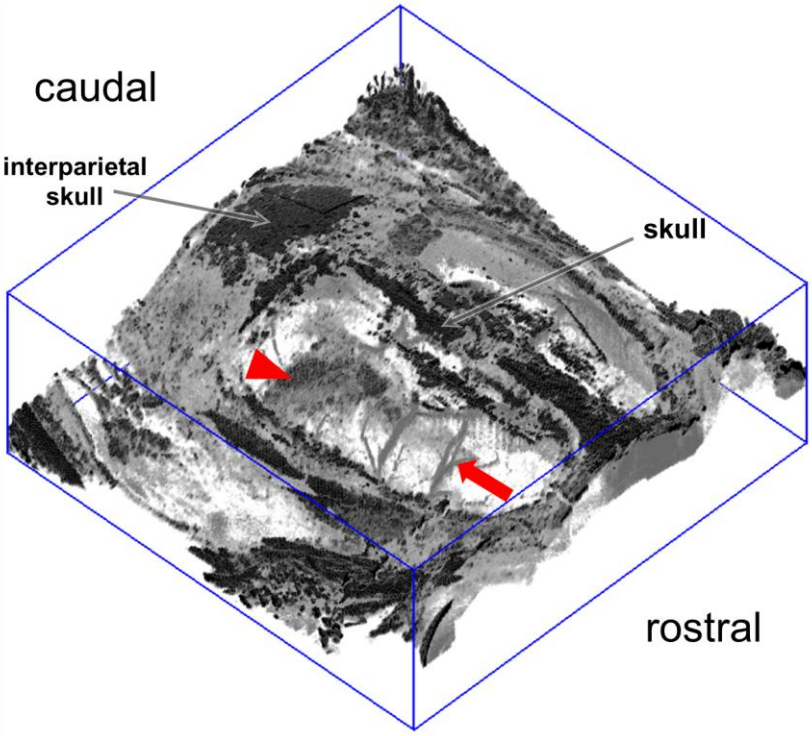

Figure 1.6 The blood vessels in mouse brain. The red arrow indicates the cerebral blood vessels and the arrow head indicates corpus callosum.

OCT for neuroimaging

Current methods of detection of neural activities are fluorescence microscopy[22, 65-68], fMRI[69-73], CT-scan[74], PET-scan[75-77]. Although they are excellent in detecting neural activity, they lack spatial resolution and require dyes. Although electrophysiology is the gold standard to detect neural activity, it is inherently invasive, lacks spatial resolution[78-83].

Optical imaging techniques such as diffuse optical tomography(DOT)[51, 84, 85], intrinsic optical imaging (IOS) [45, 86-88], photoacoustic tomography and microscopy[49, 89], spatial frequency domain imaging(SFDI) [90, 91]overcame these limitations by achieving high resolution and they were minimally invasive.

Optical coherence tomography is a non-invasive imaging technique, which can acquire 3D volumetric images (Figure 1.6). OCT can detect neural activity by quantifying changes of backscattered intensity [92-95]and phase[16, 96-100].It is a promising tool to investigate the neural activity of the brain *in vitro* [101-104].

1.4.Conclusion

OCT, an interferometry-based imaging tool, utilizes light to acquire cross-sectional image. The first-generation TD-OCT uses moving reference arm but the second-generation SD-OCT does not require moving reference arm, instead detect wavelength varying spectrum. OCT is utilized to diagnose different diseases, especially in ophthalmology. It is also used in neuroimaging to detect neural activity both *in vitro* and *in vivo* animal model.

Chapter 2:Non-contact detection of neural activity during seizure activation in mouse hippocampus using backscattered intensity of Optical Coherence Tomography

2.1. Introduction

This chapter describes the detection of neural activity optically using OCT. An *in vitro* murine brain slice model was used to generate large-scale neural activity (epilepsy), and OCT intensity quantified the optical changes during the propagation of neural activity.

Epilepsy is characterized by recurrent and unpredictable interruption of normal brain function due to abnormal excessive or synchronous neuronal activity, called epileptic seizure[105, 106]. Electro-encephalography(EEG) signals have been used to detect epilepsy for many years, which is inherently invasive with low spatial resolution, minimal depth discrimination and high susceptibility to electrical noise[107-109].Functional magnetic resonance imaging has been used to detect the seizure based on blood-oxygen-level dependent (BOLD) signal, but have the limitation with regard to resolution, acquisition speed, and specificity[110-112]. Optical imaging techniques such as diffuse optical coherence tomography(DOT)[51, 84, 113], intrinsic optical signal (IOS)[114-116] overcome these limitations and can detect neuronal activity during seizure activation through changes of intrinsic optical properties.

Optical coherence tomography(OCT) is a label-free, non-contact based imaging techniques, which can acquire depth-resolved images[117-120]. OCT has been shown to be a promising method for *in vitro* imaging in highly scattering tissues[121]. In this study,

we demonstrate that changes in optical properties of murine brain tissue during neural activities can be detected using SD-OCT by inducing a burst of neural activities, measuring backscattered intensity from the tissue over time, quantifying these changes, and validating by correlating with electrophysiology.

2.2.Materials and methods

2.2.1.Animals

All experiments and procedures were performed according to University of California, Riverside Institutional Animal Care and Use Committee-approved protocols. Wild-type (Jackson Laboratory, C57BL/6J, stock number 000664) mouse colonies were bred and maintained in house to generate pups for this study. Both male and female mice were used in this study.

2.2.2.Murine brain slice preparation

Postnatal day (P) 15-30 mice were anesthetized with isoflurane and quickly decapitated. The brain was rapidly removed and submerged in ice-cold, low [Ca^{2+}], high sucrose dissecting solution with carbogen (95%-5% O_2-CO_2) gas continuously applied. A 300 μm thick horizontal whole brain slices were made in the dissection solution with a Leica 1200S vibratome. Slices containing hippocampus were recovered in oxygenated normal ACSF for an hour at 32°C and stored at room temperature until use for imaging. The standard dissecting solution contained (in mM): 87 NaCl, 2.5 KCl, 25 $NaHCO_3$, 1.25 NaH_2PO_4, 4 $MgCl_2$, 0.5 $CaCl_2$, 10 D-glucose, 75 sucrose. Solution maintained at pH 7.4

by continuous oxygenation with carbogen gas mixture. All chemicals were obtained though Fisher Scientific unless otherwise specified.

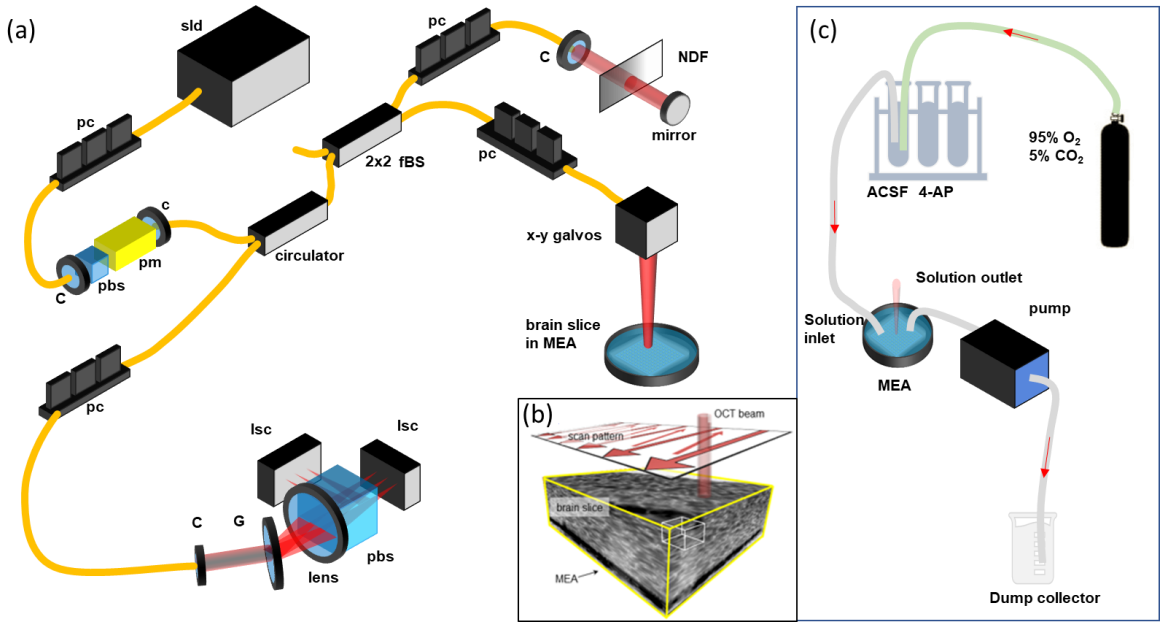

Figure 2.1 System diagram. (a) sld: superluminescent diode MEA: multi-electrode array, pc: polarization controller, pm: polarization modulator, G: grating, NDF: neutral density filter, lsc: line scan camera, C: collimator, pbs: polarization beam splitter, fBS: fiber beamsplitter. (b) OCT beam scanning pattern to acquire volumetric images. (c)Flow of carbogen mixed solution into brain slice.4-AP:4-aminopyridine, ACSF: artificial cerebrospinal fluid.

2.2.3.Imaging system

The SD-OCT system (Figure 2.1a) utilized broadband, low-coherence light source consisting of two superluminescent diodes (SLD), one centered at 1295 nm with a FWHM bandwidth of 97 nm (Thorlab Inc), and the other centered at 1350 nm with a FWHM bandwidth of 48 nm (Denselight Semiconductor Pte Ltd) resulting a combined bandwidth of 120 nm centered at 1298 nm. The system resolution was 8 μm and 20 μm axially and

laterally, respectively. The source was connected to a circulator, which was then connected to a 2x2 fiber-based beam splitter that split 90% of the light to the sample arm and 10% of the light to the reference arm. In the sample arm, a pair of galvanometer (Thorlab Inc) mirrors provided transverse scanning of the collimated beam. A lens (AC254-050-C, Thorlab) with the diameter of 1 inch and focal length of 50 mm was used to direct and collect backscatter light from the sample. The backscattered light from reference and sample arm were collected by a custom-built spectrometer. The spectrometer consists of a diffraction grating (Wasatch Photonics, 1100 lpmm), a focusing lens (JenOptik Optical Systems, f=150 mm), polarization beam splitter cube (Rocky Mountain Instrument Co., 4-inch Cube) and two 1024 pixels line scan cameras (Goodrich SUI SU-LDH linear digital high-speed InGaAs camera).

2.2.4.Data acquisition and processing for OCT and Electrophysiology

Both OCT and electrophysiology data were recorded simultaneously for hippocampal area of murine brain slice.

2.2.4.1.OCT data acquisition and processing

OCT volumetric data was acquired at the A-line rate of 15 kHz, and a single volume has 100 cross-sectional images composed of 1024 A-lines (Figure 2.1b). Acquisition time for each volume was 12 s. An imaging depth of 2 mm was obtained with 6.5 mW of incident power on brain slice. To have uniform wavenumber spacing, linear interpolation was performed to the nonlinear k-space sampled spectral data. The fast Fourier-transformation(FFT) from wavenumber to the spatial domain was performed, and depth-

resolved structural information was retrieved. In spectrometer based OCT, the sensitivity of the system decreases as a function of depth due to the finite resolution of the spectrometer. Because of this, a correction was applied by multiplying each A-line by a calculated correction curve to compensate for the decrease of sensitivity as a function of depth [120]. The correction curve was calculated from the equation:

$$R(z) = (\frac{\sin\zeta}{\zeta})^2 * e^{\left[-\frac{w^2}{2ln2}\zeta^2\right]} \quad (2.1)$$

where $\zeta = \left(\frac{\pi}{2}\right) * (\frac{z}{z_{RD}})$ is the depth normalized to the maximum depth, $z_{RD} = \lambda^2/4\Delta\lambda$ where $\Delta\lambda$ is the wavelength spacing between pixels, and $w = \delta\lambda/\Delta\lambda$ where $\delta\lambda$ is the spectrometer's spectral resolution(FWHM). The spectrometer drop-off from the mirror sample was 11 dB, and equation 2.1 was used to fit the drop-off and calculated the correction curve. By applying correction curve, it was ensured that any change of intensity during neural activity was from the tissue under investigation.

The noise for each A-line was different due to reflection from the multi-electrode array for some of the A-lines and generated by averaging intensity of 20 pixels above brain slice and 50 pixels below MEA. A noise-free A-line was obtained by subtracting noise from each A-line. A median filter of size 70 x 70 μm was applied to minimize variation due to coherence speckle. Kernel size was determined by applying a filter on cross-sectional images to achieve speckle contrast ratio (K_s) below 0.1 over a uniform slice of tissue.

$$K_s = \frac{\sigma_s}{\langle I \rangle} \tag{2.2}$$

where σ_s is the standard deviation and $\langle I \rangle$ is the mean intensity. Therefore, lower the σ_s, the smaller the speckle contrast ratio.

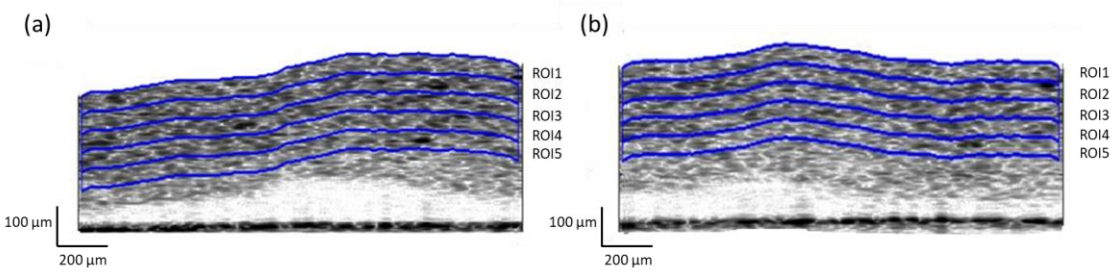

Figure 2.2 Cross-sectional image of murine brain slice. (a) Cross-sectional image of slice during control experiments. Brain slice is segmented in 5 regions of interests(ROIs). (b) Cross-sectional image of slice during epileptiform activity which are also segmented in 5 ROIs

The top and bottom surfaces of the brain slice were detected by SNR thresholding of 80 dB, and an *en face* intensity image was generated by averaging whole volume in the axial direction. Lateral motion was measured by cross-correlation of reference *en face* image from baseline with all other *en face* images, and correction was applied to all other volumes with respect to reference volume. Each volume was segmented (Figure 2.2) in different layers with 50 µm height, and volume of each layer was 2000 x 2000 x 50 μm^3. The average intensity of each layer was calculated for different datasets. Percentage intensity change from baseline was also calculated for each layer. Standard deviation(σ) was calculated for time t for all data sets of control experiment with ACSF only or epileptiform activity experiment with ACSF and 4-AP. Percentage change of intensity time was plotted with additional indications of 1.5σ above and below the mean intensity.

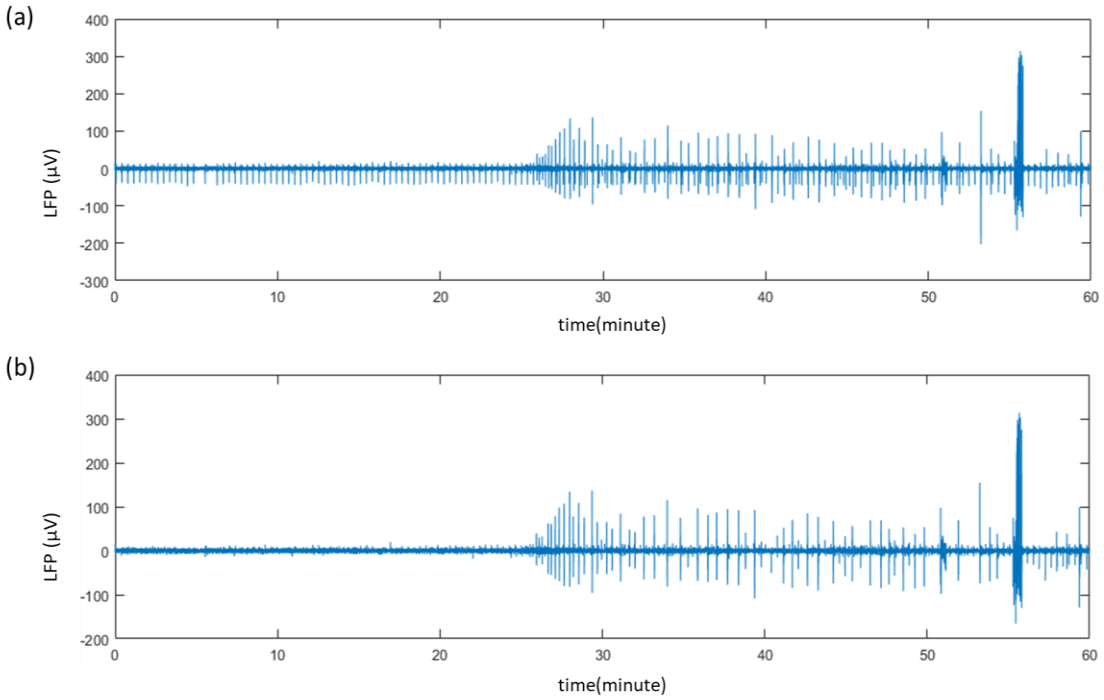

Figure 2.3 OCT beam artifact on LFP trace. (a) Before removal of noise, there were periodic spikes for OCT beam movement on reflective electrode. (b) After removal of noise.

2.2.4.2.Electrophysiology data acquisition and processing

Multielectrode array (MEA) recordings were performed on a 60-channel optically clear array (60pMEA200/30-Ti) with a low-noise amplifier (MEA1060-BC) from MultiChannel Systems. Hippocampal slices were prepared, as described in 2.2.2, placed on the array, and positioned such that the CA1, CA3, and dentate gyrus (DG) were centered over the recording electrodes. Brain slices were continuously perfused during baseline recordings with ACSF (4 ml/min flow rate) containing (in mM): 125 NaCl, 2.5 KCl, 25 NaHCO3, 1.25 NaH2PO4, 1 MgCl2, 2 CaCl2, 25 D-glucose, 10 sucrose (Figure 2.1c). Experiments consisted of an initial 20 minutes of ACSF control followed by ACSF mixed

with 100 µM 4-AP. All MEA recordings were performed at 32°C, which was sufficient to generate stable epileptiform activity.

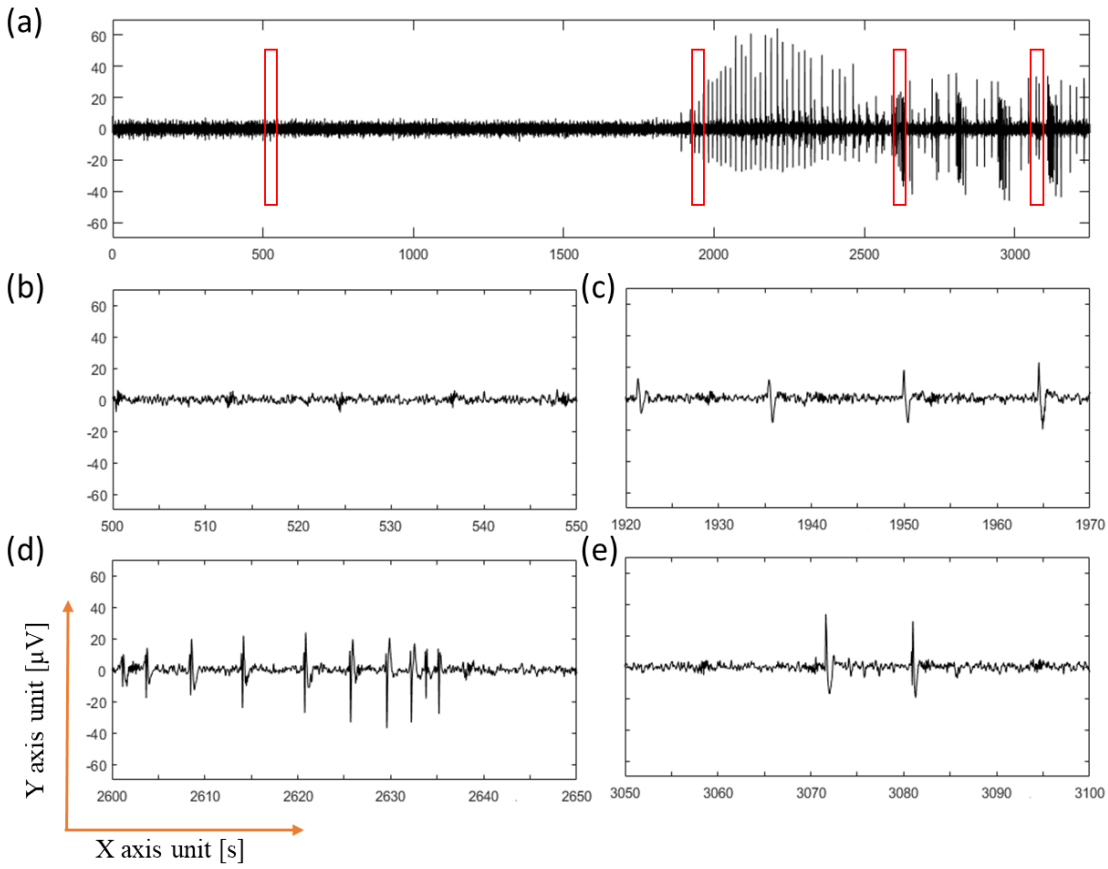

Figure 2.4 LFP trace of single MEA channel. (a) LFP time trace of an epileptiform activity experiment. (b)During baseline with ACSF, there was no spikes greater than 10 µV. (c) The amplitude of burst increased during baseline to pre-seizure period. (d) During epileptiform activity with high firing rate of activities. (e) Epileptiform activity with low firing rate.

Local field potential(LFP) were acquired using MC Rack software (MultiChannel Systems) and exported to MATLAB (MathWorks) for further processing. Data from all 60 MEA channels were collected at 10 kHz. Bandpass (0.1 - 7 Hz) 2nd order Butterworth filter was applied to remove OCT-induced electrical noise (Figure 2.3). The built-in Hilbert

Matlab function was used to compute the Hilbert power(HP) of the bandpass filtered data (Figure 2.4). The HP was then averaged across all channels for 22 seconds bin to compute the correlation between the MEA and OCT data.

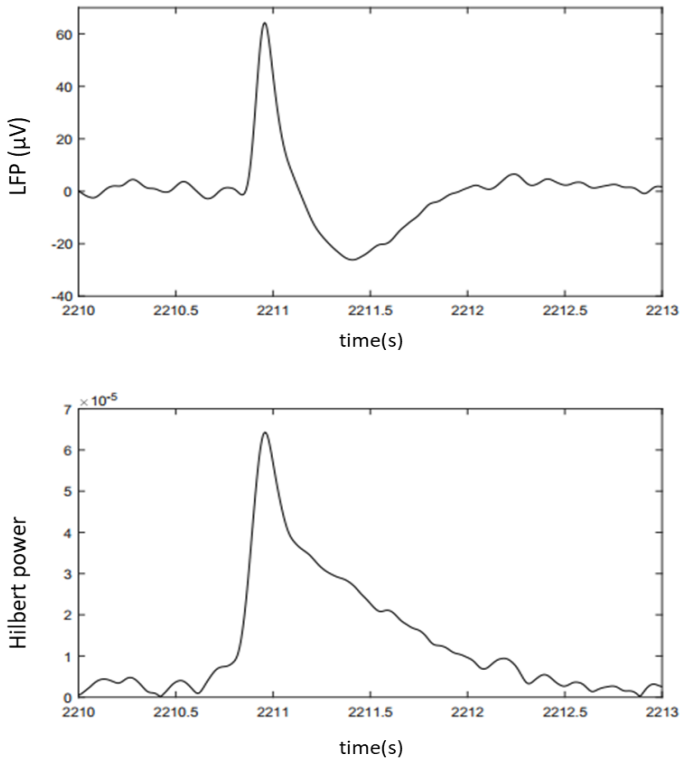

Figure 2.5 Single burst of LFP and corresponding Hilbert power. The duration of LFP was 1.2s.

We used optically clear array (to minimize the reflection from OCT beam) to collect LFP information, which had no mechanism to attach the slice with the surface of the MEA (perforated MEA has suction mechanism to attach the slice with MEA electrodes). An anchor was used to hold the slice with MEA (Figure 2.6c), and its position was different in different experiments. Therefore, there were an unequal distance from the MEA surface and the bottom of the brain slice among experiments. The amplitude of the LFP depends

on the distance between MEA and brain slice as well as the intensity of the neural activity. Due to the distance mismatch among experiments, the LFP were different even in baseline (see Figure 2.6a). Therefore, a correction was required to match the baseline otherwise the standard deviation among experiment will be high even in baseline, and average time trace will not be reliable because of different offset in baseline.

In order to compare results across different experiments, all experimental data were normalized with respect to a baseline (black trace of Figure 2.6a was selected as a baseline). Figure 2.6b shows the result after normalization. Baseline of all data are in the same offset level.

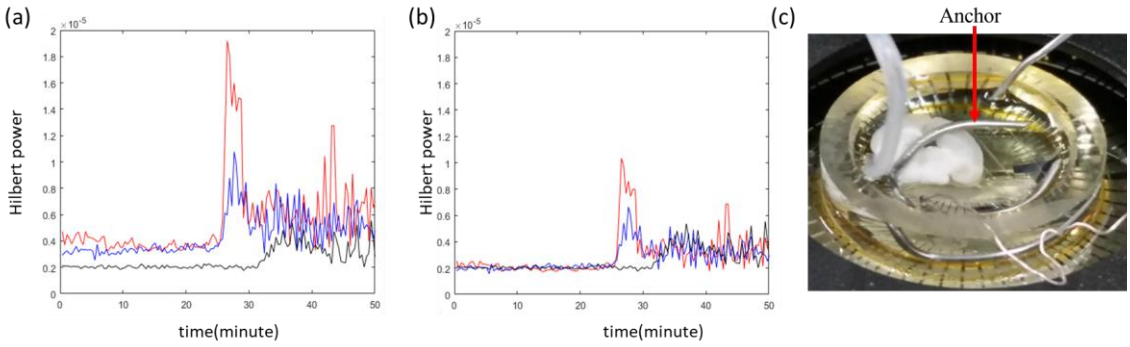

Figure 2.6 Normalization of Hilbert power. (a) before normalization (b) after normalization with respect to reference trace (black Hilbert trace). (c) MEA with brain slice.

2.3.Results and Discussions

Epileptiform activity induced by introducing 4-AP solution into brain slice after acquiring data for the baseline using ACSF solution and optical intensity was compared with the baseline to 4-AP. The OCT cross-sectional images were acquired by sending an

optical beam through ACSF and 4-AP solution, and the composition of ACSF and 4-AP were different. If the composition of the media is different, then their refractive index is different, that will impact on backscattered light. To demonstrate the effect of the 4-AP solution on backscattered light, a control experiment was performed on the dead slice, first, by acquiring baseline data with ACSF, then with the 4-AP solution. Then, other sets of control experiment were performed by acquiring data for full experiment period with ACSF only. Finally, experiments were performed by acquiring the baseline data for 20 minutes, then neural activity induced data for another 40~45 minutes. The results were compared between top layer(ROI1), which were composed non-connected axons, and bottom layers (ROI5, the active region of the slice, and nearest to the electrodes in MEA).

2.3.1.Control experiment with dead slice to demonstrate the effect of 4-AP on backscattered light

Brain slice is kept in un-oxygenated ACSF solution so that cells lose their capability to induce neural activity. Then OCT images were acquired for 20 minutes by flowing ACSF solution into brain slice. Then, the tube was switched from ACSF to the 4-AP solution beaker (Figure 2.1c), and it took 4 minutes for the 4-AP solution to reach into the brain slice. From 25^{th} minute, the 4-AP solution flowed in dead brain slice, and data was acquired until slice deformed.

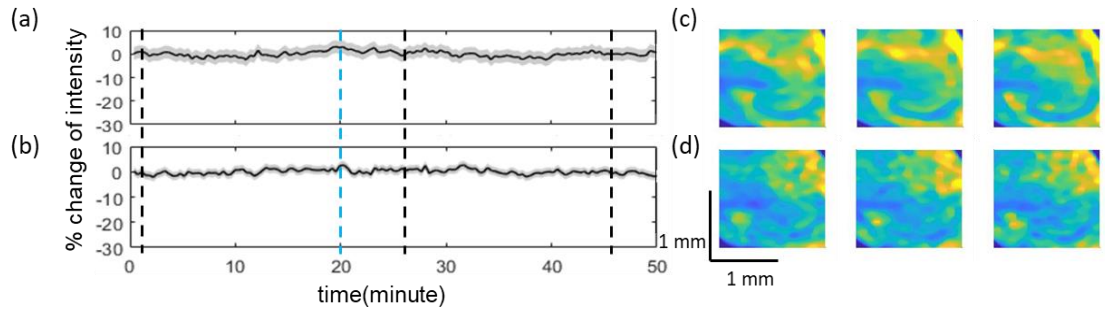

Figure 2.7 Effect of 4-AP on backscattered intensity. (a) The time trace of intensity of a dead slice on top layer. The gray bar indicates the standard deviation(±1.5σ). (b) The time trace of intensity of a dead slice on bottom layer. The gray bar indicates the standard deviation(±1.5σ). For both time trace, intensity trend before 4-AP introduction and after 4-Ap introduction are similar. No change of intensity in heatmap (c-d) at baseline (1st minute), after introduction of 4-AP (27th minute), and 46th minute.

Data was processed according to section 2.2.4.1, and an intensity time trace was generated for entire experiment (Figure 2.7a) for the top and bottom layer. The standard deviation across experiments was calculated, and shaded gray was drawn for ±1.5σ from each time trace. The variation of intensity before and after the 4-AP was similar (Figure 2.7a-b). This demonstrated that there was no significant effect of the 4-AP solution on backscattered light. Any change of OCT intensity during epileptiform activity induced by the 4-AP originated from the scattering change of the tissue for neural activities.

The *en face* heatmap on the different time point of data acquisition demonstrated that there were no significant changes of OCT intensity (Figure 2.7c-d) in CA1, CA3 or DG areas in the hippocampus for the top and the bottom layer of the brain slice.

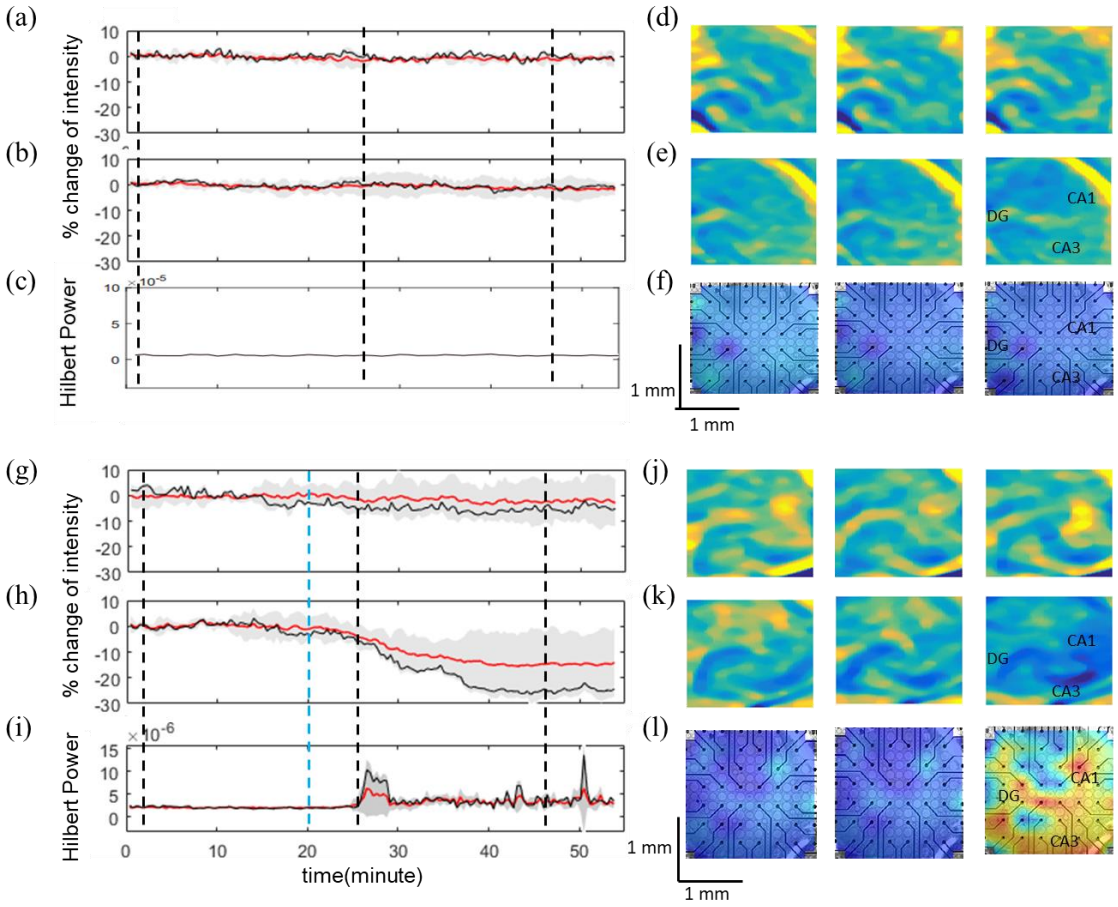

Figure 2.8 Intensity decreases during epileptiform activity. (a-b) The time trace of intensity, the red line is the mean intensity for all experiments, and black line is the intensity for which heatmap is generated in (d-e). The gray shaded area is the ±1.5σ area from mean intensity. The intensity fluctuates less than ±5% for both top(a) and bottom layer(b) layer. There is no change of Hilbert power in (c). The heatmap of d-f demonstrated similar trends of time trace (vertical black lines indicate the time of heatmap). The intensity does not change after 4-AP introduction on top layer(g) as most of the tissue was dead. The average intensity (red line) of all experiment fluctuates between ±5%. But bottom layer (h), where tissue was active, after introduction of 4-AP resulted decrease of intensity by 10~18%. The time trace of Hilbert power also correlated with OCT intensity decrease. The heatmap (k-l) demonstrated the decrease of intensity in CA1, CA3 and DG area in bottom layer from baseline corresponds to increase of Hilbert power but the intensity does not change in top layer(j).

2.3.2.Control experiment with ACSF

The control experiment with ACSF solution only was performed to demonstrate the impact of ACSF on backscattered light. ACSF solution flowed into brain slice placed on MEA about an hour, and both OCT and electrophysiology data were recorded simultaneously. The data was processed according to section 2.2.4.1, and the result showed in Figure 2.8a-e. The top layer was mostly dead tissue because of the local trauma from the vibratome. So, there should not be any activities. In OCT time trace (Figure 2.8a), intensity fluctuated between ±5%, which was like bottom layer (Figure 2.8b), where tissue was active. The Hilbert power was also not changing (Figure 2.8c) over time.

Heatmaps were also generated (Figure 2.8d-f), at 1st, 25th and 45th minute. There were no significant changes in OCT intensity in CA1, CA3 or DG areas in the hippocampus for the top layer of brain slice. A similar trend was found for the bottom layer of brain slice, and has qualitative similarity to that seen in a corresponding electrophysiology heatmap generated from MEA data.

2.3.3.Induction of epileptiform activity

ACSF solution was flowed for 25 minutes, then the 4-AP solution was introduced to induce epileptiform activity. OCT images and MEA signal were recorded for 3 different mice. All experimental data was aligned based on the initiation of seizure. The time trace of OCT intensity and Hilbert power was shown in (Figure 2.8g-i). The trend of intensity at the top layer (Figure 2.8g) was like the top layer of the dead slice (Figure 2.7a) or ACSF

control (Figure 2.8a). However, there was a 10 to 18% decrease of OCT intensity (Figure 2.8h) during epileptiform activity indicated by an increase of Hilbert power (Figure 2.8i).

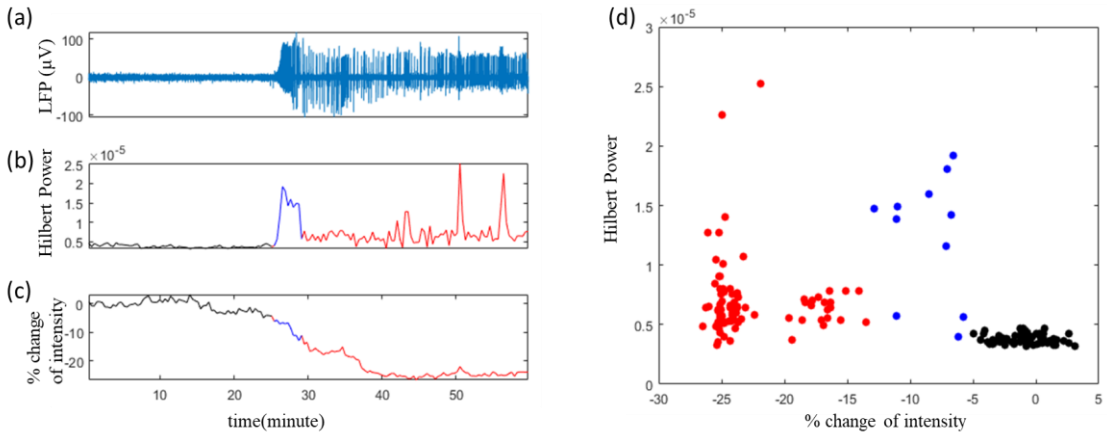

Figure 2.9 Correlation between OCT and mean Hilbert power. (a) LFP time trace. (b) Mean Hilbert power for a 22 seconds bin. (c) OCT intensity trace for active bottom layer of an epileptiform experiment. (d) correlation between % change of intensity and mean Hilbert power. The black, blue and red dot represent corresponding data of b & c in similar color.

Heatmaps were also generated at 1st, 25th and 45th minutes. There were no significant changes in OCT intensity (Figure 2.8j) in CA1, CA3 or DG areas in the hippocampus for the top layer of brain slice. However, there were changes in OCT intensity in CA1, CA3 or DG area of the hippocampus of the bottom layer of brain slice (Figure 2.8k), which also spatially correlated with electrophysiology (Figure 2.8l).

2.3.4.Correlation between OCT and Electrophysiology

The correlation was calculated between OCT intensity trends and Hilbert power. To match with OCT data, Hilbert power was segmented into 22 second bins to represent the neural activity. This 22 second bins of data were converted to a single point in 2

different ways. First, the average of the Hilbert power was taken, second, maximum of the Hilbert power was calculated for the bin.

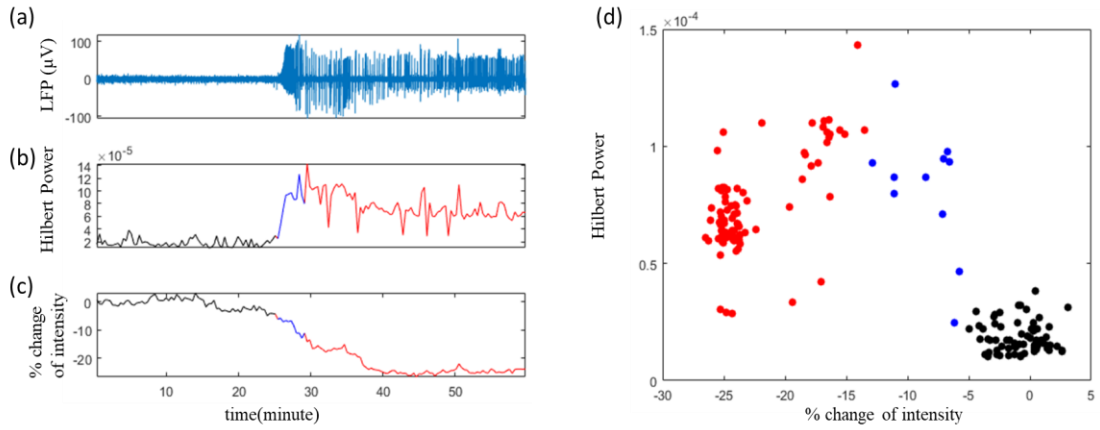

Figure 2.10 Correlation between OCT and maximum Hilbert power. (a) LFP time trace. (b) Maximum Hilbert power for a 22 seconds bin. (c) OCT intensity trace for bottom layer of an epileptiform experiment. (d) correlation between % change of intensity and max Hilbert power. The black, blue and red dot represent corresponding data of b-c in similar color.

Figure 2.9a is the time trace of LFP of a single MEA channel in CA3 region of murine brain slice and corresponding Hilbert power (Figure 2.9b) which is averaged for a 22 seconds bin to compute the correlation between the MEA and OCT data. The average Hilbert power accounts for amplitude as well as firing rate of neurons.

Before bursts of activities, there were few spikes of activities in the single channel LFP trace, so there were small fluctuations of Hilbert power. The trend of OCT intensity was similar to both LFP and Hilbert power trace. However, during the burst of activities, LFP fluctuated in between -50 μV to 60 μV and the Hilbert power increased as well. But OCT intensity decreased during the burst of activities. During the pre-seizure period (blue color in time trace of Figure 2.9b), there was a sudden increase of the Hilbert power but

the OCT intensity decreased slowly, which was due to slow change of the scattering in tissue. During the seizure period, mean Hilbert power was high and the OCT intensity decreased further and then reached a slightly lower steady state.Therefore, we found a negative correlation between the OCT intensity and the Hilbert power of electrophysiology.

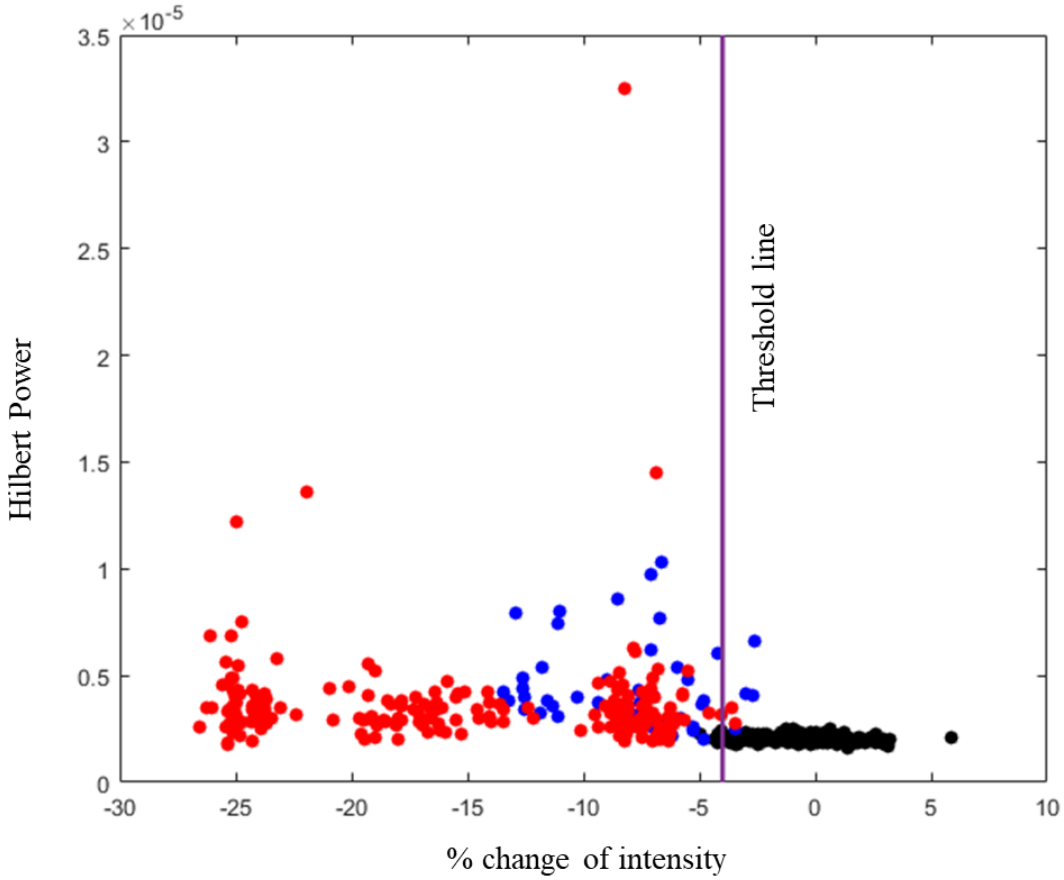

Figure 2.11 Sensitivity and specificity separate activity and non-activity. Black, Blue and red represent baseline, pre-seizure and seizure, respectively. A vertical line at -4% of intensity separates epileptiform activity from baseline with 97.27% of specificity and 97.6% of sensitivity.

The maximum Hilbert power of a bin represents the amplitude of a burst, but can't account for the firing rate. The amplitude of the initial burst was higher than the later time trace.The Hilbert power for the later approach (Figure 2.10b) was higher than the former (Figure 2.9b).However, both approaches could separate baseline from pre-seizure and seizure.

2.3.5.Sensitivity and Specificity between OCT and Electrophysiology

The Hilbert power of electrophysiology and the OCT intensity was separated into 3 parts: baseline, pre-seizure(initial high peak), and seizure.True positive, true negative, false positive and false negative was calculated from combined data for -4% intensity line(Figure 2.11). This threshold line separated epileptiform activity from no-activities with 97.27% of specificity and 97.60 % of sensitivity.

2.4.Conclusion

Spectral domain OCT can detect epileptiform activity by sensing changes of backscattered light. There was an average 10 to 18% decrease of intensity during neural activity. We used electrophysiology as a gold standard to verify the result and found a negative correlation between the Hilbert power of electrophysiology and the OCT intensity. The intensity changes in CA1, CA3, and DG were spatially correlated with electrophysiology. Finally, a threshold of -4% intensity separated activity from no-activity with 97.27% of specificity and 97.60 % of sensitivity.

Chapter 3:Detection of neural activity during seizure activation using attenuation coefficient as a biomarker

3.1. Introduction

In the previous chapter, we found that backscattered intensity can be used as a biomarker for detection of neural activity during epileptiform activity using SD-OCT. However, there was a variability of intensity in experiments to experiments. Attenuation coefficient(μ), which quantifies how strongly a sample scatters and absorbs light is a constant for a sample, can solve the problem. This chapter focuses on how μ can be used as a biomarker to detect neural activity.

The intensity variability problem is solved by taking the measurement of attenuation of light propagating through a turbid media along its path due to scattering and absorption. The attenuation of the light is dependent on the optical properties of the media and control by μ. The irradiance of the coherent laser light beam that propagates during image acquisition through brain slice (assuming homogeneous along the z-axis) is given by Lambert-Beer's law as:

$$L(z) = L_0 e^{-\mu z} \tag{3.1}$$

where $L(z)$ is the irradiance of the beam after traveling through the brain slice over a distance z, L_0 is the irradiance of the incident light beam. From equation 3.1, the larger the value of μ, lesser the propagation of light for a fixed distance of z. Attenuation coefficient

is therefore an intrinsic optical property of the sample and should not suffer from variability due to fluctuations in the incident light intensity from the system from day to day.

The detected OCT signal from brain slice from a depth of z can be described by[4, 122]:

$$I(z) = I_0 e^{-2\mu z} \tag{3.2}$$

Here, the factor of 2 is due to the double-pass nature of light propagation in and back out of the brain slice. μ can be estimated by taking logarithm on both side of the equation 3.2 as:

$$\mu = -0.5 * \frac{\ln(I(z)/I_0)}{z} \tag{3.3}$$

The μ can be calculated from equation 3.3 by fitting it with an intensity depth profile.

In this study, we demonstrate that changes in optical properties of murine brain tissue during epileptiform activity can be detected using SD-OCT by inducing a burst of neural activities, measuring μ from the tissue over time, quantifying these changes, and validating by correlating with electrophysiology.

3.2.Materials and methods

3.2.1.Animals

Wild-type (Jackson Laboratory, C57BL/6J, stock number 000664) mouse colonies were bred and maintained in house to generate pups for this study. Both male and female mice were used in this study.

3.2.2.Slice preparation

The slice preparation section is described in section 2.2.2.

3.2.3.Imaging system

The imaging system is described in section 2.2.3

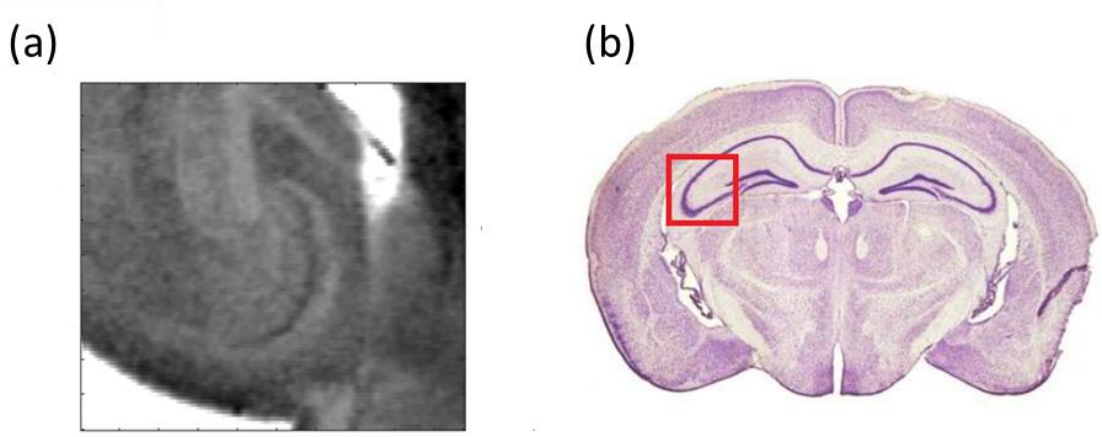

Figure 3.1 Data acquisition in hippocampus. (a)OCT *en face* image of hippocampus of murine brain slice (b) Schematic representation of mouse hippocampus with cornu ammonis (CA), dentate gyrus (DG) and stratum lacunosummoleculare regions[123].

3.3.Data acquisition and processing for OCT and Electrophysiology

Both OCT and electrophysiology data were recorded simultaneously from hippocampus area of murine brain slice (Figure 3.1).

3.3.1. OCT data acquisition and processing

A spectral-domain OCT system was used to acquire images of the murine brain slice. OCT volumetric data was acquired at the A-line rate of 15 kHz, and a single volume has 100 cross-sectional images composed of 1024 A-lines. Acquisition time for each volume was 12 s. An imaging depth of 2 mm was obtained with 6.5 mW of incident power on the brain slice. To have uniform wavenumber spacing, linear interpolation was performed to obtain nonlinear k-space sampled spectral data. The fast Fourier-transformation(FFT) from wavenumber to the spatial domain was performed, and depth-resolved structural information was retrieved. A depth-dependent sensitivity data was measured, and removed by multiplying each A-line by a calculated correction curve[120].

The noise for each A-line was different due to reflection from electrodes and generated by averaging intensity of 20 pixels from the top of the A-lines where there is no brain slice. A noise-free A-line was obtained by subtracting noise from each A-line. A median filter of size 70 x 70 μm was applied to minimize variation due to coherence speckle. Kernel size was determined by applying a filter on cross-sectional images to achieve a speckle contrast ratio below 0.1 over a uniform slice of tissue. The top and bottom surfaces of the brain slice were detected by SNR thresholding of 80 dB, and an *en face* intensity image was generated by averaging whole volume in axial direction. Lateral

motion was measured by cross-correlation of reference *en face* image from baseline with all other *en face* images, and this correction was applied to all other volumes with respect to reference volume.

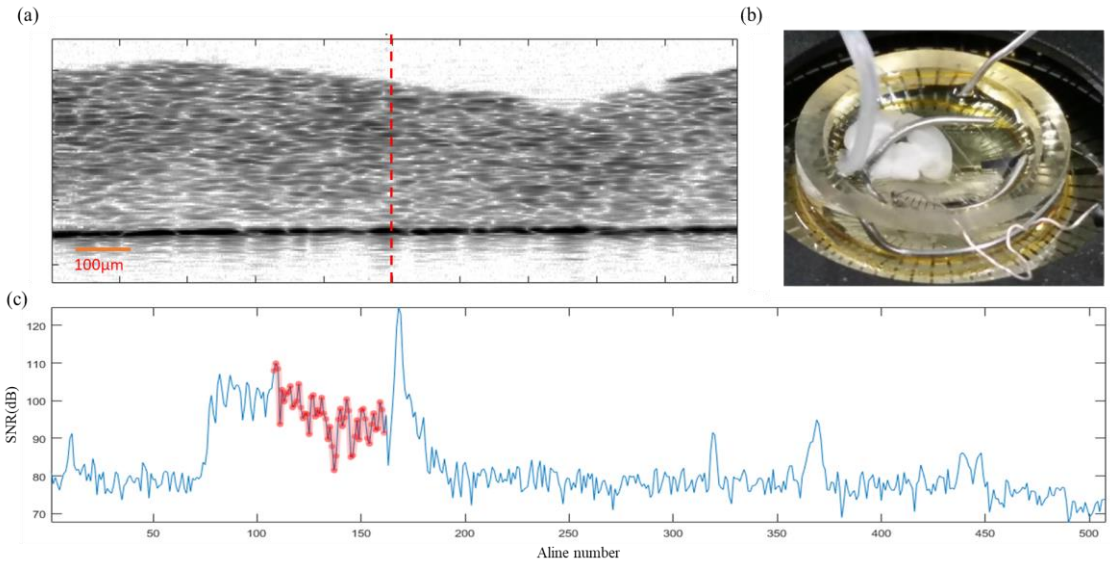

Figure 3.2 Transparent brain slice and its cross-sectional image. Cross-sectional image(a) of a transparent brain slice(b) in MEA well. (c) depth profile from cross-sectional image at the position of vertical red line.

The cross-sectional intensity image of brain slice cannot be converted into corresponding µ image in the pixel to pixel as described by Vermeer[124]. That method inherently assumes that incident light is attenuated within the imaging depth range. If most of the sample is transparent, it does not hold true. For our case, brain slice was 300 µm thick and transparent enough to pass a considerable amount of light (Figure 3.2a-b). The intensity at the bottom of the brain slice is 20 dB. Therefore, the Vermeer method cannot be applied to examine the data obtained from brain slices.

For the transparent sample with low attenuation coefficient, fitting methods can estimate attenuation coefficient with sufficient accuracy [125, 126].But fitting method (from equation 3.3) only provide a μ value for a depth range assuming tissue is homogeneous for the entire depth range. Fortunately, brain slice is relatively homogenous within depth range of 300 μm. Therefore, this method can estimate μ from the brain slice.

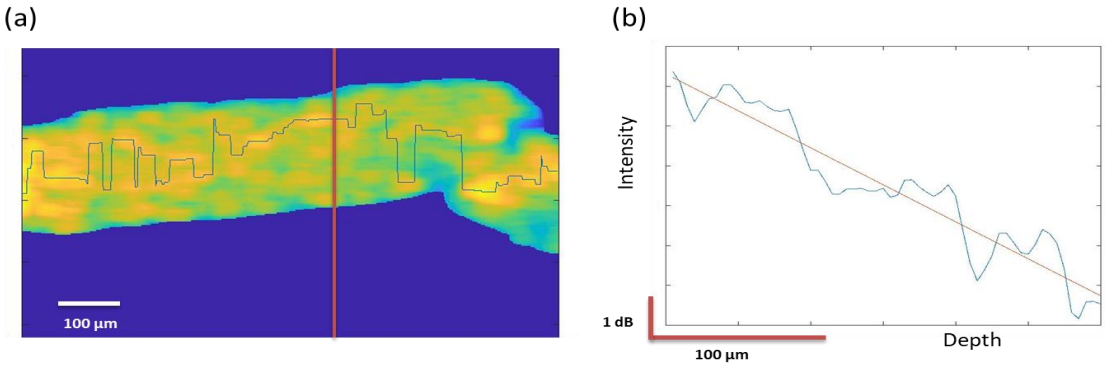

Figure 3.3 Cross-sectional image of murine brain slice. (a) Cross-sectional image of a slice with maximum intensity line. (b) depth profile from maximum intensity line to bottom of brain slice is taken from (a) indicated by vertical red line. The blue line is the depth profile and the pink straight line is the fitted line. Slope of the fitted line is the attenuation coefficient.

The single A-line does not follow the exponential equation of 3.3 due to speckle in the tissue. The maximum intensity of the A-line is inside the slice (see Figure 3.3a), not at the top of the brain slice. From the maximum intensity point, the shape of the depth profile follows the equation 3.2(see Figure 3.2c). Therefore, a maximum peak of each A-line was found, and from maximum peak to bottom of the slice was selected to calculate μ (red portion of depth profile in Figure 3.2c). The selected portion of the A-line was converted to a logarithmic scale and fitted with equation 3.3, and negative of the slope of the fitted line was the μ of that portion of A-line (Figure 3.3b). The process was repeated for all A-lines of a cross-sectional image. Thus, a cross-sectional intensity image converted

into a row of μ value. For all cross-sectional intensity images of a volume were converted to an *en face* attenuation coefficient images. The μ of each volume was averaged over time to have time plot. Percentage change of μ from baseline was calculated. Standard deviation(σ) was calculated for time t for all data sets of control experiment with ACSF only or epileptiform activity experiment with ACSF and 4-AP. Percentage change of μ time was plotted with additional indications of 2σ above and below the mean μ. Corresponding heatmaps was also generated by projecting % change of μ on intensity *en face* intensity images.

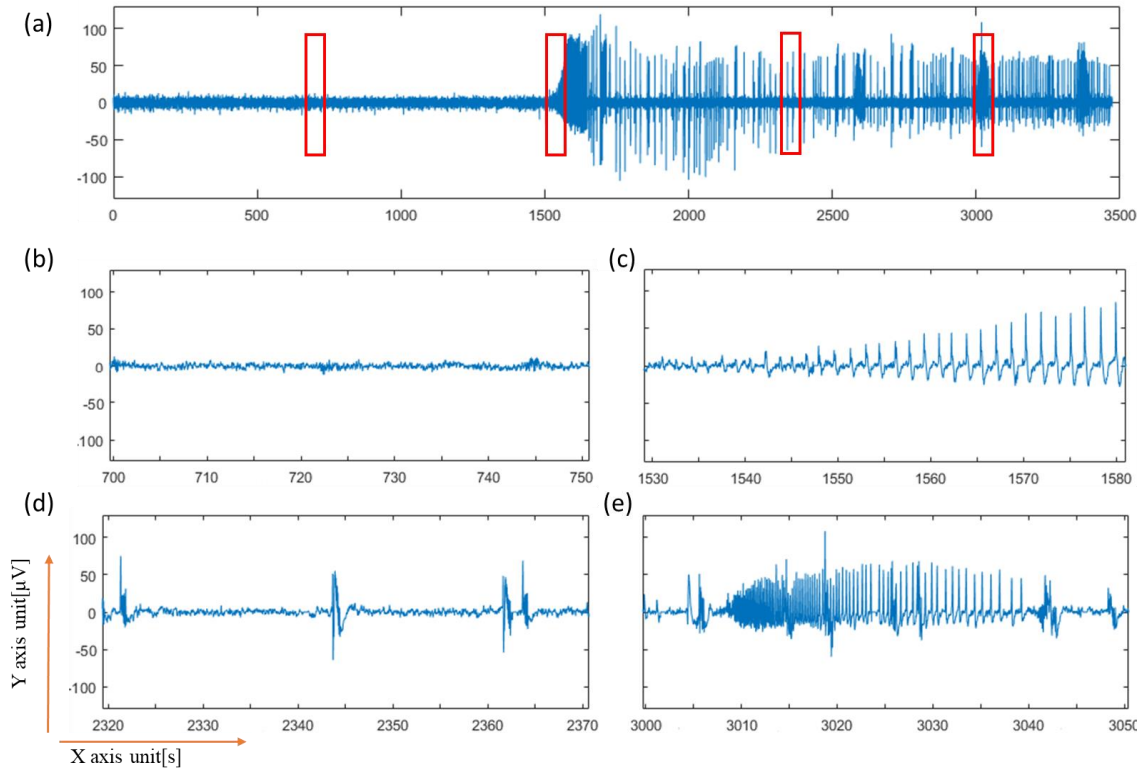

Figure 3.4 LFP time trace for an experiment. (a) LFP time of 4-AP induced epileptiform activity. (b) During baseline, LFP fluctuates between -15 μV to 15 μV. (c)In pre-seizure, LFP increase from baseline to 120 μV.(d) During epileptiform activity, amplitude of LFP is lower than pre-seizure. (e) High frequency neural activities.

3.3.2.Electrophysiology data acquisition and processing

Multielectrode array (MEA) recordings were performed on a 60-channel optically clear array (60pMEA200/30-Ti) with a low-noise amplifier (MEA1060-BC) from MultiChannel Systems. Details are discussed in section 2.3.2.

Data were acquired using MC Rack software (MultiChannel Systems) and exported to MATLAB (MathWorks) for further processing. Data from all 60 MEA channels were collected at 10 kHz. Bandpass (0.1 - 7 Hz) 2nd order Butterworth filter was applied to remove OCT-induced electrical noise (Figure 3.4). The built-in Hilbert Matlab function was used to compute the Hilbert power(HP) of the bandpass filtered data. The HP was then averaged across all channels for in 22 second bins to compute the correlation between the MEA and OCT data. Heatmap of EEG trace was also generated by projecting Hilbert power of each electrode on MEA grid.

The HP was normalized with respect to baseline because there was a slight difference of baseline of LFP for the experiment to experiment due to the unequal distance between the bottom surface of brain slice and the top surface of MEA. The details are discussed in section 2.2.4.2.

3.4.Results and Discussions

Baseline images were taken from murine brain slice that were kept functionally active by constant flow of oxygen-perfused ACSF solution. Then images with neural activities were taken by flowing 4-AP solution into brain slice. The composition of ACSF

and 4-AP were different and for the acquisition of OCT images, the light passed through the solution of ACSF and 4-AP. As optical signal-to-noise ratio especially the scattering during neural activity were small [127], we wanted to make sure that during 4-AP induced neural activities, there was no contribution of the 4-AP solution on the backscattered light. To demonstrate the effect of 4-AP on brain slice, we took images of dead brain slice by flowing 4-AP solution after 20 minutes of baseline data with ACSF solution.

3.4.1.Control experiment with dead slice

A brain slice was kept without the oxygenated solution for 10~15 minutes to kill neural activity. Then the slice was moved on MEA to collect LFP. There were no activities in the LFP. After that, brain slice was perfused for 20 minutes with ACSF solution and then the tube was switched to the 4-AP solution. It took 4 minutes to reach the 4-AP solution into the slice, and the 4-AP solution was continued to perfuse till the slice was deformed.

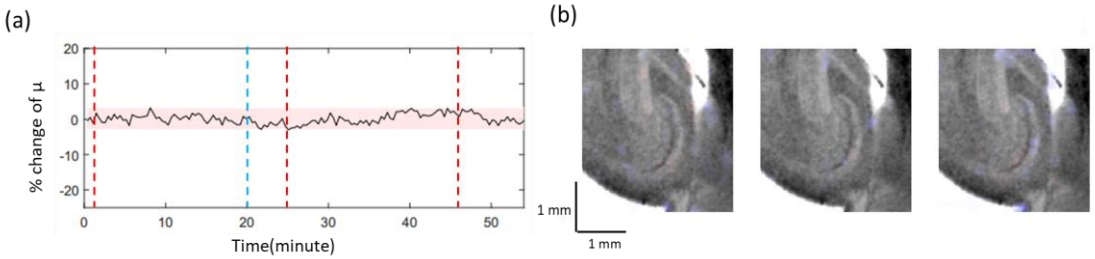

Figure 3.5 Effect of 4-AP on μ. (a)The time trace of μ of dead slice. ACSF solution was flowed in brain slice till 20th minutes, then solution exchange started from ACSF to 4-AP. After 4 minutes, 4-AP solution flowed into brain slice. The μ trend after 4-AP introduction was same as before. (b) heatmap also shows no indication of % change of μ from baseline.

The attenuation data was processed according to the section 3.3.1. In Figure 3.5a, the first 20 minutes was the baseline period, then solution exchange started, and 4-AP solution entered slice at 25th minute. The average μ time trace demonstrated that there was no change of μ due to the introduction of the 4-AP solution into brain slice. The standard deviation(σ) was calculated on the baseline data, and the ±2σ line was drawn from the average baseline line. The percentage fluctuation of μ was ±3%. The heatmap was calculated during baseline, just after introduction of the 4-AP solution to brain slice, and 20 minutes after the introduction of the 4-AP solution. The heatmap of % change of μ indicated that there were no changes of μ for the 4-AP solution only (Figure 3.5b).

3.4.2.Control experiment with ACSF

Another set of control experiments were performed with ACSF solution to see the effect of ACSF on live murine brain slice. The OCT images were acquired about an hour by continuously flowing ACSF solution, and simultaneously acquiring electrophysiology data. The time trace of average μ was calculated and % change of μ was calculated from baseline for each experiment. The results from 3 experiments were combined by taking the average of all of them. As there was no solution change from ACSF to 4-AP, so all HPs were synchronized at the start of the experiment. The σ was calculated for all experiments for each time point during the full experiment period, and ±2σ shaded area was drawn in pink color from the average time trace (Figure 3.6a).

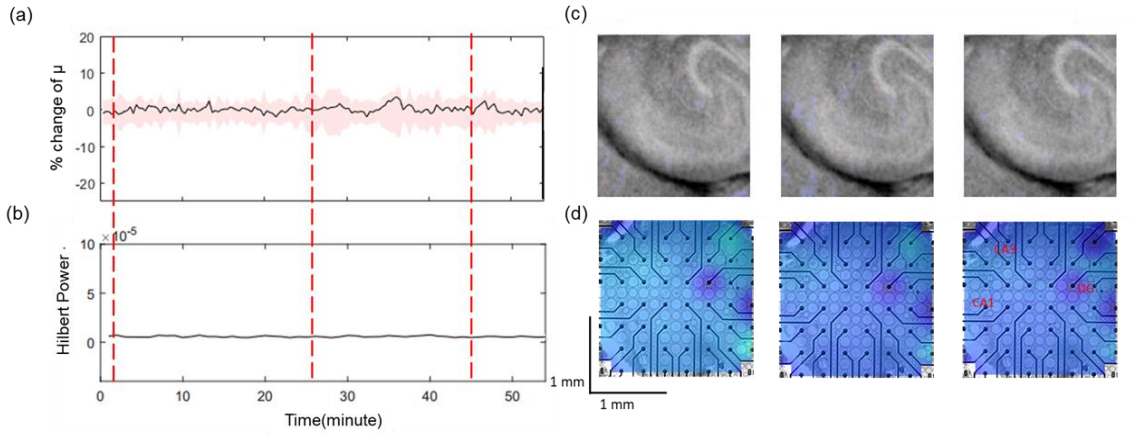

Figure 3.6 Control experiment with ACSF solution only. (a) time trace of attenuation coefficient after averaging of 3 experiments. The pink shaded area is the ±2σ area from mean time trace, and the % change of μ is less than 3%. The black line is the data of an experiment for which OCT heatmap is generated. (b) The mean HP of electrophysiology with ±2σ line in pink also generated like OCT time trace. The black line is the data of an experiment for which EEG heatmap is generated. (c) % changes of μ in OCT *en face* images of brain slice, and corresponding HP changes(d) from electrophysiology. Heatmaps were taken at the time of 3 red vertical lines drawn in a-b. There are no significant changes of either μ or HP over time of control experiment.

Similarly, the mean HP of 3 experiments was calculated for 3 experimental data. The σ calculation and shaded area generation process was like OCT. The OCT *en face* heatmap (Figure 3.6c) and HP heatmap (Figure 3.6d) demonstrated that there were no significant changes in either μ or HP in the brain slice. Overall, the ACSF has no effect on % changes of the attenuation coefficient of murine brain slice.

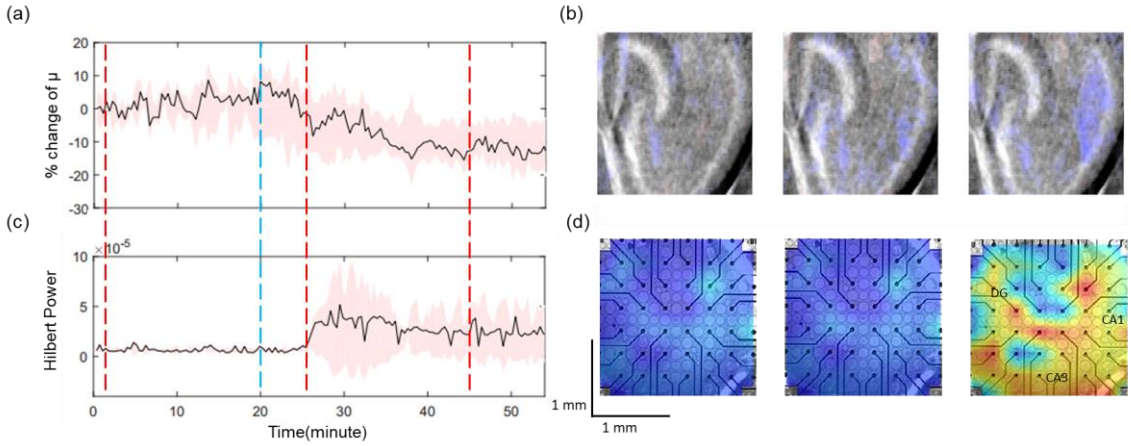

Figure 3.7 Epileptiform activity after introduction of 4-AP solution (a) time trace of attenuation coefficient after averaging of 3 experiments. The shaded pink area is the ±2σ line from the mean μ. The μ fluctuates between ±5% during baseline and decreases 10~15% during epileptiform activity. The black line is the data of an experiment for which OCT heatmap is generated. (b) The mean HP of electrophysiology with ±2σ line in pink also generated like OCT time trace. The black line is the data of an experiment for which EEG heatmap is generated. (c) % changes of μ in OCT *en face* images (blue-decrease, red-increase) of brain slice, and corresponding HP changes(d) from electrophysiology. Heatmaps were taken at the time of 3 red vertical lines drawn in a-b. There is spatial correlation of μ changes and HP changes.

3.4.3.μ decreases during epileptiform of activities

Epileptiform activity was induced by flowing 4-AP solution into brain slice. For the baseline, ACSF solution was perfused in brain slice for 20 minutes, then the tube was switched from ACSF to the 4-AP solution, and the 4-AP solution reached into slice within 3~5 minutes, and 4-AP continues to flow in the slice for next 35~40 minutes.

The start time of the epileptiform activity was calculated from HP time trace based on standard deviation of the baseline. For each experiment, standard deviation(σ) was calculated from baseline (first 20 minutes) and the ±2σ line was drawn and extrapolated for the entire duration of the experiment. As the HP was positive, the +2σ line crossed the HP trace, and that crossing time point was the start of epileptiform activity. All 3

experiments were aligned based on the starting point of epileptiform activity. The mean and standard deviation was calculated like ACSF control experiment. Also, ±2σ shaded area was drawn like ACSF control experiment (Figure 3.7a-b).

There was a correlation between percentage change of μ and mean HP trace. During the baseline, there was no significant increase or decrease of μ, and corresponding HP. At the 25th minute, HP started to increase, and μ started to decrease. Although HP increased like a burst at the start of the epileptiform activity, μ changed slowly because of scattering of tissue changes slowly. After the initial burst, HP was steady but μ decreased slowly. Therefore, the time the trace of the attenuation coefficient separated activity from non-activity.

There was a qualitative spatial correlation between OCT μ changes in CA1, CA3 and DG area with electrophysiology (Figure 3.7c-d). At the baseline, there was no significant changes of μ, and HP. During pre-seizure, μ started to change, so did the HP. During epileptiform activity, there was a decrease of μ (blue color in *en face* OCT image) and increase of HP (red color on EEG) in CA1, CA3 and DG area.

3.4.4.Correlation between optical changes and Electrophysiology

The collected LFP from CA3 region was converted to HP. As the OCT volume represent data of 22s, HP also segmented as a bin of 22s to match with OCT attenuation coefficient. The HP was further processed in two ways. First, maximum HP of a bin was

the representative data of that bin. Second, mean HP of a bin was the representative data of that bin. The two methods of HP can explain the different dynamic of firing.

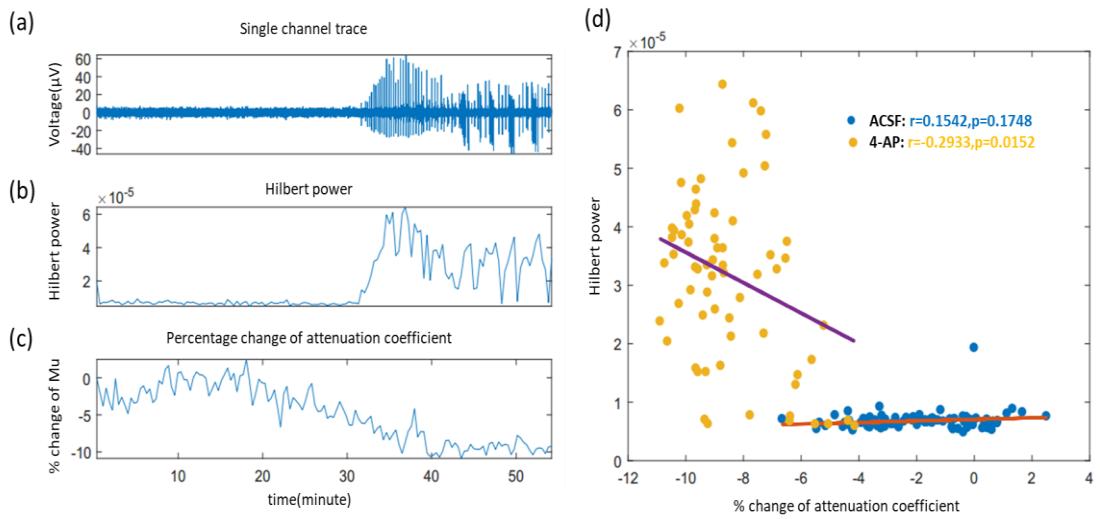

Figure 3.8 Correlation analysis with μ and maximum HP. (a) Single channel trace of electrophysiology data collected from CA3 region. (b) Maximum HP of a bin of 22s (c) Percentage change of attenuation coefficient over time. (d) correlation between percentage change of attenuation coefficient and maximum HP.

Figure 3.8 demonstrates the correlation analysis for maximum HP. The LFP of a single channel (Figure 3.8a) was converted to HP, and maximum HP was calculated for a bin of 22s (Figure 3.8b). The OCT attenuation coefficient decreases 10% during seizure activation (Figure 3.8c). The correlation between % change of μ and maximum HP was done for both ACSF and seizure activation(4-AP). The correlation coefficient(r) was 0.1542 with insignificant p value but during seizure activation, the correlation coefficient(r) was -0.2933 with $p<0.05$, which was significant. The negative correlation during seizure activation indicates opposite action i.e. increase of HP and decrease of μ. The slope of the fitted line is also different in baseline and epileptiform activity.

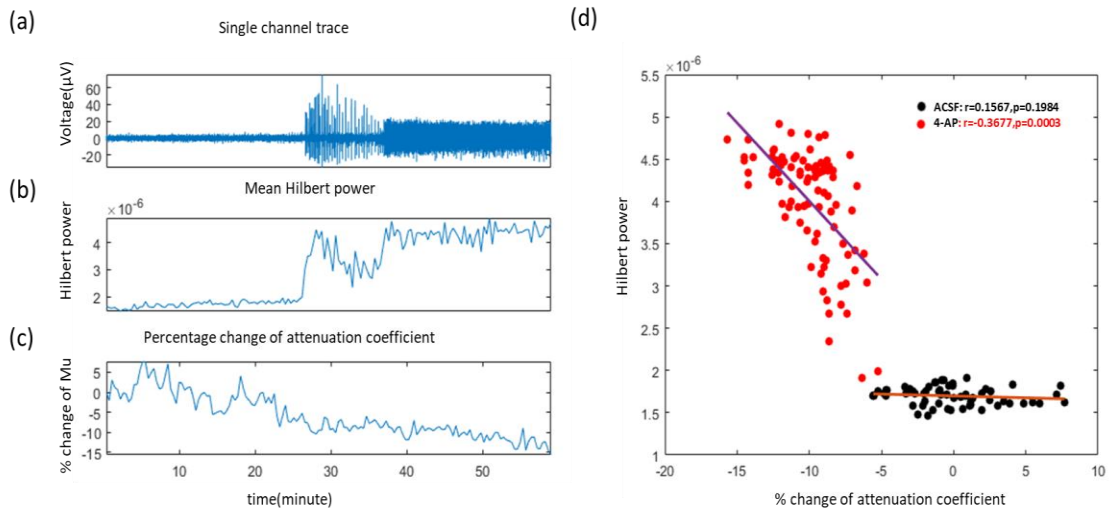

Figure 3.9 Correlation analysis with μ and average HP. (a) Single channel trace of electrophysiology data collected from CA3 region. (b) Mean HP of a bin of 22s (c) Percentage change of attenuation coefficient over time. (d) correlation between percentage change of attenuation coefficient and mean HP.

Correlation analysis was done similar way except for average HP of a 22 seconds bin was taken as the representative data of that bin. Figure 3.9a is the LFP from the single channel and converted to HP (Figure 3.9b). The OCT attenuation coefficient decreases 10~15% during seizure activation (Figure 3.9c), which corresponds to increase of mean HP. Correlation between percentage change of μ and mean HP was calculated separately during baseline and epileptiform activity. During the baseline period, the correlation coefficient was 0.1567 with insignificant p value but during epileptiform activity, the correlation coefficient was -0.3677 with $p<0.05$. Also, epileptiform of activities were different than the baseline. The slope of the fitted line of epileptiform activity is greater than the baseline.

The results of 3 experiments were combined, and divided into baseline, pre-seizure and seizure region. Figure 3.10a shows the results of correlation of maximum HP with % change of μ. During the baseline period, attenuation coefficient fluctuates between -6~8%, and HP is relatively constant compared to pre-seizure or seizure period. During the pre-seizure period, max HP is higher than the seizure period, the attenuation coefficient changes are in between seizure and baseline. There is a clear boundary between seizure and the baseline period. During the epileptiform of activities, the attenuation coefficient decreases by 7~16%. A vertical green line at -6% was drawn to separate baseline and activities. True positive, true negative, false positive and false negative was calculated, and the specificity and sensitivity was 99.5% and 94.8%, respectively.

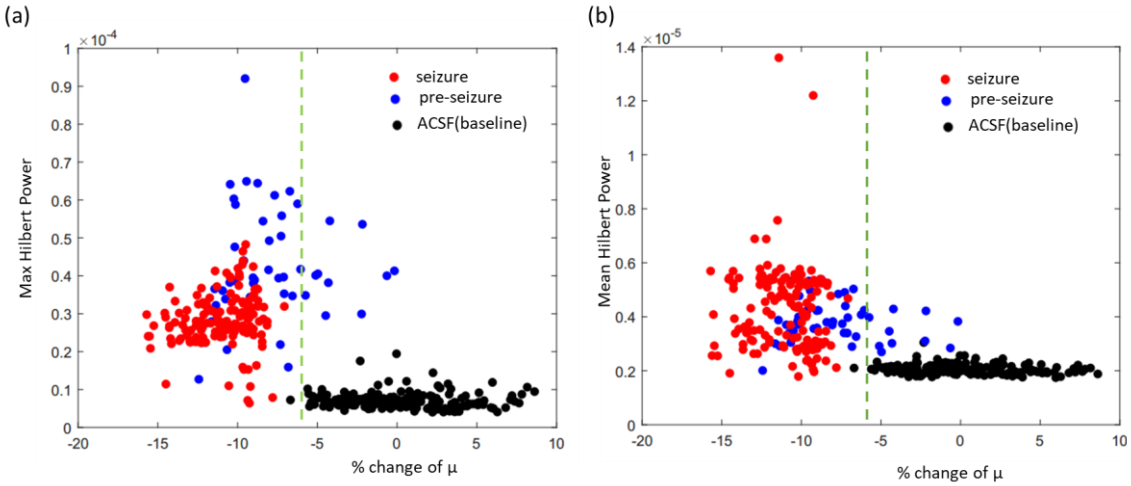

Figure 3.10 Correlation between attenuation coefficient and HP. (a) Combined correlation scattered plot of 3 experiments Pre-seizure maximum HP is higher than seizure. The vertical line separating seizure from non-seizure has the specificity of 99.5% and sensitivity of 94.8% (b)Pre-seizure area is in between baseline and seizure. The vertical line separating seizure from non-seizure has the specificity of 99.5% and sensitivity of 94.8%.

The range of baseline HP (Figure 3.10b) in mean HP is narrower than the maximum HP. Most importantly, the pre-seizure amplitude of mean HP (Figure 3.10b) is less than maximum HP (Figure 3.10a). The number of the firing of neurons per second is lower in pre-seizure than seizure but the amplitude is higher. Therefore, the maximum value of the HP is higher during pre-seizure than mean HP.

A vertical green line at -6% was drawn to separate baseline and activities. True positive, true negative, false positive and false negative was calculated, and the specificity and sensitivity was 99.5% and 94.8%, respectively.

In both analyses, the decrease of attenuation coefficient and the increase of HP were different in seizure and baseline. Attenuation coefficient decreases by 6%(vertical green line of Figure 3.10) separates the seizure and non-seizure area.

3.5.Conclusion

SD-OCT can detect neural activity during seizure activation by quantifying the changes of attenuation coefficient. The control experiment on dead brain slice with ACSF and 4-AP demonstrated that there was no influence of 4-AP on OCT signals. There were also no changes of μ during control experiment with ACSF only. Therefore, collected OCT signal during epileptiform of activities accounts only for neural activities.

There was a 10~15% decrease of μ during epileptiform of activities, which correlate with gold standard electrophysiology. The decrease of μ in hippocampus correlated spatially with electrophysiology. The correlation coefficient of time trace during

epileptiform of activities was negative and statistically significant ($p<5\%$). However, the correlation coefficient was different between baseline, and seizure activation and a percentage change of μ threshold (6%) separated them.

Chapter 4:Non-contact detection of neural activities in functionally stimulated horseshoe crab using phase-resolved optical coherence tomography

4.1.Introduction

This chapter describes of detection of neural activity in millisecond temporal resolution from optic nerve of the functionally stimulated compound eye of horseshoe crab(*limulus).* The pr-SDOCT was used to detect thickness changes during neural activation.

Electrophysiology, which requires direct contact or near direct contact with neurons, measures action potential from a single neuron or a group of neurons with high sensitivity and temporal resolution. Although collected information has a high signal to noise ratio, contact with neurons may damage the tissue under investigation[128-131].The fluorescence imaging has been demonstrated a reliable way of detecting action potential from neurons which needs the introduction of reporter molecules into the cells, and measured signal results from the conversion of the electrical signal into fluorescence by mean of a reporter. However, there is a risk of perturbing biological system under study depending on the dosage of reporter molecules[129, 132]. Besides, it is challenging to introduce them to a specific location because of involvement of invasive procedure in most cases, which limits on the wide application of these contrast agents. So, there is a need for a label-free optical method which can detect action potential by overcoming these disadvantages.

Starting from 1950, few studies have found that nerve undergoes transient structural changes in thickness or volume as well as changes of optical properties such as scattering, birefringence, fluorescence, and absorbance[127, 133-138]. Hill found that a single cuttlefish nerve fiber increases about 0.1μm for 10,000 impulses. There was also a change of opacity in a crustacean nerve trunk following repetitive stimulation [134]. *Iwasa* reported a fast (3-5 ms) swelling of 5-10 nm in crab nerve bundles[135]. Tasaki and Byrne studied changes in garfish olfactory nerves in a watertight container[136, 137].In 2003, Yao *et al.* measured a displacement of 0.1-0.8 nm for lobster nerve bundles (average of 100 responses) [138].

The pr-OCT demonstrated detection of the structural changes associated with neural activity [95, 96, 99, 139, 140]. It can detect and measure sub-nanometer displacements. These capabilities make OCT an important tool to study neural activities. Akkin *et al*. used a phase-sensitive OCT system to measure the transient neural surface displacement in crayfish walking leg nerve during propagation of nerve impulses and was able to detect transient motion on the order of 0.4-1.0 nm (average of 500 responses) of the saline bath/nerve tissue interface on a time scale of 1-2ms [96]. Fang-Yen *et al.* used a similar configuration that measured the displacement of a lobster nerve with respect to a reference glass surface. A 5 nm swelling with duration of 10ms (single response) was detected, indicating a compound response [140]. Akkin *et al.* had also demonstrated similar results in squid giant axons [99, 139].

Here we present our study of detection of optical changes during action potential in horseshoe crab optic nerve. Previous studies with OCT mostly used nerve with large size (diameter of 300-450 μm) or nerve fiber bundle (diameter of 100-300 μm)[95, 96, 99, 139, 140]. In this study, we used horseshoe crab optic nerve with a diameter of (3-10 μm) which was the physiological relevant size of the mammalian peripheral nervous system[141-143]. Another aspect of this study was that the nerve was functionally stimulated by shining the lateral compound eye, instead of electrical stimulation of the nerve itself. Optical detection of functionally stimulated nerve activity removes the possibility of stimulation artifacts in recording and more importantly, opens the opportunities for future studies on monitoring small-scale network activity.

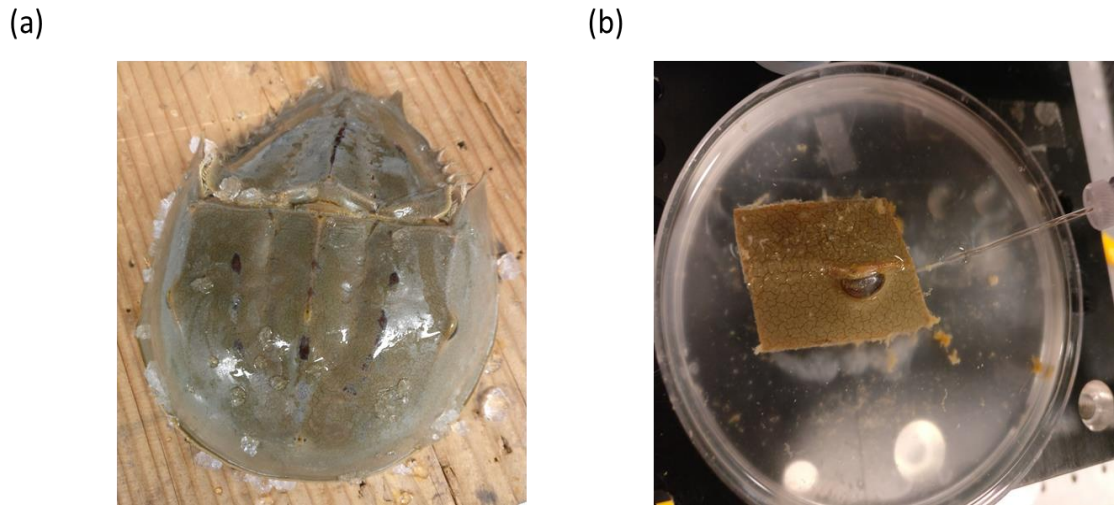

Figure 4.1 Dissection of Horseshoe crab (a) Horseshoe crab before dissection (b) Horseshoe crab after dissection

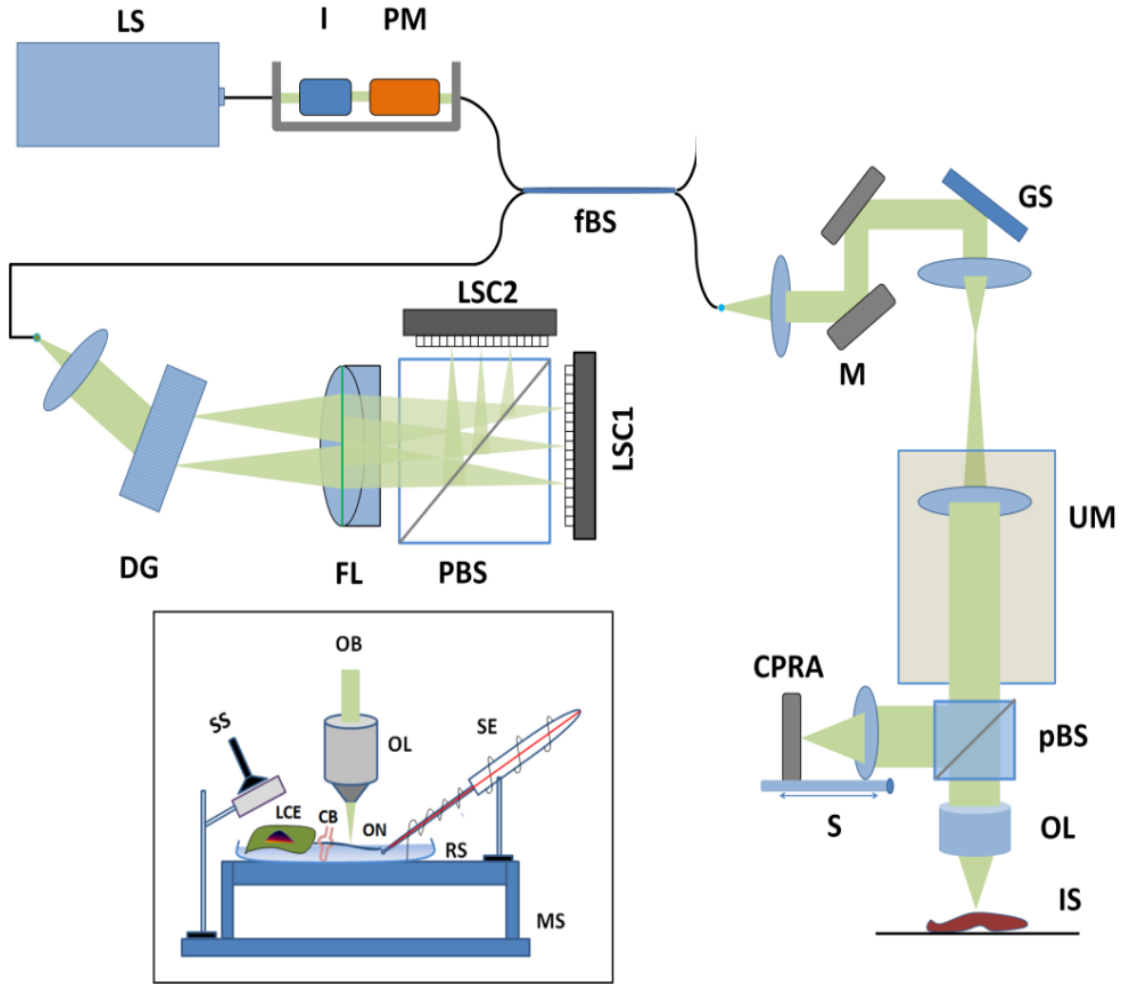

Figure 4.2 Spectral domain OCT system. LS: light source (Ti:Sapph 800nm laser), I: isolator, PM: polarization modulator, fBS: fiber-based beam splitter, M: mirror, GS: galvo scanner, UM: upright microscope, pBS: plate beam splitter, nCPRA: near common-p, OB: optical beam , SE: suction electrode, CB: cold block, ON: optic nerve, RS: resting stage,LCE: limulus compound eye

4.2.Materials and methods

4.2.1.Animals

Medium size (6”-8” in diameter) male Limulus (Marine Biological Laboratory, Woods Hole, MA) with clear (non-injured) lateral eyes was chosen for dissection. All experiments and procedures were performed according to University of California, Riverside Institutional Animal Care and Use Committee-approved protocols.

4.2.2.Dissection of horseshoe crab

The horseshoe crab was cold-anesthetized by keeping it in an ice bucket for 30 minutes. This cold- anesthetized animal was attached to a wooden board for dissection (Figure 4.1). One lateral eye was extracted carefully with optic nerve and put on petri dish with Ringer’s solution (430 mM NaCl, 9.56 mM KCl, 9.52 mM CaCl2.2H2O, 9.97 mM MgCl2.6H2O, 50 μM HEPES). The pH of the solution was maintained 7.4.

4.2.3.System description

The common path configuration of SD-OCT at 800 nm wavelength was used in this study (Figure 4.2). The light from a Ti: Saph broadband mode-locked laser (Femtolasers, Inc., Integral OCT 2709, center wavelength 804 nm, bandwidth 170 nm) was passed to a sample and a reference arm equally by a 2x2 fiber-based beam splitter. The backscattered lights from both arms are collected by a custom-built spectrometer. The sample arm was incorporated into an upright microscope (Olympus, BX61) through the camera port. The raster scanning was managed by a galvanometer based scanner (Cambridge Technology, Inc., 6210H). This arm was incorporated with a small internal reference arm placed within

the microscope just after the tube lens to reduce mismatch of refractive index. A plate beam splitter (Thorlabs, BS111) splits the sample arm beam into 70:30 ratio while 30% light transmits to the small reference arm that consists of a lens and a mirror both mounted on a one-dimensional moving stage. The remaining light is transmitted through an objective lens (Olympus, UPLSAPO 4x) on the sample which rests on a micromanipulator controlled stage (Sutter Instruments). The spectrometer consists of a diffraction grating (Wasatch Photonics, 1200 lpmm, 830 nm), a focusing lens (JenOptik Optical Systems, f=150mm), polarization beam splitter cube (Rocky Mountain Instrument Co., 4-inch Cube) and two line scan cameras (Basler sprint camera, sp4096-140km). The axial resolution of the system was measured to be 2 µm in the air and the lateral resolution to be 4 µm with the 4x objective. The maximum acquisition speed of the line scan camera is 144000 lines/seconds and yields a temporal resolution of 7µs. The detected spectrum from the camera is sent to the computer through a frame grabber (National Instrument, NI1429). Another data acquisition card (National Instrument, NI 6259) runs two BNC breakout boxes (BNC 2110 and 2120) which generate the controls signals for the line scan camera, scanning mirrors, stimulation shutter and electrophysiology recording unit. A PCI-e chassis (Magma) accommodates all these PCI-e cards and a workstation computer is used for controlling data acquisition.

4.2.4.OCT data acquisition and processing

OCT M-scan (without any lateral movement of laser beam) images were acquired at 10 kHz from optic nerve of the compound eye of the horseshoe crab. The duration of the

action potential is 2~3 ms. Therefore, at the acquisition speed of 10 kHz (time resolution of 0.1 ms), action potential propagation at a single observation point has a temporal duration equivalent to 20 to 20 depth scans, which are enough to represent thickness change due to action potential. If the acquisition speed is increased, then the camera exposure time is decreased. Less exposure time means less collection of photons from the sample. As the SNR depends on collected photons from the sample, lower exposure time reduces the system SNR[7]. Less SNR reduces the system sensitivity to detect thickness change from the sample (details are discussed in section 4.3.1).

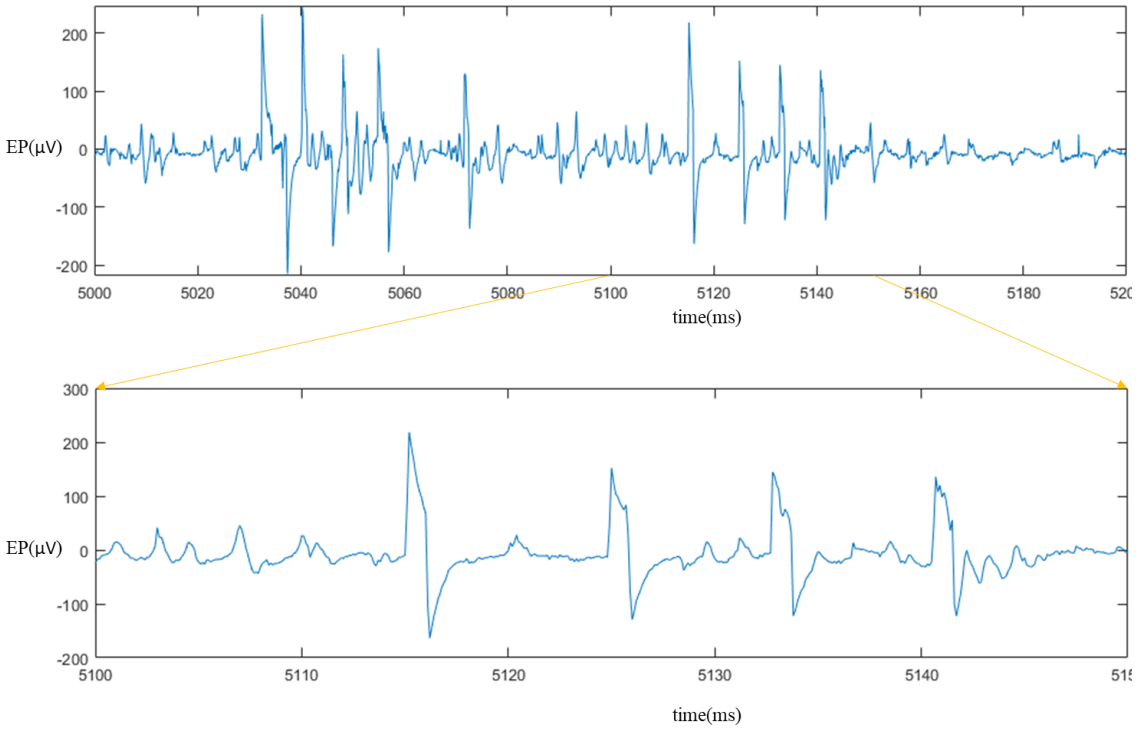

Figure 4.3 Electrical recording by suction electrode

To have uniform wavenumber spacing from the collected spectrum, linear interpolation was performed to the nonlinear k-space sampled spectral data. The fast Fourier-transformation(FFT) from wavenumber to the spatial domain was performed, and depth-resolved structural and phase information was retrieved.

4.2.5.Electrophysiology data acquisition and processing

The axon or axon bundle were sucked into the suction electrode (Figure 4.2). To induce neural activity, a UV flashlight was used for visual stimulation of the compound eye. The neural activity data from the suction electrode was sent to a differential amplifier (Warner Instruments, DP-301) for filtering of noise and amplification and then sent both to the acquisition computer for recording and to an oscilloscope for visualization. The electrode data was processed in Matlab2016b. The time domain data was transformed to the frequency domain by FFT to remove 60Hz noise and its harmonics. Figure 4.3 shows the electrical recording by the suction electrode.

4.3.Results and discussion

The control experiment was performed for the pr-OCT system to test its capability to measure thickness changes. The piezo wire, which is known to swell after applying a voltage across it, is used to mimic thickness change in nm range. Then horseshoe crab optic nerve data were collected to detect swelling of axon during action potential propagation.

4.3.1.Phase noise measurement of pr-SDOCT

A coverslip was used as a sample to check the phase noise of the system. Data was acquired from the coverslip placed at the focal plane of the 4x objective for 60s in M-scan (no lateral movement of sample arm laser light) mode for different signal to noise ratio(SNR). The varying SNR was achieved by placing neutral density filter(NDF) in sample arm and varying the position of NDF for different attenuation level. The data was analyzed to extract intensity and phase information as described in section 4.2.4.

The top and the bottom layers of the coverslip were the layers of interest, and the phase difference between these two layers was calculated. Change in this differential phase *(Δφ)* can be converted to change in actual path length (or thickness) *(Δp)* in the sample arm using the relation:

$$\Delta p = \frac{\lambda_c * \Delta\varphi}{2\pi/2} \tag{4.1}$$

where λ_c is the center wavelength of the source (804nm) and "2" accounts for the double trip of backscattered light from the sample and the reference arm.

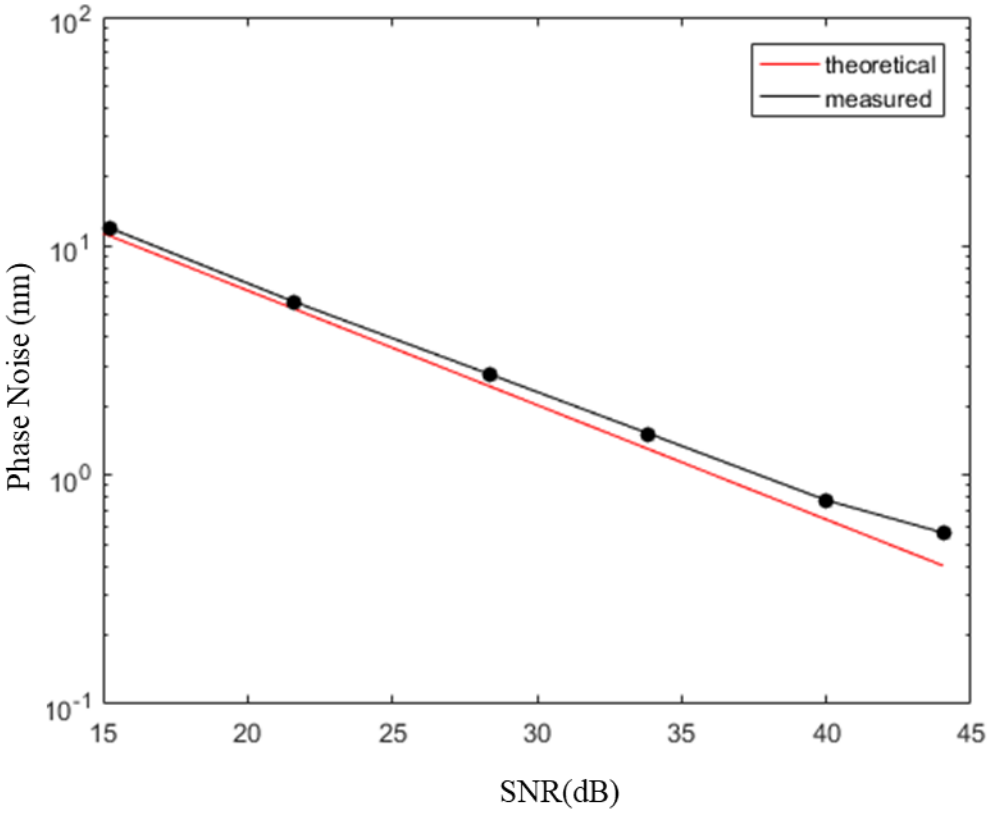

Figure 4.4 Measurement of standard deviation of phase difference between top and bottom of coverslip for different signal to noise ratio. Red line indicates theoretical value of phase noise from equation 4.3, and black line indicates actual measurement of phase noise

For an invariable thickness of coverslip, the phase difference should remain constant over time. However, there is a variation of the phase difference, and standard deviation of this phase difference defines the noise margin of the system for a given SNR. This noise margin sets the threshold of the minimum detection capability of the system for a SNR. Phase noise margin ($\sigma_{\Delta\varphi}$) directly dependent on SNR through this relation[11, 144] by:

$$\sigma_{\Delta\varphi} = \sqrt{\frac{1}{SNR}} \tag{4.2}$$

For the SNR at the top and the bottom layer of the coverslip, the phase noise at time t is:

$$\sigma_{\Delta\varphi} = 1/\sqrt{\frac{1}{2\mathrm{SNR}_{\mathrm{top}}} + \frac{1}{2\mathrm{SNR}_{\mathrm{bottom}}}} \tag{4.3}$$

In Figure 4.4, the black line represents actual phase noise and the red line is the theoretical phase noise from equation 4.3. The actual measurement was higher than the theoretical calculation. We assume that the remaining part of the phase noise was coming from environmental factors, such as vibration of the coverslip, slight variation of room temperature, etc.

The phase data was acquired without any lateral scanning because lateral scanning introduced phase noise[144]. If d is the spot size of the beam and Δx is the lateral movement of the beam, then expected standard deviation, $\sigma_{\Delta x}$ is given by [144]:

$$\sigma_{\Delta x} = \sqrt{\frac{4\pi}{3}\left(1 - exp\left(-2\left(\frac{\Delta x}{d}\right)^2\right)\right)} \tag{4.4}$$

The overall phase noise, σ_{phase}:

$$\sigma_{phase} = \sqrt{{\sigma_{\Delta\varphi}}^2 + {\sigma_{\Delta x}}^2} \tag{4.5}$$

If the SNR from the sample is 35dB, then without scanning, the phase noise is 1.13 nm (calculated from equation 4.2). This means, system can measure thickness change

above 1.13 nm for the SNR of 35dB. If lateral motion of the beam due to scanning is 10 µm and the spot size of the beam is 20 µm, then the phase noise due to lateral motion is 55.47 nm (calculated from equation 4.4). The combined phase noise is 55.49 nm (calculated from equation 4.5). So, the source of major portion of phase noise is from lateral scanning.

The expected swelling of the axon of horseshoe crab is 10~30 nm. So, all the desired signals will be buried under phase noise if we scan during data acquisition. Hence, all phase data was acquired without scanning.

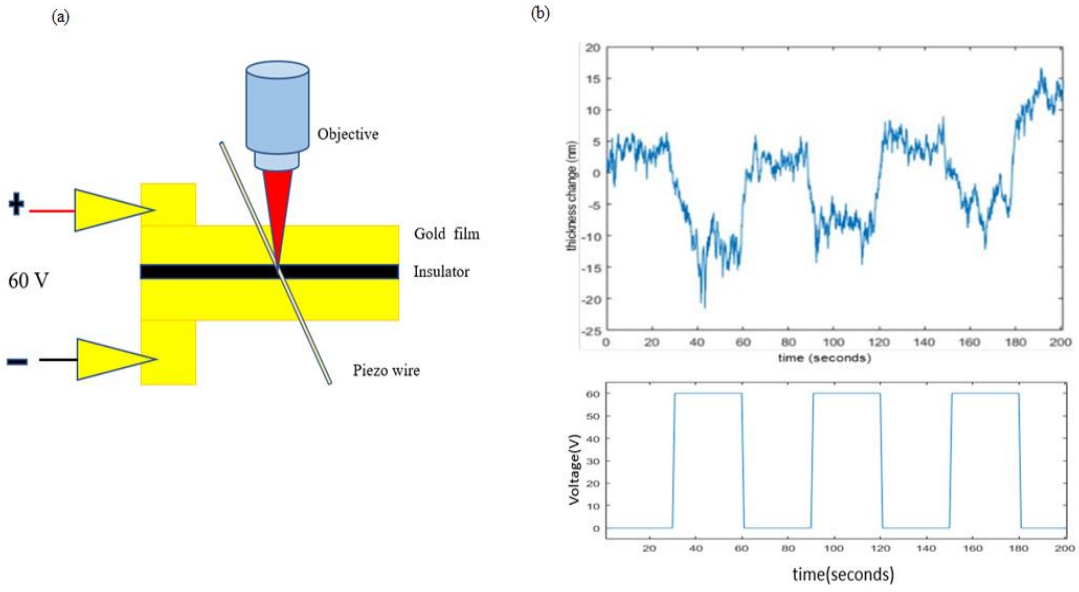

Figure 4.5 Simulation of action potential propagation on a piezo wire. (a) A T shaped gold film was separated by insulator. A 60 V AC voltage was applied across gold film to make changes of thickness of piezo wire. OCT data was acquired over time by positioning beam on top of piezo wire. (b) Top figure shows the thickness changes corresponding to applied voltage on piezo wire which matched with expected thickness change of 15~20 nm.

4.3.2.Physical model of neural activity with piezo wire

An experiment was conducted to verify the capability of the system of detecting sub-nanometer displacements or thickness changes. A piezo wire (diameter 10μm) was used to mimic the activity of action potential. It was made using electrospinning method in collaboration with Jin Nam's lab as described in [145-147].Piezo wire swells if a voltage is applied across it[148]. A piezo wire was placed on top of a gold plate (Figure 4.5a) which was separated by an insulator. Voltage was applied to the gold plates; positive voltage on one part of the gold plate and negative voltage on another part of the gold plate. Piezo wire was making circuit complete to facilitate the flow of current. After applying of the voltage, the current passed through the piezo wire, and thickness of the piezo wire was changed. M- scan OCT data was also collected by positioning OCT beam on top of the piezo wire. The expected thickens change was 15~20 nm, which matches our result. So, this pr-OCT system can measure relative changes in path length of this small magnitude within a reasonable noise margin (Figure 4.5b).

4.3.3.Bulk motion correction

One of the problems of the phase measurement was the movement of the sample over time during data acquisition. As OCT data was taken over time from the sample of a location, there was a need to correct for any bulk motion otherwise phase data could not be compared over time.

4.3.3.1.Algorithm development

The bulk motion was corrected in several steps. First, depth profile was generated from intensity data of a sample by averaging 1024 A-lines (Figure 4.6). Then the noise was calculated by selecting a depth range where there was no information of the sample.

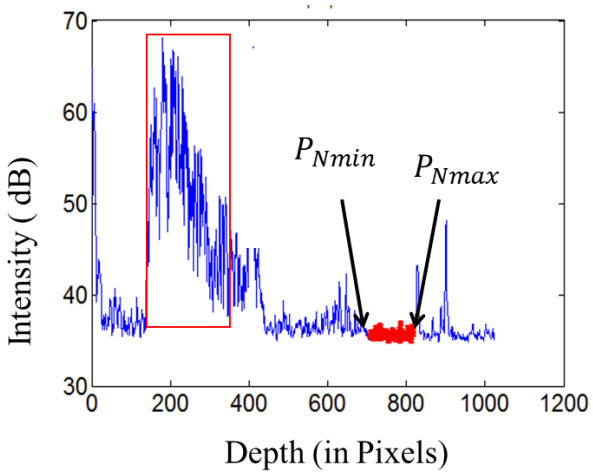

Figure 4.6 Calculation of SNR. The depth profile of a sample. Noise is selected in between depth point of $P_{Nmin}$and P_{Nmax}.

Noise is defined as:

$$I_N(t) = \frac{1}{(P_{Nmax} - P_{Nmin} + 1)} \sum_{P_{Nmin}}^{P_{Nmax}} I(p,t) \tag{4.6}$$

where $I(p,t)$ is the intensity at time t at p[th] pixel, P_{Nmin} and P_{Nmax} are minimum and maximum depth points respectively (Figure 4.6). The SNR is defined as:

$$SNR(p,t) = \frac{I(p,t) - I_N(t)}{I_N(t)} \tag{4.7}$$

Variance of phase is related to SNR[144] by

$$\sigma_{\phi}^{2} = \frac{1}{2\,SNR(p,t)} \tag{4.8}$$

Second, phase difference between consecutive A-lines were calculated as:

$$\Delta\phi(p,t) = \Delta\phi(p,t) - \Delta\phi(p,t-1) \tag{4.9}$$

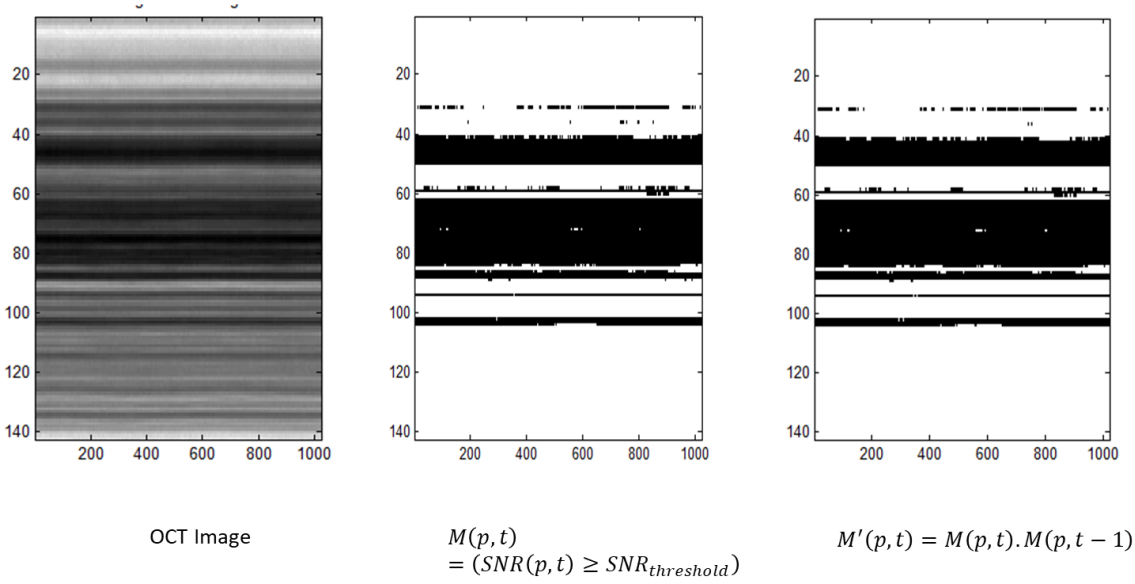

Figure 4.7 Masking of low SNR. (a) M-scan OCT intensity image. (b) SNR thresholding of intensity. A 20 dB threshold was applied to generate mask. (c)Final mask is generated by multiplying mask for same depth point but for time t-1 and t.

The phase variance of consecutive A-line can be derived from equation 4.8 as:

$$\sigma_{\Delta\phi}^{2} = \sigma_{\phi}^{2}(p,t) + \sigma_{\phi}^{2}(p,t-1) \tag{4.10}$$

A weighted mask which is inversely proportional to phase variance is defined as (using equation 4.8 and 4.10):

$$w_{\Delta\phi}(p,t) = \frac{1/2}{\sigma_{\Delta\phi}^{2}} = \frac{SNR(p,t) + SNR(p,\,t-1)}{SNR(p,t).\;SNR(p,t-1)} \tag{4.11}$$

Third, the SNR mask, M (p, t) is generated by thresholding SNR from intensity data (Figure 4.7). This mask is extended for consecutive A-line to make sure SNR is high for both A-lines.

$$M'(p,t) = M(p,t).\ M(p,t-1) \tag{4.12}$$

Fourth, after applying weighted mask as well as SNR mask for sample's region of interest ($P_{b\,max}$ to $P_{b\,min}$),bulk motion correction factor can be found as:

$$\Delta\phi(t) = \frac{\sum_{P_{b\,min}}^{P_{b\,max}} w_{\Delta\phi}(p,t)\ .\ \Delta\phi(p,t)\ .\ M'(p,t)}{\sum_{P_{b\,min}}^{P_{b\,max}} w_{\Delta\phi}(p,t)\ .\ \ M'(p,t)} \tag{4.13}$$

Bulk motion corrected phase can be found as:

$$\phi'(p,t) = \phi(p,t) - \Delta\phi(t) \tag{4.14}$$

Now the phase difference in consecutive A-lines is:

$$\Delta\phi'(p,t) = \phi'(p,t) - \phi'(p,t-1) \tag{4.15}$$

Finally, phase difference for two depth layers with separation of Δp can be found as:

4.3.4.Suppression of phase noise for low SNR

The theoretical phase noise ($\sigma_{\Delta\varphi}(\mathrm{p},\mathrm{t})$) was calculated for two layers separated by Δp from equation 4.3. Then the average phase difference ($\theta(p)$) was calculated from the baseline of $\Delta\phi''(p,t)$(for example, 750 to 800 ms of Figure 4.8a). Minimum detectable noise limit was $\sigma_{\Delta\varphi} \pm \theta(p)$.

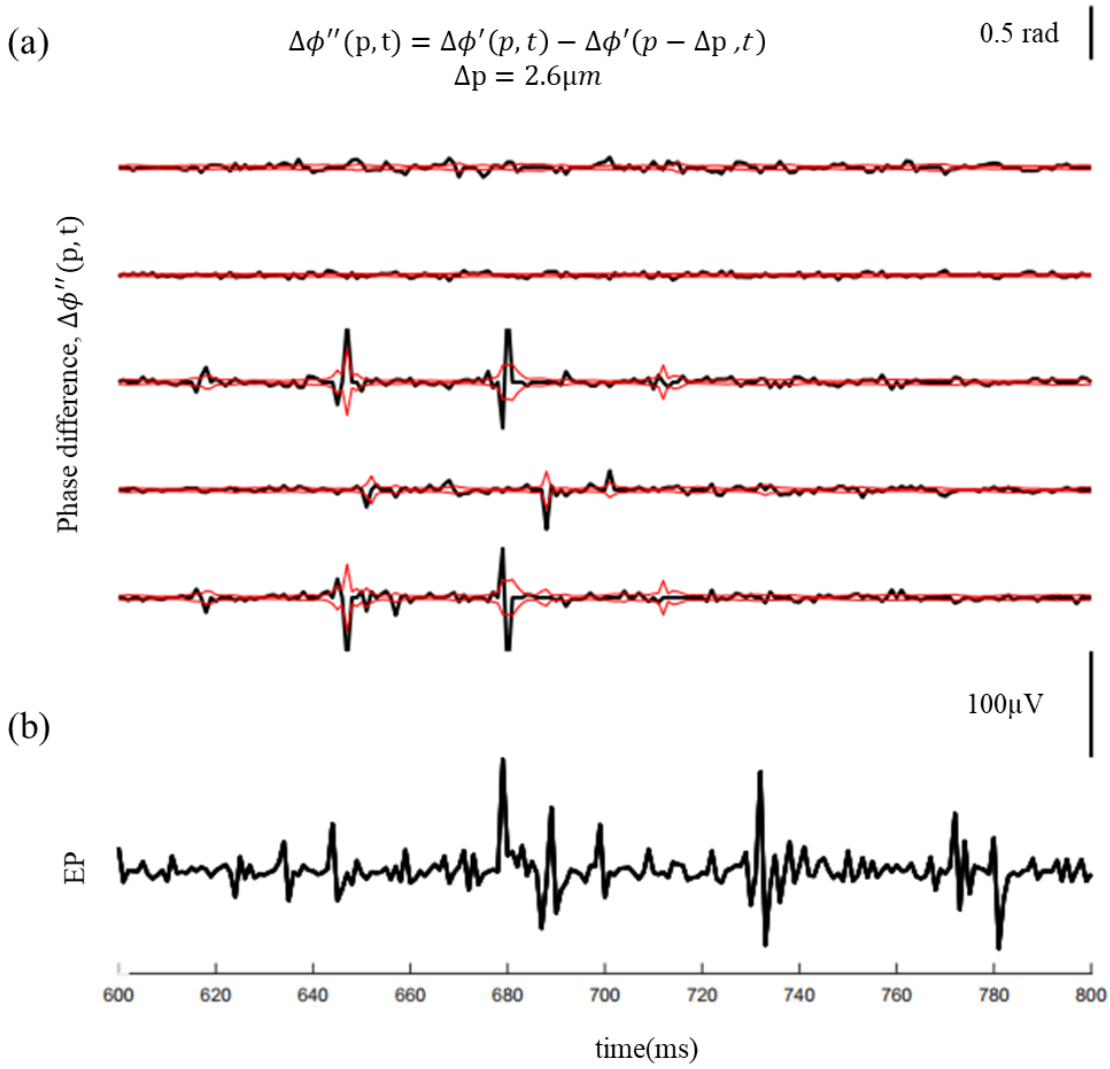

Figure 4.8 Phase noise suppression. (a) Minimum detectable phase line was calculated from the SNR of 2 layers (red lines). (b)Electrophysiology from axon

In Figure 4.8a, the red lines are the theoretical phase noise limit line. Any phase fluctuation inside the two red lines are noise, not from any activity and noise was suppressed by making $\Delta\phi''(p,t)$ to zero. The red lines had a high amplitude when there were activities (for example at 680 ms of Figure 4.8a) because of the decrease of intensity for the reduction of backscattered light for the reduction scattering in axon due to neural activity.

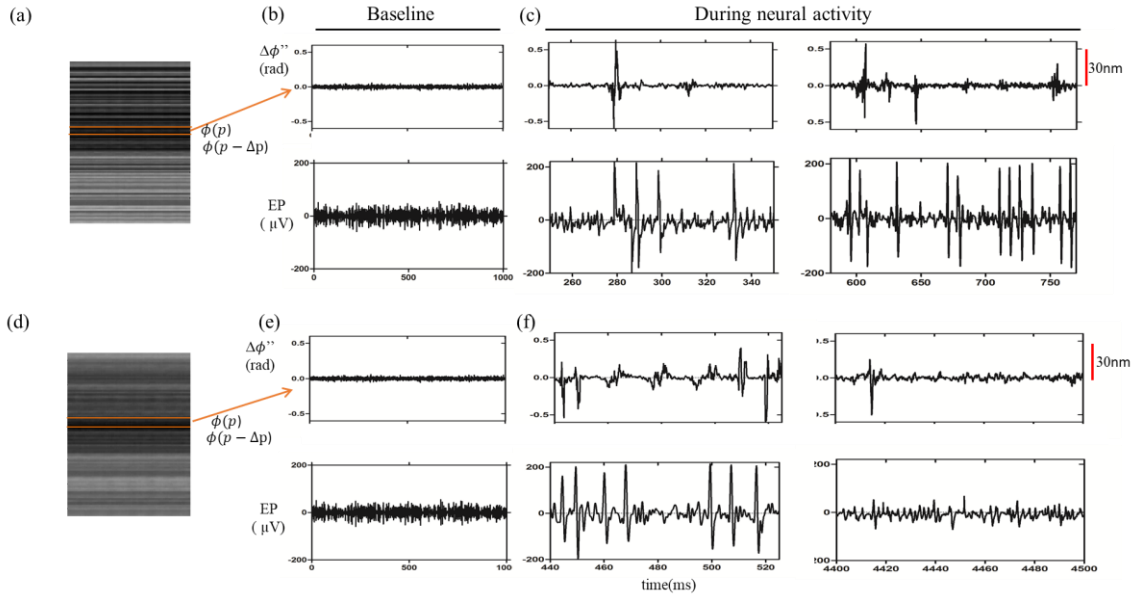

Figure 4.9 Detection of neural activity. (a, d) Intensity M-scan images. (b, e) No neural activity and no change of phase. (c & f) neural activity correlate with electrophysiology.

4.3.5.Phase changes during neural activity

Phase difference was taken from two depth layers separated by 2.6 μm. During no activity period, there was no change of phase (Figure 4.9b, e). When there were neural activities, there were changes of the phase difference or swelling of axon between 10~30 nm (Figure 4.9c, f).

4.3.6.Depth-resolved phase measurement

Physical distance of each layer is 1.3 μm, and if there is any activity in one layer, it should also affect in other layers because the diameter of the axon is 3 to 10 μm. In other words, if there is a swelling of the axon in one layer, there should be swelling of the axon in other layers too. From the center of the axon, the direction of swelling at the top part is in one direction and the bottom part is in another direction. So, there is a correlation between consecutive depth layers during action potential propagation.

The correlation of 2 depth layers (d1 and d2) was calculated as:

$$r_{d_n,d_{n+1}} = \frac{max\{corr(d_1,d_2)\}}{\sqrt{max\{corr(d_1,d_1)\}\cdot max\{corr(d_2,d_2)\}}}$$
$$corr(x,y) = FFT^{-1}\{FFT\{x\}\cdot\overline{FFT\{y\}}\} \quad (4.15)$$

where the data length of d1 or d2 was 1.6ms, which was the half the duration of action potential (Figure 4.10).

If two layers are correlated, then we marked with a red color (Figure 4.11a). A heatmap of correlation was also generated (Figure 4.11b). Two thresholds were used for correlation map: first, if the correlation was not greater than 2.6 μm in consecutive depth layers, it was not put on correlation heatmap. Second, if correlation length of a phase difference line was not greater than 3 ms (duration of a single action potential was 3 ms), it was also discarded from correlation map.

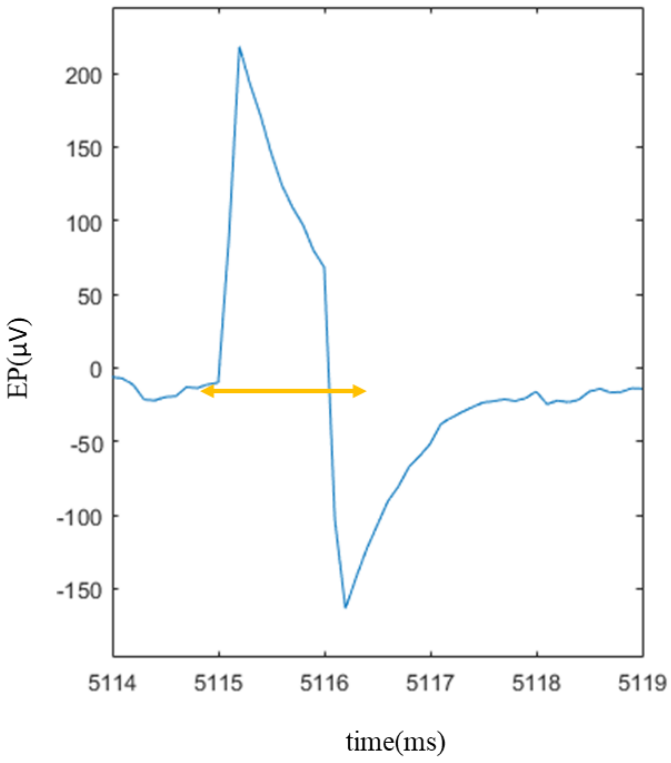

Figure 4.10 Data length for correlation analysis is 1.6ms, which is the half duration of an action potential.

The Figure 4.11 shows that when there is an action potential, there is a thickness change of different depth layers. The thickness change in different axial locations indicating those axons are active during stimulation. Black dots in correlation map indicate correlation among layers.

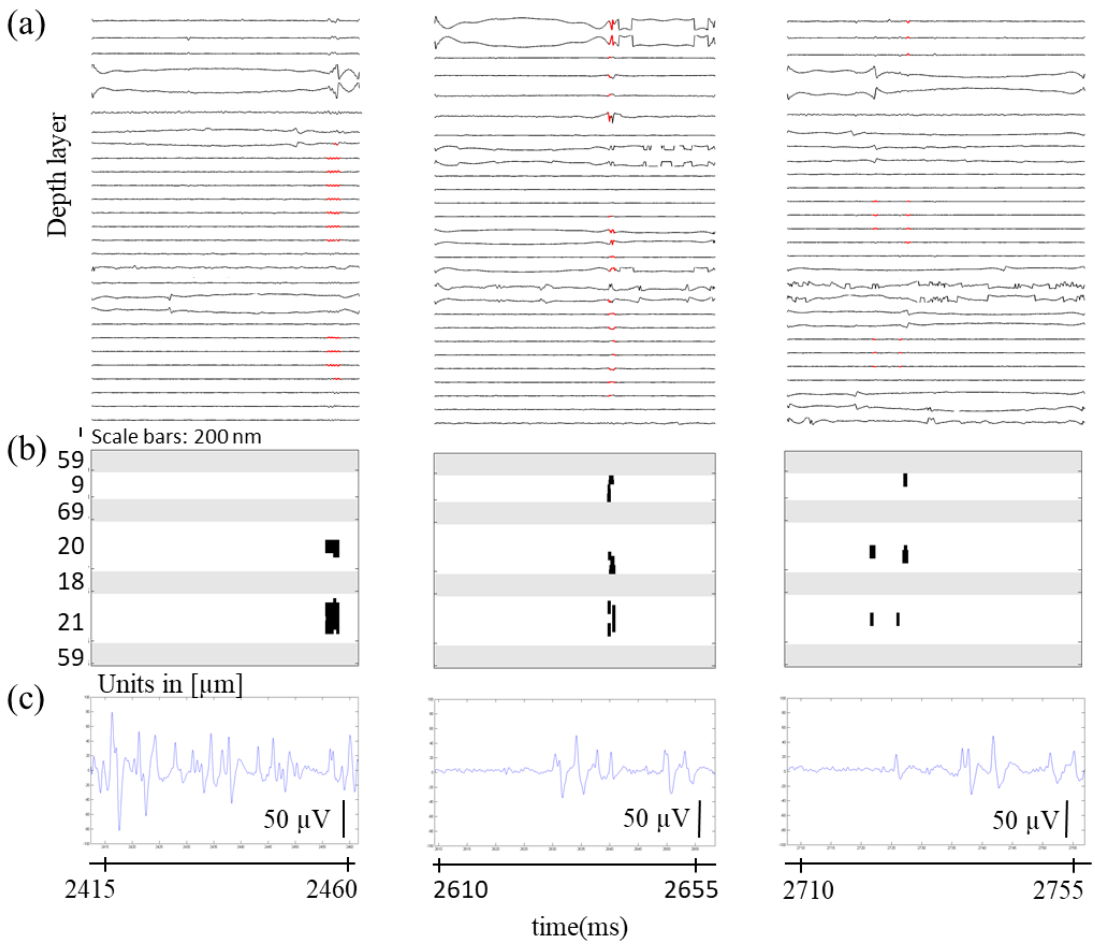

Figure 4.11 Depth-resolved phase change. (a) Axon swelling in different depth layers. (b) correlation map corresponding to swelling in different layers. (c) Electrical recording by suction electrode.

4.3.7.Control experiment-cold block

The cold block experiment was performed by flowing cold salt water to a small section of nerve in cold block chamber. The frozen nerves exhibit higher resistance than normal condition, and the conduction of impulses decrease to almost zero [149, 150]. The

nerves started to freeze at the negative temperature. No action potentials should be observed under these conditions, even when stimulated by UV light.

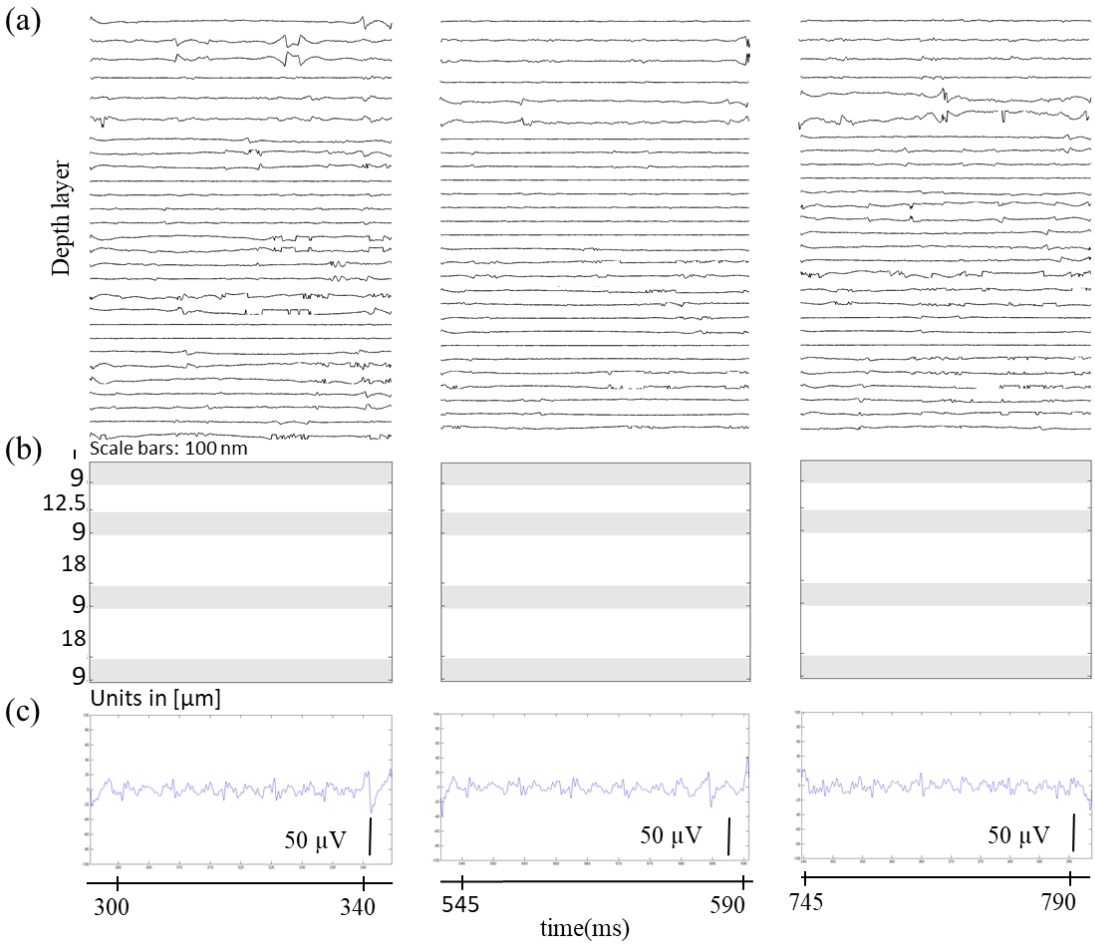

Figure 4.12 Control experiment in cold block. (a) Axon swelling in different depth layers. (b) correlation map corresponding to swelling in different layers. (c) Electrical recording by suction electrode.

There were no action potentials in stimulated optic nerves (Figure 4.12c). In depth-resolved phase difference (Figure 4.12a), there were no phase changes in consecutive layers, and correlation heatmap had no black dots.

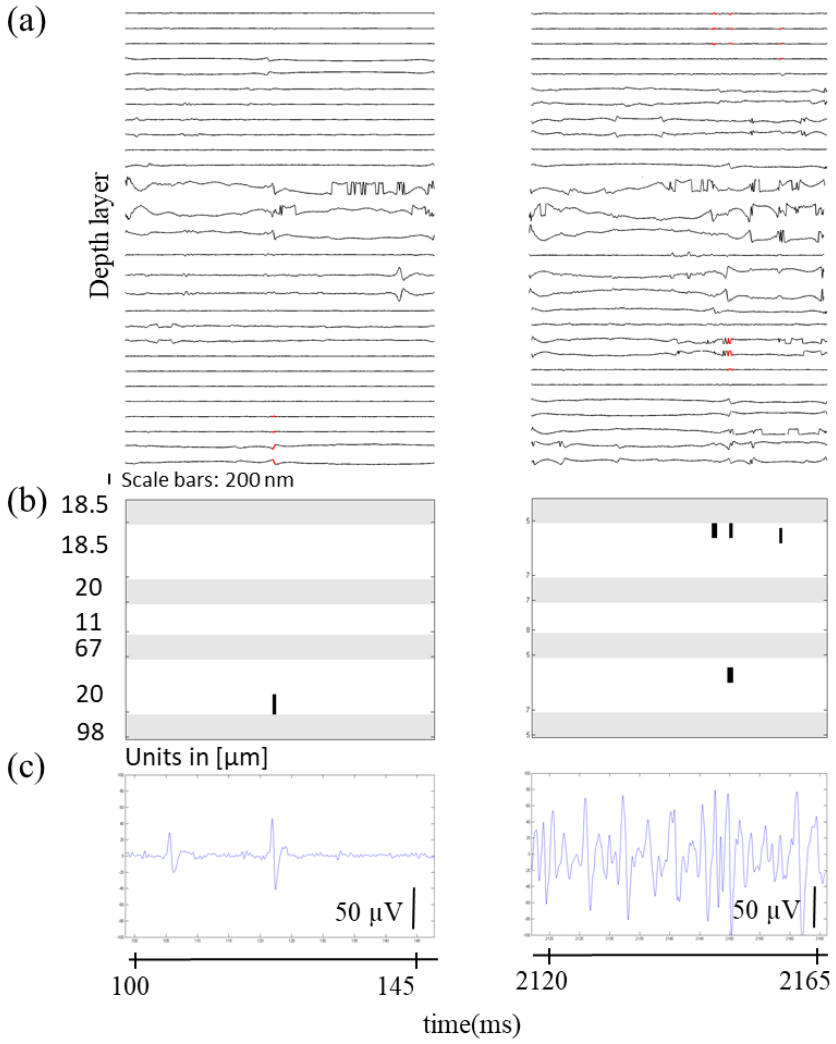

Figure 4.13 After flowing of hot water, action potential. (a) Axon swelling in different depth layers. (b) correlation map corresponding to swelling in different layers. (c) Electrical recording by suction electrode.

4.3.8.Recover from no-activity to activity-hot block

To recover from no-activity to activity, hot water has flowed into the optic nerve chamber. The nerves started to conduct again at room temperature(22°C). Figure 4.13c shows the activity after stimulation. We found swelling of the axons when there was an action potential (Figure 4.13a-b).

4.4.Conclusion

In this study, phase-resolved optical coherence tomography has been demonstrated to be capable of detection of neural activity. The control experiment with piezo wire demonstrated that pr-SDOCT was capable of detecting thickness change in nm range. We found the changes of the thickness of axon of 10~30 nm correlated with the propagation of action potential. During the cold block, there were no activities, hence no thickness changes. By flowing the hot water, the axons were reactivated, and we detected the swelling of axon during propagation of action potential. Current and future improvement efforts are focus towards the improvement of detection sensitivity of this pr-OCT and detection of activity along nerves.

Chapter 5: Detection of fast optical changes in neural activity during epileptiform activity using phase-resolved optical coherence tomography

5.1.Introduction

In the last chapter, we described the detection of thickness change from isolated axon bundle of the horseshoe crab. This chapter focuses on detection of neural activities from mammalian physiology relevant size of neurons in murine brain slice. The *in vitro* mouse seizure model was used to generate neural activity. The phase-resolved OCT system detected phase changes during action potential propagation in CA3 of the hippocampus.

Current methods of detection of neural activity are based on electrophysiology, which requires direct or near direct contact [128-131, 151-154] , or fluorescence-based techniques, which require the introduction of reporter molecules, raising a concern of toxicity [129, 132, 155].The neural activity can also be detected indirectly through neurovascular coupling[156-158]. In 1949, Hill and Keynes found an increase in optical scattering during action potential propagation in a crab nerve in Ringer's solution[159]. In 1950, Hill first discovered a volume change of 1100 $\mu m^3/cm^2$ in the axonal membrane for a single impulse in cuttlefish [134]. Laser interferometry was later used to measure the thickness change of a nerve during action potential propagation[133, 160]. To enhance the signal, the nerve was coated with gold particles to increase the nerve surface reflectivity, and for nerve bundles that were 180 μm in diameter, transient displacements of 0.3 to 2.5 nm were found [133]. Using a piezoceramic bender with hydrostatic pressure

measurements, Tasaki and Byrne found that the length contraction of a nerve did not entirely correspond with its thickness change, indicating an overall volume change of the nerve[136, 137]. All the results reveal that there is no direct relationship between axon diameter and the magnitude of this deflection.

The pr-OCT was used several times to detect slight transient volume change accompanying action potential propagation [95, 96, 99, 139, 140]. The bulk of this study was performed in the squid giant axon, known to be the largest single nerve cell. This is a perfect animal model for initial testing because the single cell has such a large diameter and can be isolated to simplify detection of neural activity. However, the separate study of smaller nerves is necessary for future utility in human brain research.

Here we present our study of detection of fast optical changes during neural activities in the murine brain slice. Previous studies with OCT mostly used nerve with large size[95, 96, 99, 139, 140].In our study, we used murine brain slice with multiple axons with physiology relevant size(1 to 10 μm) to detect swelling during neural activity[161].

5.2.Materials and methods

5.2.1.System description

The OCT system uses a broadband laser (Femtolasers, Inc., Integral OCT) with a center wavelength of 804 nm and a bandwidth of 170 nm (Figure 5.1). The sample arm is incorporated into an upright microscope (Olympus BX61W). The OCT beam underfilled

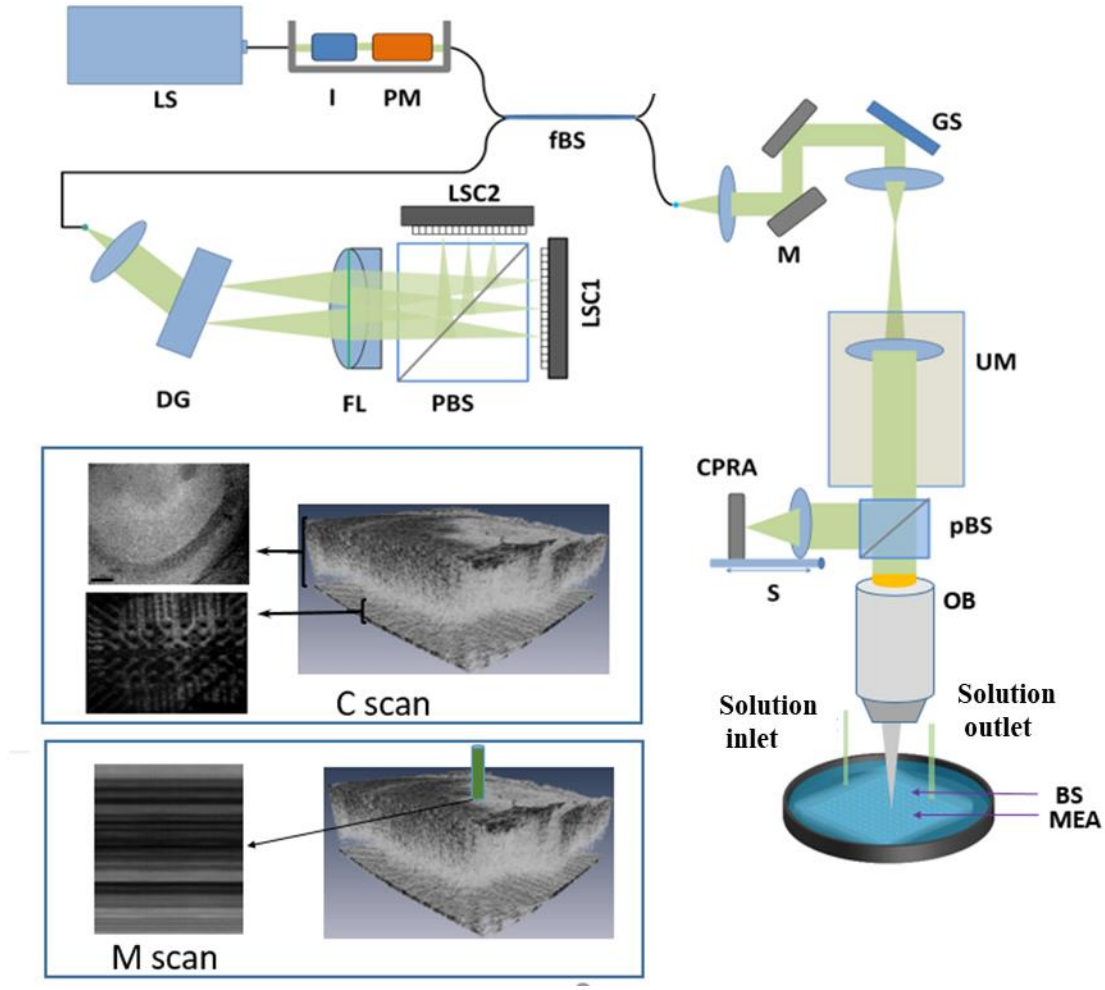

Figure 5.1 Spectral domain OCT system. LS: light source (Ti:Sapph 800nm laser), I: isolator, PM: polarization modulator, fBS: fiber-based beam splitter, M: mirror, GS: galvo scanner, UM: upright microscope, pBS: plate beam splitter, nCPRA: near common- reference arm, OB: 20X water immersion objective lens (N.A. 0.50) ,DG: diffraction grating, FL: focusing lens, PBS: polarization beam splitter, LSC: line scan camera, S: moving stage, BS: Brain Slice, ACSF: artificial cerebrospinal fluid, MEA: Multi-electrode Array.

the back-aperture of a 20X water-immersion objective (NA = 0.5) by 40% to maintain an OCT depth range of at least 500 µm. The details are discussed in section 4.2.3.

5.2.2.Sample preparation

JAX C57/BL6J wild-type mice between postnatal day P15 to P25 of either sex were used for the experiment. Mice were anesthetized with isoflurane, quickly decapitated, and the brain was rapidly removed and submerged in ice-cold low [Ca2+], high Mg dissection solution. 300 µm thick horizontal brain slices were made using a Leica 2100S vibratome in oxygenated ice-cold dissection solution. Slices were then moved to a holding chamber and incubated in oxygenated artificial cerebrospinal fluid (ACSF) at 32°C for 1hr. After an hour, the holding chamber was moved from the incubator to the table top allowing the solution and slices to come to room temperature for 30 minutes.

5.2.3.Electrophysiology data recording and processing

Recordings were done on a Multichannel Systems 60-channel perforated multielectrode array (MEA). MEA consists of an 8x8 TiN electrode grid with 200 µm spacing between electrodes and 30 µm electrode diameter. Brain slices were positioned such that the electrode grid could record from the entire hippocampus. LFP recordings from the hippocampus were done under constant ACSF perfusion at ~4mL/min at 32°C for 15 minutes. Epileptiform activity was then induced through bath application of 100 µM 4-AP.

Data were acquired using MC Rack software (MultiChannel Systems) and exported to MATLAB (MathWorks) for further processing. Data from all 60 MEA

channels were collected at 10 kHz. Bandpass (0.1 - 7 Hz) but only channel near the OCT beam was processed. A 2nd order Butterworth filter was applied to remove OCT-induced electrical noise from the LFP.

5.2.4.OCT data recording and processing

OCT data was acquired at the A-line rate of 10 kHz from a specific location of CA3 region of the hippocampus (see inset of Figure 5.1, M-scan) without lateral scanning. Lateral scanning introduce phase noise as describes in section 4.3.1. The duration of the LFP is 200~1200 ms. Therefore, at the acquisition speed of 10 kHz (time resolution of 0.1 ms), action potential propagation at a single observation point has a temporal duration equivalent to 2000 to 12000 depth scans, which are enough to represent phase changes due to propagation of action potential. The high acquisition speed also reduces the system sensitivity of the detection of thickness change as describes in section 4.2.4.

The beam was positioned in such a way that it did not directly hit the electrode to avoid huge reflection from electrodes. The spectral data was saved simultaneously with electrophysiology data. To have uniform wavenumber spacing, linear interpolation was performed to the nonlinear k-space sampled spectral data. The FFT from wavenumber to the spatial domain was performed, and depth-resolved structural information, as well as phase information, was retrieved.

5.3.Results and Discussion

5.3.1.Characterization of pr-OCT phase measurement

Phase measurement of the pr-OCT system was characterized in two steps. In the first step, a coverslip was used as a sample to check the phase noise of the system. The details are described in section 4.3.1.

The detection of thickness change in nanometer range was described in section 4.2.2. for the piezo wire stimulation. This proved that system was capable of detecting thickness changes in millisecond resolution time scale.

5.3.2.Bulk motion correction of brain slice

The OCT data was acquired by flowing ACSF as well 4-AP solution. The brain slice could move up or down due to change of flow of the solution (solution level of the MEA well is increased or decreased). So, a correction algorithm is necessary to adjust the movement of brain slice. This will ensure the comparison of data over time.

5.3.2.1.Algorithm development

The detail of the algorithm was discussed in section 4.3.3.1, and bulk motion correction factor can be found as:

$$\Delta\phi(t) = \frac{\sum_{P_{b\,min}}^{P_{b\,max}} w_{\Delta\phi}(p,t)\,.\;\Delta\phi(p,t)\,.\;M'(p,t)}{\sum_{P_{b\,min}}^{P_{b\,max}} w_{\Delta\phi}(p,t)\,.\;\;M'(p,t)} \tag{5.3}$$

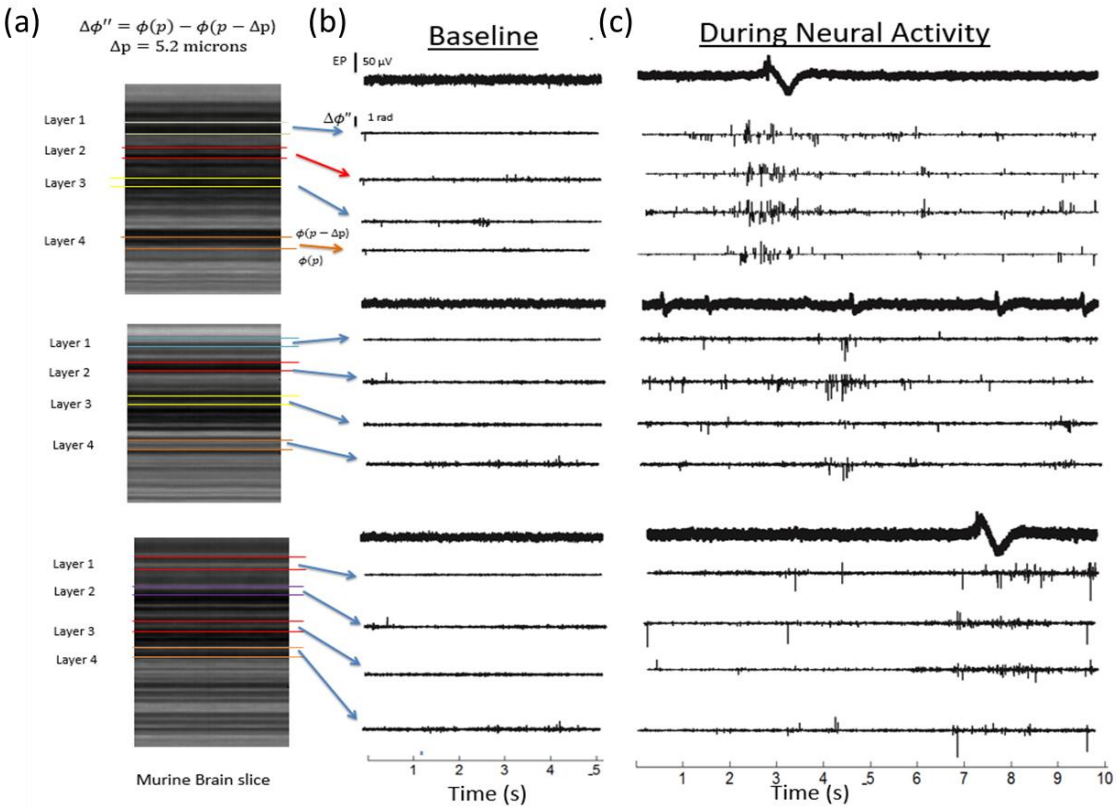

Figure 5.2 Detection of neural activity. (a)Intensity image of M-scanned brain slice. Layer 1-4 were selected based on high SNR (>20 dB). (b)Baseline(ACSF) electrophysiology time trace and corresponding phase difference. The phase difference had no large fluctuation but there were small fluctuations due to spontaneous activity (c) During neural activity in 4-AP, fluctuations of phase were higher than baseline and there was a correlation between EP and phase fluctuations.

Bulk motion corrected phase can be found as:

$$\phi'(p,t) = \phi(p,t) - \Delta\phi(t) \tag{5.4}$$

Now phase difference in consecutive A-lines is:

$$\Delta\phi'(p,t) = \phi'(p,t) - \phi'(p,t-1) \tag{5.5}$$

Finally, phase difference for two depth layers with separation of Δp can be found as:

$$\Delta\phi''(p,t) = \Delta\phi'(p,t) - \Delta\phi'(p - \Delta\mathrm{p}\,, t\,) \tag{5.6}$$

5.3.3.Phase fluctuation during neural activity

The bulk motion correction algorithm was applied to both the baseline and the epileptiform of activities data. A 20 dB threshold was applied to mask out the low SNR data. The phase noise for 20 dB is 6.36 nm or 0.1 rad. Phase difference was taken from two depth points separated by 5.2 μm (Figure 5.2). From M-scanned intensity data, several layers were selected where SNR was higher than 20 dB (Figure 5.2a). During the baseline period (Figure 5.2b), there were very low phase fluctuations, which originated from the spontaneous activity of the neurons.

During the epileptiform activity (Figure 5.2c), the phase fluctuations were higher than the baseline. The top and the bottom data of Figure 5.2c had higher EP spike(seizure) than middle figure(pre-seizure). The density and amplitude of phase fluctuations were higher during seizure activation than pre-seizure. The EP and phase fluctuation were correlated well in time. Thus, phase fluctuation can be used as a biomarker for the detection of neural activities.

5.3.4.Depth resolved detection of neural activities

Phase difference was taken from all the depth layers where SNR was greater than 20 dB (Figure 5.3a-b). During the baseline (Figure 5.3a), LFP was in between -20 μV to

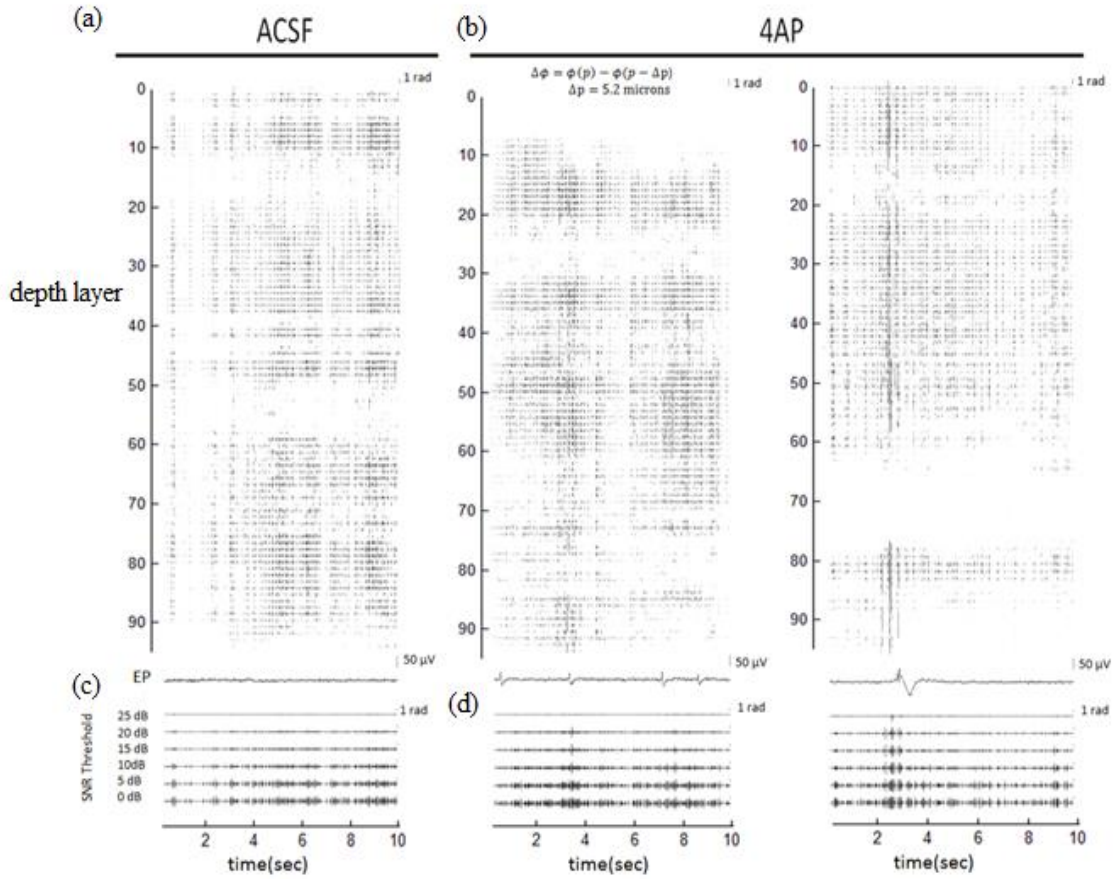

Figure 5.3 Phase fluctuations during neural activity. (a-b) Phase difference is taken for whole depth section of brain slice. (c-d) For each time point, maximum phase deviation from zero is taken for different SNR thresholds. For low SNR, phase fluctuation is high even in ACSF because of high phase noise. As the SNR threshold increases, phase fluctuation can only be seen during activity.

20 µV. There was a small number of action potentials during baseline, and there were changes of the phase difference. The area with <20 dB SNR was moved out from phase fluctuation calculation (see depth layers between 10~20 and 52~58 of Figure 5.3a), which had a phase noise of 0.1 rad. During neural activity (Figure 5.3b), phase fluctuations were higher than the baseline, and in different depth layers. These phase fluctuations correlated with EP.

Figure 5.3c-d demonstrated the effect of SNR thresholding on phase fluctuations. As per equation 4.2, the phase noise will be low if SNR is high and vice versa. To show SNR thresholding effect, first, all depth layers phase difference ($\Delta\phi''$) was combined by:

$$\varphi(t) = \max(|\Delta\phi''(z,t)|), \text{ where depth layer}, z = 1\ to\ n.$$

where *n* is the total number of depth layers and $\varphi(t)$ is the combined phase fluctuation of all layers. Second, different SNR thresholds were applied from 0 dB to 25 dB with an increment of 5 dB and $\varphi(t)$ was calculated over time.

From Figure 5.3c, phase fluctuations were observed even in the baseline for 0 dB thresholding. As the SNR threshold was increased, phase fluctuations were reduced. At SNR threshold of 5 dB, the phase noise is 0.56 rad or 35.8 nm. Therefore, both ACSF and 4-AP data showed phase fluctuations, which mostly originated from noise. At SNR threshold of 15 dB, the phase noise is 0.177 rad or 11.32 nm. As the amount of phase noise from the data is reduced, the difference of phase fluctuations between ASCF and 4-AP are prominent. At 20 dB threshold (phase noise is 0.1 rad or 6.36 nm), there were almost no phase fluctuations in the baseline. But in Figure 5.3d, phase fluctuations were observed at 20 dB thresholding, that were coming from neural activities. At 25 dB of threshold (phase noise is 0.056 rad or 3.58 nm), phase fluctuations can be observed only during seizure activation (high amplitude of LFP). Therefore, phase fluctuations, which corresponds to swelling of axons during neural activities, can be detected using the phase-resolved measurement of OCT.

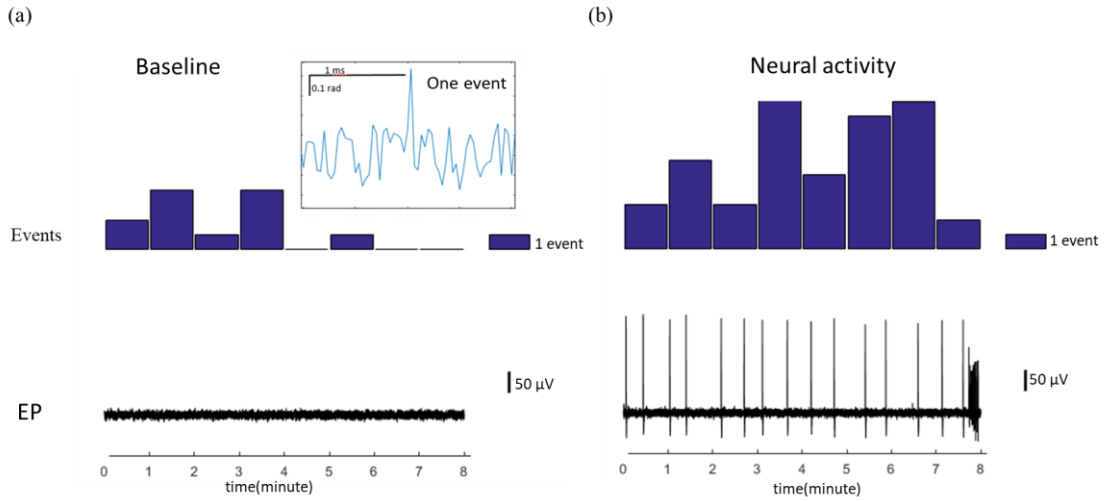

Figure 5.4 Detection of events. After masking out phase data for lower than 20 dB SNR, each event was detected for crossing of ±0.3 rad of phase changes from baseline. The length of the bin was 60 s. (a) during baseline period, there were spontaneous activities. (b) During neural activities, the detected events were higher than baseline period.

5.3.5.Event comparison between ACSF and 4-AP

The number neural activity events were compared between ACSF(baseline) and 4-AP (neural activities). To calculate events, a SNR threshold of 20 dB was used to remove low SNR data. An event is counted if the phase difference exceeds ±0.3 rad, and a bin of 60 s is chosen to show the results (Figure 5.4). In an active murine brain slice, there were spontaneous activities even during baseline, and a small number of events were found (Figure 5.4a). During the neural activities, the number of events was higher than the baseline (Figure 5.4b) because of structural changes of nerves in the higher number.

5.4.Conclusion.

In this study, phase-resolved optical coherence tomography has been demonstrated to be capable of detection of neural activity. We found the changes of phase fluctuation corresponding to changes of LFP. To best of our knowledge, this is the first demonstration of propagation of action potential during epileptiform of activities in murine brain slice. We also found the higher number of phase fluctuation during neural activity from seizure activation than the baseline. Current and future improvement efforts are focus towards the improvement of detection sensitivity of this pr-OCT and detection of multi-unit activities.

Chapter 6: Identification of optical changes during sharp wave ripple activation in *in vitro* mouse hippocampus using optical coherence tomography

6.1.Introduction

In chapters 2 and 3, we discussed detection of neural activity during seizure activation in the murine hippocampal CA1, CA3, and DG area through changes of optical intensity and attenuation coefficient. In the previous chapter, we detected neural activity through phase fluctuation in the hippocampal murine brain slice. In this chapter, we detected optical intensity changes during sharp wave ripple activation from the localized area of hippocampal CA1 as a first step to detect neural activity from a single action potential.

Sharp waves(SPWs) are large amplitude negative wave in CA1 stratum radiatum associated with a fast-oscillatory pattern (110-220 Hz) of the local field potential(LFP) in the CA1 pyramidal layer, known as “ripples”[162-166]. SPW-R, formed by the coupling of SPWs and ripple, have been found in the hippocampus of every investigated species so far are the most synchronous events in the mammalian brain[162, 167]. SPW-R is a cognitive biomarker for memory consolidation and planning[108], and pathological fast ripples also observe during epilepsy[168].

The self-organized burst of activity in the CA3 region produces a SPW sink in the apical dendrites of the CA1 pyramidal neurons and discharge interneurons. A short-lived

fast oscillation is generated by the interaction between the discharging pyramidal cells and interneurons. This oscillation can be detected as fast LFP oscillation in the CA1 pyramidal layer [169]. These synchronous events are volatile and can be transformed from the physiological event into pathological interictal epileptic discharge for the alteration of the recruitment process[170, 171].SPW-R is a cooperative event, and there is no special change of spikes of individual pyramidal cells, however, a large fraction of neurons fire together. Therefore, LFP events from these neurons correlate between individual neurons and population behavior[166].

In vitro slice method offers a unique advantage to study the cellular and network mechanism of cooperative population activities[172].Calcium imaging is used to detect SPW-Rs in CA1 but needs calcium indicator dyes[173]. Functional Magnetic Resonance Imaging(fMRI) can reveal large-scale signatures of SPW-R only[174]. Electrophysiology is a reliable method to collect LFP and there are various algorithms to detect SPW-R but it is inherently invasive and has a low spatial resolution[175-178]. Therefore, there is a need for a method capable of detecting SPW-R non-invasively and label-free manner with high spatial resolution.

Optical coherence tomography is a label-free imaging technology which can generate 2D or 3D image of tissue with a high spatial resolution[120, 179]. In this study, we used SD-OCT, to our knowledge for the very first time, to detect the SPW-Rs by inducing SPW-Rs in CA1, quantifying the changes of backscattered intensity in murine brain slice and validated with gold standard electrophysiology.

6.2.Materials and methods

6.2.1.Animals

All experiments and procedures were performed according to University of California, Riverside Institutional Animal Care and Use Committee-approved protocols. Wild-type (Jackson Laboratory, C57BL/6J, stock number 000664) mouse colonies were bred and maintained in house to generate pups for this study. Both male and female mice were used in this study.

6.2.2.Brain slice preparation for ripple activation

Postnatal day (P) 25-40 mice were anesthetized with isoflurane and quickly decapitated. The brain was rapidly removed and submerged in ice-cold, artificial cerebrospinal fluid (ACSF) with carbogen (95%-5% O2-CO2) gas continuously applied. 400 µm thick horizontal whole brain slices were made in the dissection solution with a Leica 1200S vibratome. Slices containing hippocampus were recovered in oxygenated ACSF for a minimum of 2hrs at 32^0C until use. Our standard ACSF contained (in mM): 119 NaCl, 2.5 KCl, 26 NaHCO3, 1 NaH2PO4, 1.3 MgCl2, 2.5 CaCl2, 10 D-glucose. Brain slices were continuously perfused during our recordings (see inset of Figure 6.1)with ACSF (8 ml/min flow rate). ACSF was maintained at pH 7.4 by continuous oxygenation with carbogen gas mixture. To induce sharp-wave ripples, ACSF during recordings had KCl concentration raised to 5 mM. All chemicals were obtained though Fisher Scientific unless otherwise specified.

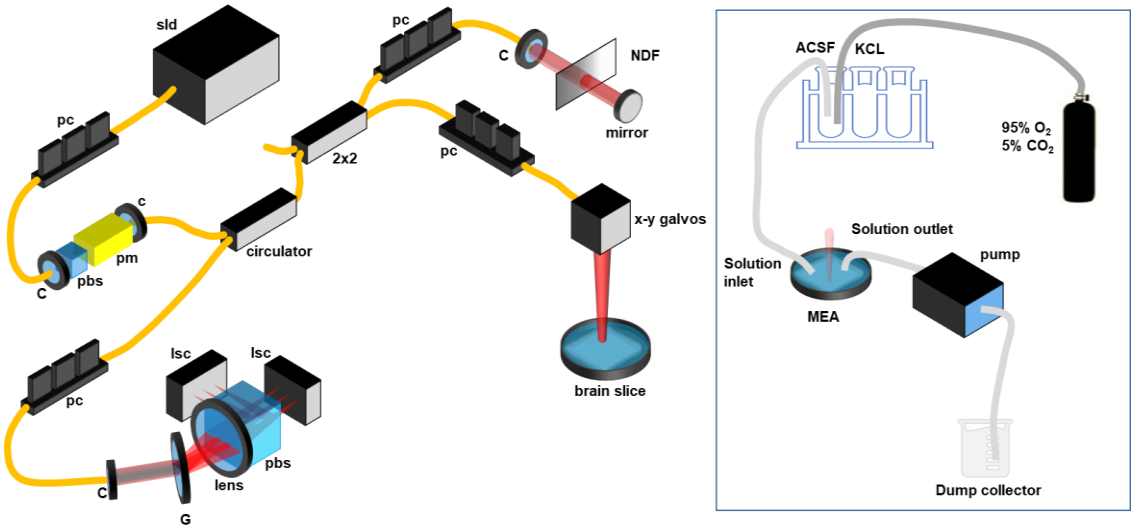

Figure 6.1 System diagram. sld: superluminescent diode MEA: multi-electrode array, pc: polarization controller, pm: polarization modulator, G: gratting, NDF: neutral density filter, lsc : line scan camera, C: collimator, pbs: polarization beam splitter. Inset diagram demonstrates flow of solution into brain slice. The gas (95%-5% O_2-CO_2) flows into solution, then oxygen rich solution flows into brain slice, and a pump collect un-oxygenated solution.

6.2.3.OCT Imaging system

The SD-OCT system (Figure 6.1) utilized broadband, low-coherence light source consisting of two superluminescent diodes (SLD), one centered at 1295 nm with a FWHM bandwidth of 97 nm (Thorlab Inc), and the other centered at 1350 nm with a FWHM bandwidth of 48 nm (Denselight Semiconductor Pte Ltd) resulting a combined bandwidth of 120 nm centered at 1298 nm. The system resolution was 8 nm and 20 nm axially and laterally, respectively. The detail description of the system is in section 2.2.3.

6.2.3.1.OCT data acquisition and processing

OCT cross-sectional images were acquired at the A-line rate of 30 kHz, and each cross-sectional image composed of 256 A-lines. Acquisition time for each cross-sectional

image was 8.53 ms, and continuous 8 images were taken from CA1 region (Figure 6.2a-b). There was a gap of 51.8 ms before the acquisition of the next frame. An imaging depth of 2 mm was obtained with 6.7 mW of incident power on brain slice. To have uniform wavenumber spacing, linear interpolation was performed to the nonlinear k-space sampled spectral data. The fast Fourier-transformation(FFT) from wavenumber to the spatial domain was performed, and depth-resolved structural information was retrieved. The images were displayed on an inverse log scale as well. A depth-dependent sensitivity data was measured, and removed by multiplying each A-line by a calculated correction curve to compensate for the decrease of sensitivity as a function of depth for the finite resolution of the spectrometer.

The noise for each A-line was different due to reflection from electrodes of MEA and generated by averaging intensity of 20 pixels from the top of the A-lines where there was no brain slice. A noise-free A-line was obtained by subtracting noise from each A-line. The first 5 A-lines from each frame was excluded to avoid image distortion due to the instability of the galvo mirror in new position. Then an area of 300 μm X 200 μm was selected from each cross-sectional image to calculate average intensity of each frame. Hence, each OCT intensity data point represents ripple information for the duration of 8.53 ms. As the duration of the ripple is around 40 ms, the time resolution of cross-sectional image provides 5 points to represent a ripple, which is sufficient if we average across many ripples.

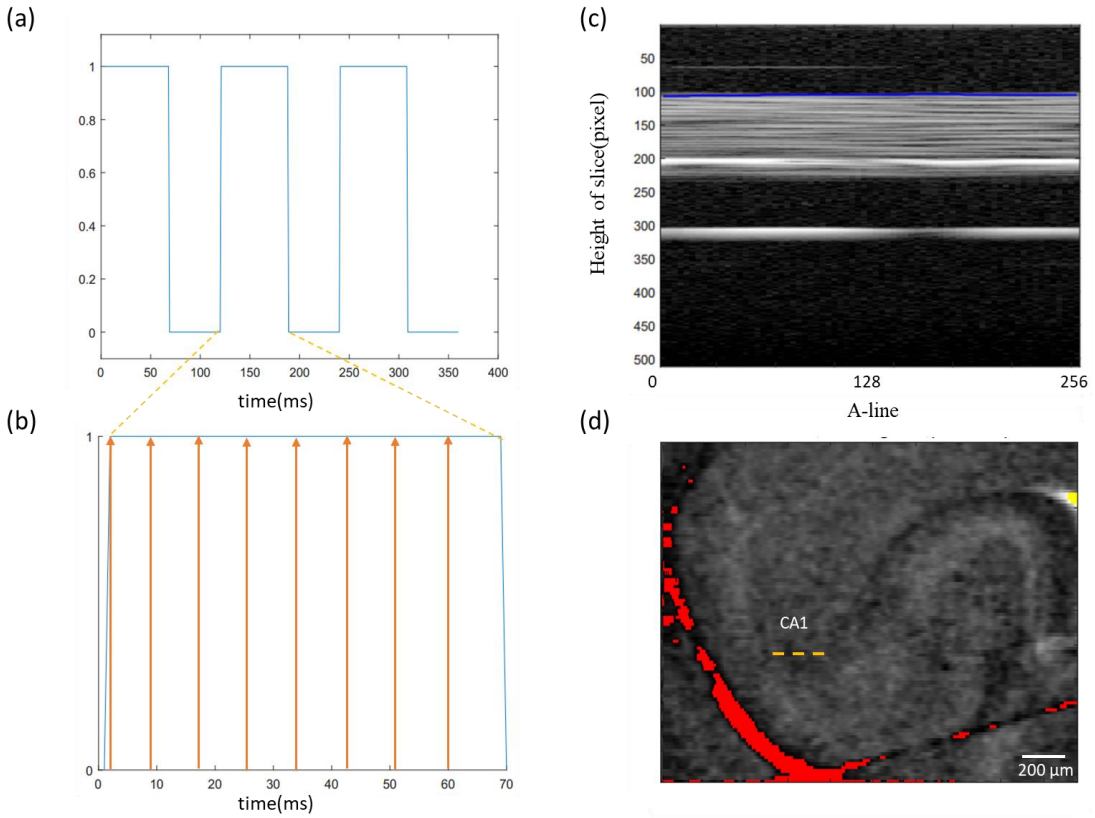

Figure 6.2 OCT data acquisition scheme. (a) Images were continuously saved for 68.2 ms, then there was gap of 51.8 ms before next acquisition [1 indicates data acquisition and 0 indicates gap]. In the acquisition period of 68.2 ms, 8 B-lines were acquired(b) with each B-line consists 256 A-lines. A single B-line(c) was taken from CA1 region(d). The red on the *en face* image(d) indicates the anchor, which was used to hold the brain slice stationary.

6.2.3.2.Electrophysiology data acquisition and processing

Multielectrode array (MEA) recordings were performed on a 60-channel perforated array (60pMEA200/30-Ti) with a low-noise amplifier (MEA1060-BC) from MultiChannel Systems. Hippocampal slices were prepared, as described above, placed on the array, and positioned such that the CA1, CA3, and dentate gyrus (DG) were centered over the recording electrodes. All ripple recordings were performed in slightly elevated extracellular potassium (5 mM KCl) to induce sharp-wave ripple complexes. All MEA recordings were performed at 32°C, which was sufficient to generate stable ripple activity.

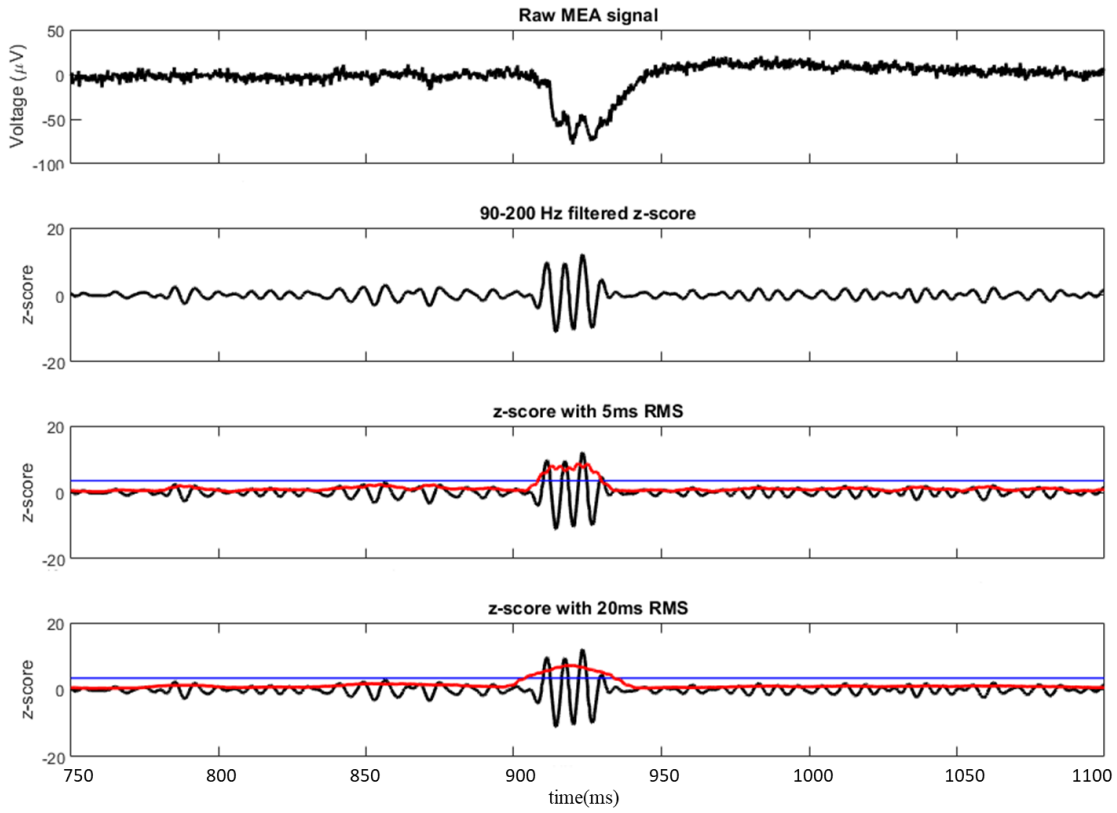

Figure 6.3 Processing of Sharp Wave Ripple. (a) LFP over time. (b) 90-200 Hz filtered z score. (c) z-score with 5 ms RMS. The red line is the envelope of ripple(RMS), and the blue line is the +3.5σ line. (d) z-score with 20 ms RMS. The red line is the envelope of ripple(RMS), and the blue line is the +3.5σ line.

Data were acquired using MC Rack software and exported to MATLAB for further processing. Data from all 60 MEA channels were collected at 10 kHz. Ripples were detected from LFP recordings from CA1 of the hippocampus by bandpass filtering (90-200 Hz 2nd order Butterworth filter), z-normalization, and finally computing the root-mean squared (RMS) of the z-normalized trace (Figure 6.3). The threshold for ripple detection was set as deviations above 3.5 standard deviation. A minimum of 20 ms and maximum of 500 ms events duration were used as exclusion criteria for ripple detection. Additionally, a none overlap period of 50 ms was used to identify individual ripples. Ripple duration was

measured from the first to last time the signal crossed the 3.5 standard deviation threshold. Inter-arrival times were computed as the difference in ripple onset times as determined by 3.5 standard deviation threshold.

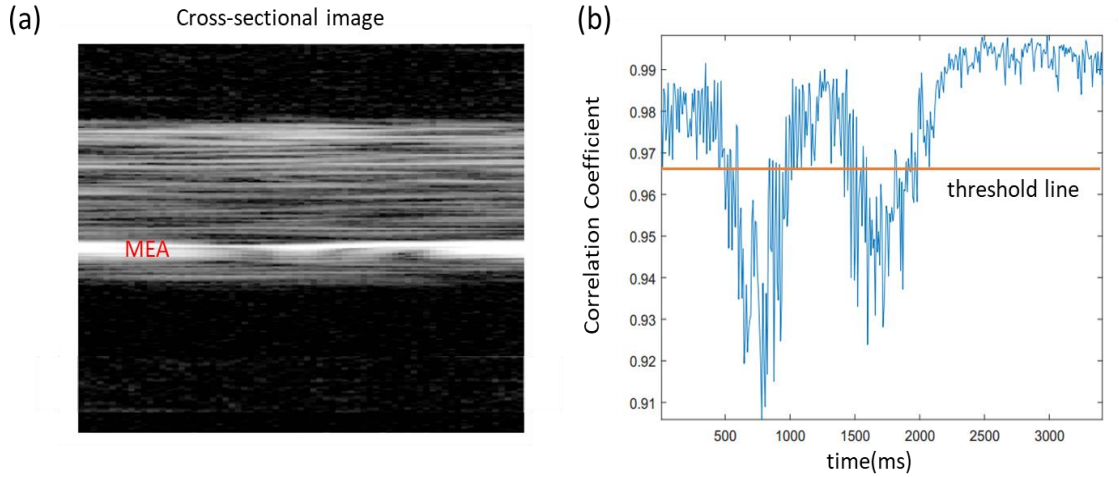

Figure 6.4 Axial motion detection. Average intensity over time, I(t) was calculated from cross-sectional images(a). Correlation coefficient was calculated between consecutive segment I(t=1 to t=N) and I(t=2 to t=N+1), where N is the segment size and so on.

6.3.Results and discussion

6.3.1.Control experiment to track axial motion of brain slice

The sample needs to be stationary over time to have an accurate intensity measurement for small intensity changes during neural. If there is a lateral motion during data acquisition, there is no way to compare activity from a time t1 with the activity from time t2 because signals are generating from different spatial locations. As the solution flow in and out from MEA well, there is a change of solution level, which causes axial motion of brain slice. There are 2 ways to detect axial motion. The first method requires detection

of the top surface of the brain slice from intensity thresholding. If the solution level changes, this also changes the intensity of top surface of the brain slice. Thus, detection of the top surface based on intensity is not a reliable method.

Another way, we can detect axial motion using cross-correlation between consecutive average intensity segment. If the average intensity over time is $I(t)$, and the selected segment length is N, then a segment of data, for example, $A = I(t = 1\ to\ t = N)$, and another segment of data, $B = I(t = 2\ to\ t = N + 1)$. The correlation coefficient is,

$$\rho(A,B) = \frac{1}{N-1}\sum_{i=1}^{N}\left(\overline{\frac{A_i - \mu_A}{\sigma_A}}\right)\left(\frac{B_i - \mu_B}{\sigma_B}\right)$$

where μ_A and σ_A are the mean and standard deviation of *A*, respectively, and μ_B and σ_B are the mean and standard deviation of *B*. The correlation coefficient was calculated for other consecutive data segments of length N and plotted over time (Figure 3b).

To check the algorithm, brain slice was moved axially in between 700 ms and 1000 ms. From Figure 6.4b, we found a decrease of correlation coefficient when there was a movement of brain slice. Another axial movement was in between 1500 ms and 2000 ms. A threshold of 0.965 was set to detect axial motion. Anytime, the correlation coefficient crosses the threshold limit, OCT data was discarded for that portion.

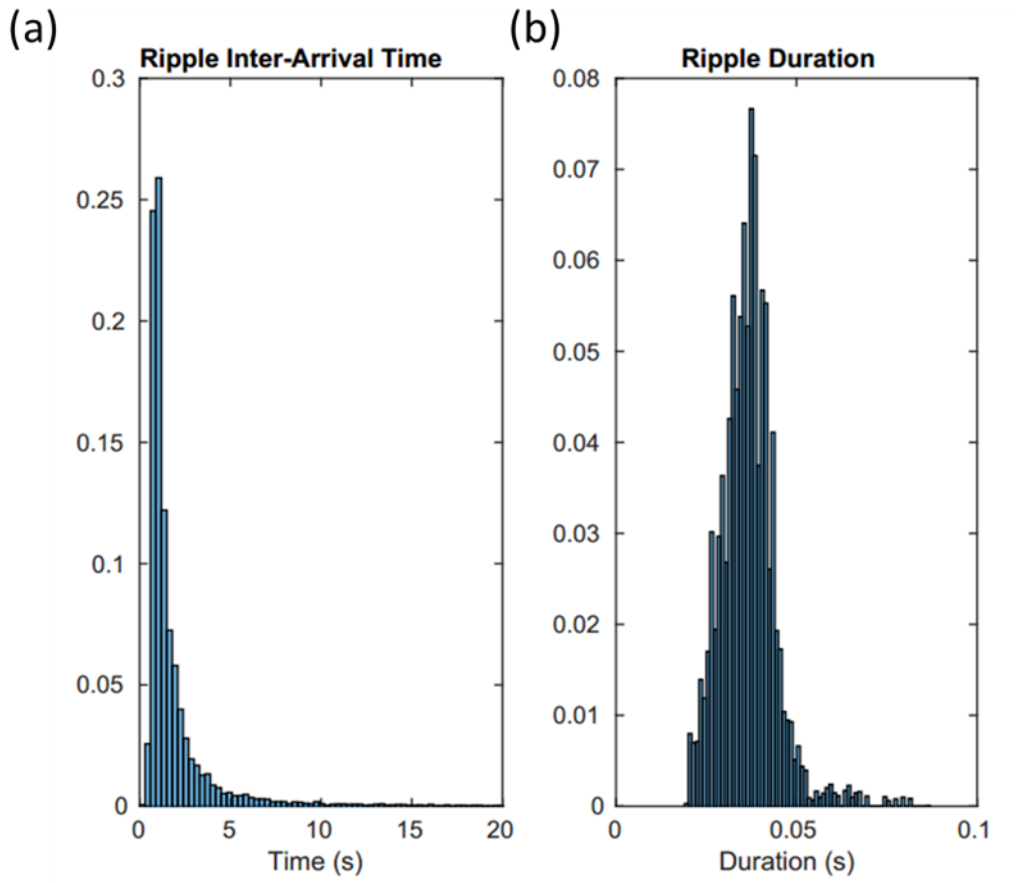

Figure 6.5 Analysis of ripple. (a) Ripple inter-arrival time. (b) the duration of ripple

6.3.2.During Sharp Wave Ripple activation

Sharp wave ripples were induced by introducing elevated KCL (5 mM), and both electrophysiology and OCT data were acquired from CA1 region simultaneously. Ripple was extracted from the electrophysiology and peak of ripple was identified. Ripple time interval (Figure 6.5a) is 2 s for more than 50% of the data and can be up to 20 s. The duration of ripple is in between 20 to 50 ms (Figure 6.5b) and median duration is 40 ms.

Ripple peak was identified from the RMS value of the z-normalized trace. As the maximum duration of the ripple 80 ms, a segment of 350 ms of data was selected by keeping peak of ripple in the middle. Corresponding OCT average intensity data was also selected for the comparison of intensity and ripple. In the 350 ms segment of OCT intensity data, there was a non-data segment too. For each 120 ms, the OCT system acquired data for 57% of the time, and other 43% time, there was no data (see Figure 6.2a) and filled with Not a Number(NaN). So, to have a true picture of OCT intensity, multiple segments need to be averaged to have a continuous segment of 350 ms.

The total number of ripple was 32, and mean intensity was calculated by excluding NaN data. Standard deviation(σ) was calculated from the first 120 ms of mean intensity data where there were no ripples. ±2σ lines were drawn from the average of the baseline (Figure 6.6a) to indicate the change of intensity for ripple activation. The -2σ line crosses the mean intensity at -0.98% of intensity.

The average was also taken for the 32 ripples. As the ripples data was acquired continuously, there was no need of nan-mean. ±2σ lines were drawn from baseline (Figure 6.6b) to indicate start and end of ripple. The -2σ line crosses RMS of z-normalized trace at 1.75(a.u.) indicating start and end of ripple.

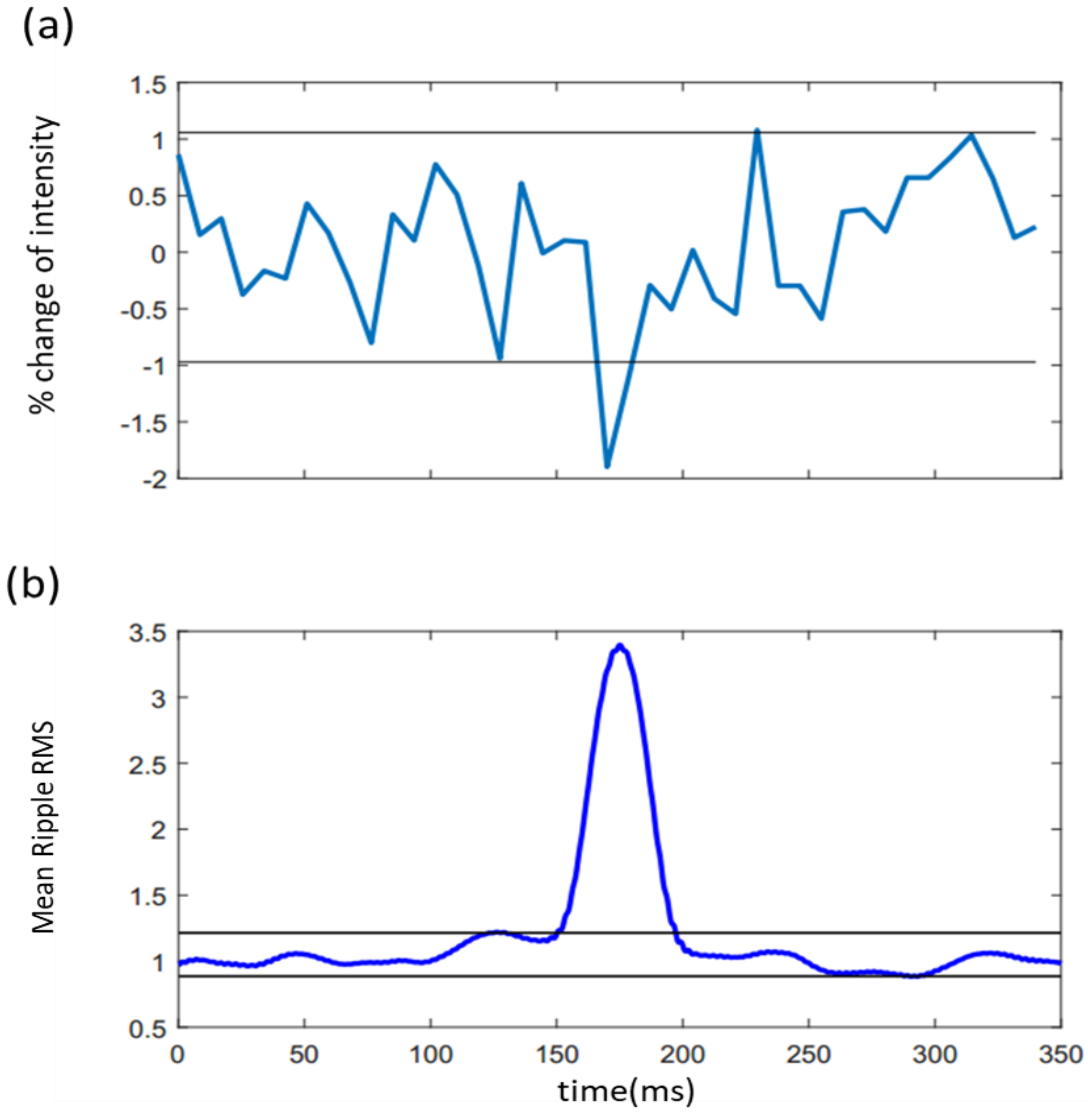

Figure 6.6 Correlation between percentage change of intensity and mean ripple RMS. (a) Average intensity of OCT intensity for 32 ripples. 2 standard deviation lines indicate the detection of ripple activation. (b) Mean Ripple RMS of 32 ripple with 2 standard deviation lines. The timing of the OCT intensity and electrophysiology signals is similar.

Figure 6.6 demonstrated that the timing of the OCT intensity and electrophysiology signals was similar. At 175th ms, ripple had its peak, and there was a decrease of OCT intensity of 1.9%. Ripple changed the optical scattering properties by changing the shape

of neurons in CA1 region. Therefore, the backscattered light that collected by OCT from CA1 region was different from baseline to ripple activation.

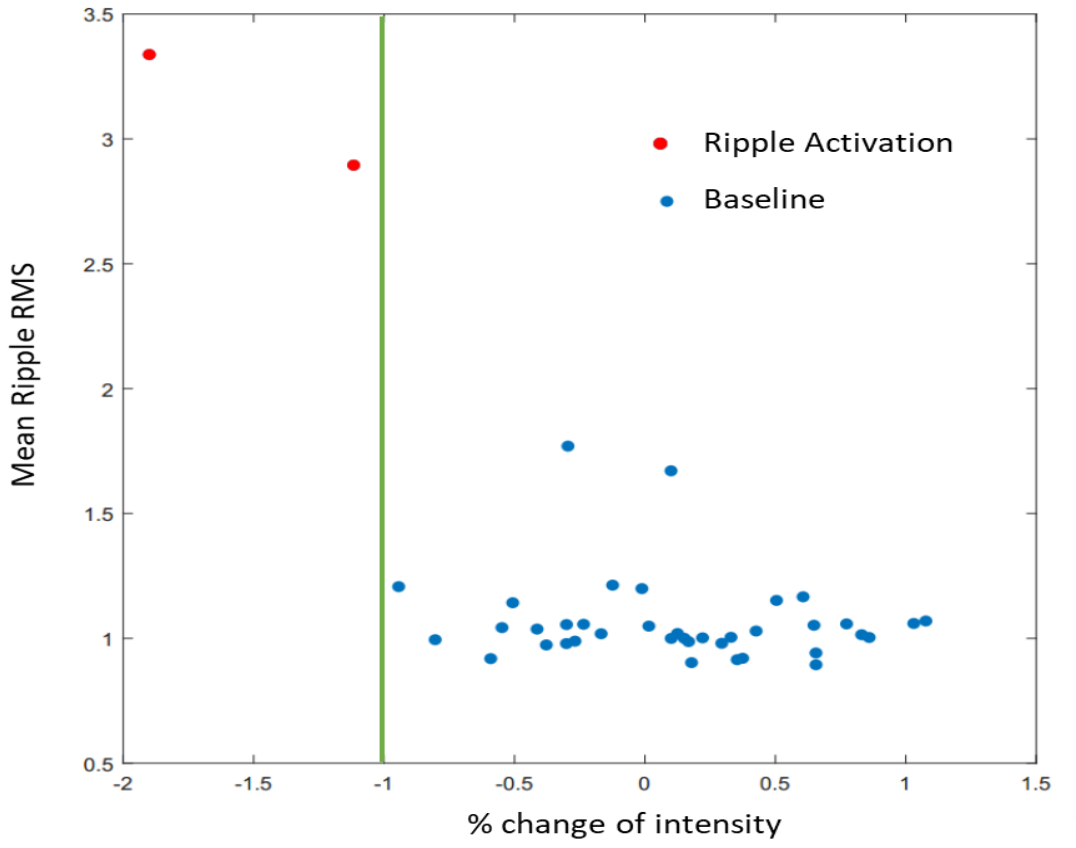

Figure 6.7 Separation of ripple activation form baseline. The vertical line at -1% intensity separate ripple from non-ripple.

Figure 6.7 demonstrated the correlation between ripple activation and OCT intensity change. The blue dots were from baseline and red dots were from ripple activation. The vertical line at %1 change of intensity separated the baseline from ripple activation.

6.4.Conclusion

SD-OCT can detect sharp wave ripple in *in vitro* mouse brain slice from the localized area of CA1 of the hippocampus. The intensity of the backscattered light decreases during ripple activation. The 1% decrease of OCT intensity from baseline indicated the activation of the ripple.

The maximum decrease of intensity is 2%, which is less than the seizure induced intensity change. We hypothesize that the change of intensity will be higher if we average many ripple activities. Then the baseline noise will be removed and the decrease of intensity will be more prominent from baseline.

Conclusion

Optical coherence tomography is a suitable method to detect neural activity without the use of exogenous agents. Nerves undergo intrinsic structural changes during neural activity. Pr-SD-OCT can detect neural activities by measuring the change in thickness of an axon during the propagation of an action potential with millisecond time resolution via phase-resolved measurements. First, we detected the swelling of the optic nerves of a functionally stimulated compound eye of a horseshoe crab *in vitro*. As lateral scanning introduced phase noise, the OCT phase data was collected by positioning the laser beam on one location of the optic nerves. The optic nerves swelled 10-30 nm during action potential propagation. In this experiment, we can visually see the axons and adjust the position of the laser beam by real-time monitoring of the cross-sectional image before acquiring phase data. Furthermore, murine brain slices were also examined *in vitro*. The diameter of these nerves is similar to the mammalian physiology relevant size of neurons. The neural activity was induced by introducing the 4-AP solution on the submerged brain slice on the MEA. Since this is a large-scale synchronized neural activity, collecting information from one location of the CA3 region of hippocampal brain slice has the signature of structural changes of neurons. The depth-resolved measurement demonstrated that the fluctuation of phase differences or thickness changes were correlated with local field potential. We also found there was a decrease of SNR during propagation of the action potential. There is an inverse relationship between SNR and phase noise. The decrease of SNR resulted in an increase of phase noise, which makes phase measurement unreliable at

low SNR. Therefore, we need to examine intensity carefully to understand the phase changes during action potential propagation. Then we moved on with the detection of optical intensity changes from the localized area of hippocampal CA1 using sharp wave ripple activation. We collected OCT intensity information from the CA1 by lateral scanning of 200 μm. In order to have a reliable measurement, a sufficient number of ripples needed to be averaged. However, obtaining a sufficient number of ripples proved to be difficult. So, a large spatial averaging during neural activity from seizure activation from 3D volumetric images was done to obtain the first careful measurements of a change of non-vascular-coupled OCT intensity/attenuation coefficient.

In order to induce neural activity without any vascular coupling, in vitro murine brain slice seizure model was used for the study. SD-OCT detected these synchronous neural activities in the hippocampus by quantifying backscattered intensity. There was a 10~18% decrease of intensity during epileptiform activity, and this decrease was spatially correlated with electrophysiology in CA1, CA3 and DG area. A threshold of -4% intensity separated activity from no-activity with 97.27% of specificity and 97.60 % of sensitivity. Attenuation coefficient, an optical property of the tissue which was invariable for similar types of tissue, was used as a biomarker and detected neural activities. There was a 10~15% decrease of attenuation coefficient from baseline, and a threshold of -6% attenuation coefficient separated neural activity from baseline with 99.5% of specificity and 95% of sensitivity. Therefore, the intensity or the attenuation coefficient can be used as a biomarker to detect neural activity.

References and Bibliography

1. Huang, D., et al., *Optical coherence tomography.* Science, 1991. **254**(5035): p. 1178-81.

2. Fercher, A.F., *Optical coherence tomography - development, principles, applications.* Z Med Phys, 2010. **20**(4): p. 251-76.

3. Clivaz, X., et al., *High-resolution reflectometry in biological tissues.* Opt Lett, 1992. **17**(1): p. 4-6.

4. Schmitt, J.M., et al., *Optical-coherence tomography of a dense tissue: statistics of attenuation and backscattering.* Phys Med Biol, 1994. **39**(10): p. 1705-20.

5. Tanno, N., et al., *Biliary lipid composition in heterozygous familial hypercholesterolemia and influence of treatment with probucol.* Dig Dis Sci, 1994. **39**(7): p. 1586-91.

6. Choma, M., et al., *Sensitivity advantage of swept source and Fourier domain optical coherence tomography.* Opt Express, 2003. **11**(18): p. 2183-9.

7. de Boer, J.F., et al., *Improved signal-to-noise ratio in spectral-domain compared with time-domain optical coherence tomography.* Opt Lett, 2003. **28**(21): p. 2067-9.

8. Leitgeb, R., C. Hitzenberger, and A. Fercher, *Performance of fourier domain vs. time domain optical coherence tomography.* Opt Express, 2003. **11**(8): p. 889-94.

9. Drexler, W. and J.G. Fujimoto, *Optical Coherence Tomography Technology and Applications Preface.* Optical Coherence Tomography: Technology and Applications, 2008: p. V-Vii.

10. Park, B., et al., *Real-time fiber-based multi-functional spectral-domain optical coherence tomography at 1.3 microm.* Opt Express, 2005. **13**(11): p. 3931-44.

11. Yazdanfar, S., et al., *Frequency estimation precision in Doppler optical coherence tomography using the Cramer-Rao lower bound.* Opt Express, 2005. **13**(2): p. 410-6.

12. Hee, M.R., et al., *Optical coherence tomography of the human retina.* Arch Ophthalmol, 1995. **113**(3): p. 325-32.

13. Hitzenberger, C., et al., *Three-dimensional imaging of the human retina by high-speed optical coherence tomography.* Opt Express, 2003. **11**(21): p. 2753-61.

14. Nassif, N., et al., *In vivo high-resolution video-rate spectral-domain optical coherence tomography of the human retina and optic nerve.* Opt Express, 2004. **12**(3): p. 367-76.

15. Gotzinger, E., M. Pircher, and C.K. Hitzenberger, *High speed spectral domain polarization sensitive optical coherence tomography of the human retina.* Opt Express, 2005. **13**(25): p. 10217-29.

16. Aguirre, A.D., et al., *Depth-resolved imaging of functional activation in the rat cerebral cortex using optical coherence tomography.* Opt Lett, 2006. **31**(23): p. 3459-61.

17. Lim, H., et al., *High-speed imaging of human retina in vivo with swept-source optical coherence tomography.* Opt Express, 2006. **14**(26): p. 12902-8.

18. Huber, R., et al., *Fourier domain mode locking at 1050 nm for ultra-high-speed optical coherence tomography of the human retina at 236,000 axial scans per second.* Opt Lett, 2007. **32**(14): p. 2049-51.

19. Fernandez, E.J., et al., *Ultrahigh resolution optical coherence tomography and pancorrection for cellular imaging of the living human retina.* Opt Express, 2008. **16**(15): p. 11083-94.

20. Fingler, J., et al., *Volumetric microvascular imaging of human retina using optical coherence tomography with a novel motion contrast technique.* Opt Express, 2009. **17**(24): p. 22190-200.

21. Torti, C., et al., *Adaptive optics optical coherence tomography at 120,000 depth scans/s for non-invasive cellular phenotyping of the living human retina.* Opt Express, 2009. **17**(22): p. 19382-400.

22. Granstedt, A.E., et al., *Fluorescence-based monitoring of in vivo neural activity using a circuit-tracing pseudorabies virus.* PLoS One, 2009. **4**(9): p. e6923.

23. Wang, R.K. and L. An, *Multifunctional imaging of human retina and choroid with 1050-nm spectral domain optical coherence tomography at 92-kHz line scan rate.* J Biomed Opt, 2011. **16**(5): p. 050503.

24. Choi, W., et al., *Phase-sensitive swept-source optical coherence tomography imaging of the human retina with a vertical cavity surface-emitting laser light source.* Opt Lett, 2013. **38**(3): p. 338-40.

25. Santos, M., et al., *Simulation of cellular changes on Optical Coherence Tomography of human retina.* Conf Proc IEEE Eng Med Biol Soc, 2015. **2015**: p. 8147-50.

26. Sugita, M., et al., *Analysis of optimum conditions of depolarization imaging by polarization-sensitive optical coherence tomography in the human retina.* J Biomed Opt, 2015. **20**(1): p. 016011.

27. Campbell, J.P., et al., *Detailed Vascular Anatomy of the Human Retina by Projection-Resolved Optical Coherence Tomography Angiography.* Sci Rep, 2017. **7**: p. 42201.

28. Cense, B., et al., *Measuring polarization changes in the human outer retina with polarization-sensitive optical coherence tomography.* J Biophotonics, 2017.

29. Mansoori, T., et al., *Measurement of Radial Peripapillary Capillary Density in the Normal Human Retina Using Optical Coherence Tomography Angiography.* J Glaucoma, 2017. **26**(3): p. 241-246.

30. Theelen, T. and M.M. Teussink, *Inspection of the Human Retina by Optical Coherence Tomography.* Methods Mol Biol, 2018. **1715**: p. 351-358.

31. Boppart, S.A., *Optical coherence tomography: technology and applications for neuroimaging.* Psychophysiology, 2003. **40**(4): p. 529-41.

32. Valenti, D.A., *Neuroimaging of retinal nerve fiber layer in AD using optical coherence tomography.* Neurology, 2007. **69**(10): p. 1060.

33. Regar, E., J. Schaar, and P.W. Serruys, *Images in cardiology. Acute recoil in sirolimus eluting stent: real time, in vivo assessment with optical coherence tomography.* Heart, 2006. **92**(1): p. 123.

34. Picchi, A., A. Micheli, and U. Limbruno, *Images in cardiology. The traumatic effect of balloon dilatation on neointimal hyperplasia: what we did not see before optical coherence tomography.* Heart, 2011. **97**(3): p. 265-6.

35. Tereshchenko, A.S., et al., *[Basic principles of optical coherence tomography in interventional cardiology].* Vestn Rentgenol Radiol, 2013(6): p. 67-72.

36. Yonetsu, T., et al., *Optical coherence tomography- 15 years in cardiology.* Circ J, 2013. **77**(8): p. 1933-40.

37. Vignali, L., E. Solinas, and E. Emanuele, *Research and clinical applications of optical coherence tomography in invasive cardiology: a review.* Curr Cardiol Rev, 2014. **10**(4): p. 369-76.

38. Baumgartner, A., et al., *Polarization-sensitive optical coherence tomography of dental structures.* Caries Res, 2000. **34**(1): p. 59-69.

39. Otis, L.L., et al., *Dental optical coherence tomography: a comparison of two in vitro systems.* Dentomaxillofac Radiol, 2000. **29**(2): p. 85-9.

40. de Melo, L.S., et al., *Evaluation of enamel dental restoration interface by optical coherence tomography.* J Biomed Opt, 2005. **10**(6): p. 064027.

41. Hsieh, Y.S., et al., *Dental optical coherence tomography.* Sensors (Basel), 2013. **13**(7): p. 8928-49.

42. Lee, S.H., et al., *Dental optical coherence tomography: new potential diagnostic system for cracked-tooth syndrome.* Surg Radiol Anat, 2016. **38**(1): p. 49-54.

43. Watanabe, H., et al., *Resolution characteristics of optical coherence tomography for dental use.* Dentomaxillofac Radiol, 2017. **46**(3): p. 20160358.

44. Welzel, J., *Optical coherence tomography in dermatology: a review.* Skin Res Technol, 2001. **7**(1): p. 1-9.

45. Alex, A., et al., *Three-dimensional multiphoton/optical coherence tomography for diagnostic applications in dermatology.* J Biophotonics, 2013. **6**(4): p. 352-62.

46. Ulrich, M., et al., *Dynamic Optical Coherence Tomography in Dermatology.* Dermatology, 2016. **232**(3): p. 298-311.

47. Schwartz, M., A. Levine, and O. Markowitz, *Optical coherence tomography in dermatology.* Cutis, 2017. **100**(3): p. 163-166.

48. Boppart, S.A., M.E. Brezinski, and J.G. Fujimoto, *Optical coherence tomography imaging in developmental biology.* Methods Mol Biol, 2000. **135**: p. 217-33.

49. Agrawal, A., et al., *Optic Nerve Head Measurements With Optical Coherence Tomography: A Phantom-Based Study Reveals Differences Among Clinical Devices.* Investigative Ophthalmology & Visual Science, 2016. **57**(9): p. Oct413-Oct420.

50. Mason, C., et al., *Doppler optical coherence tomography for measuring flow in engineered tissue.* Biosensors & Bioelectronics, 2004. **20**(3): p. 414-423.

51. Boppart, S.A., Y. Yang, and R.K. Wang, *Optical Coherence Tomography in Tissue Engineering.* Optical Coherence Tomography: Technology and Applications, 2008: p. 889-917.

52. Gurjarpadhye, A.A., et al., *Dynamic Assessment of the Endothelialization of Tissue-Engineered Blood Vessels Using an Optical Coherence Tomography Catheter-Based Fluorescence Imaging System.* Tissue Engineering Part C-Methods, 2015. **21**(7): p. 758-766.

53. Kagawa, Y., et al., *Real-time quantitation of internal metabolic activity of three-dimensional engineered tissues using an oxygen microelectrode and optical coherence tomography.* Journal of Biomedical Materials Research Part B-Applied Biomaterials, 2017. **105**(4): p. 855-864.

54. Mehta, R., et al., *Wireless, Web-Based Interactive Control of Optical Coherence Tomography with Mobile Devices.* Translational Vision Science & Technology, 2017. **6**(1).

55. Dichtl, S., et al., *Imaging of dental material by polarization sensitive optical coherence tomography.* Lasers in Dentistry V, Proceedings Of, 1999. **3593**: p. 169-176.

56. Stifter, D., et al., *Polarisation-sensitive optical coherence tomography for material characterisation and strain-field mapping.* Applied Physics a-Materials Science & Processing, 2003. **76**(6): p. 947-951.

57. Stifter, D., et al., *Investigation of polymer and polymer/fibre composite materials with optical coherence tomography.* Measurement Science and Technology, 2008. **19**(7).

58. Qin, Y.W. and H. Zhao, *Spectral-domain Optical Coherence Tomography for Material Detection.* Manufacturing Engineering and Automation Ii, Pts 1-3, 2012. **591-593**: p. 1139-1142.

59. Hutiu, G., et al., *Surface imaging of metallic material fractures using optical coherence tomography.* Applied Optics, 2014. **53**(26): p. 5912-5916.

60. Rollins, A., et al., *In vivo video rate optical coherence tomography.* Opt Express, 1998. **3**(6): p. 219-29.

61. Laubscher, M., et al., *Video-rate three-dimensional optical coherence tomography.* Opt Express, 2002. **10**(9): p. 429-35.

62. Akiba, M. and K.P. Chan, *In vivo video-rate cellular-level full-field optical coherence tomography.* J Biomed Opt, 2007. **12**(6): p. 064024.

63. Kaluzny, B.J., et al., *Spectral optical coherence tomography in video-rate and 3D imaging of contact lens wear.* Optom Vis Sci, 2007. **84**(12): p. 1104-9.

64. Hidalgo-Aguirre, M., et al., *Automatic segmentation of the optic nerve head for deformation measurements in video rate optical coherence tomography.* J Biomed Opt, 2015. **20**(11): p. 116008.

65. Hendel, T., et al., *Fluorescence changes of genetic calcium indicators and OGB-1 correlated with neural activity and calcium in vivo and in vitro.* J Neurosci, 2008. **28**(29): p. 7399-411.

66. Holekamp, T.F., D. Turaga, and T.E. Holy, *Fast three-dimensional fluorescence imaging of activity in neural populations by objective-coupled planar illumination microscopy.* Neuron, 2008. **57**(5): p. 661-72.

67. Hayashi, Y., et al., *Spatio-temporal control of neural activity in vivo using fluorescence microendoscopy.* Eur J Neurosci, 2012. **36**(6): p. 2722-32.

68. Sinha, S., et al., *High-speed laser microsurgery of alert fruit flies for fluorescence imaging of neural activity.* Proc Natl Acad Sci U S A, 2013. **110**(46): p. 18374-9.

69. Friman, O., et al., *Detection of neural activity in fMRI using maximum correlation modeling.* Neuroimage, 2002. **15**(2): p. 386-95.

70. Chevrier, A., M.D. Noseworthy, and R. Schachar, *Neural activity associated with failed inhibition: an event related fMRI study or performance monitoring.* Brain Cogn, 2004. **54**(2): p. 163-5.

71. Lee, T.M., et al., *Neural activity associated with cognitive regulation in heroin users: A fMRI study.* Neurosci Lett, 2005. **382**(3): p. 211-6.

72. Olson, I.R., et al., *Using perfusion fMRI to measure continuous changes in neural activity with learning.* Brain Cogn, 2006. **60**(3): p. 262-71.

73. Ekstrom, A., *How and when the fMRI BOLD signal relates to underlying neural activity: the danger in dissociation.* Brain Res Rev, 2010. **62**(2): p. 233-44.

74. Ohye, C., et al., *Stereotactic CT scan and its correlation with the neural activity of deep structures.* Appl Neurophysiol, 1980. **43**(3-5): p. 183-8.

75. Tagamets, M.A. and B. Horwitz, *Interpreting PET and fMRI measures of functional neural activity: the effects of synaptic inhibition on cortical activation in human imaging studies.* Brain Res Bull, 2001. **54**(3): p. 267-73.

76. Horwitz, B., *Relating fMRI and PET signals to neural activity by means of large-scale neural models.* Neuroinformatics, 2004. **2**(2): p. 251-66.

77. Lockwood, A.H., et al., *Multi-site phasic neural activity mediates the execution of an auditory continuous performance task: a PET and electrophysiological study.* J Neuroimaging, 2008. **18**(4): p. 364-74.

78. Jimbo, Y., *Recording neural activity by electrode-array substrates.* Electrochemistry, 1999. **67**(3): p. 276-279.

79. Jayaraman, V. and G. Laurent, *Evaluating a genetically encoded optical sensor of neural activity using electrophysiology in intact adult fruit flies.* Front Neural Circuits, 2007. **1**: p. 3.

80. Panetsos, F. and C. Avendano, *Neural activity of the Central Nervous System after long-term implants of sieve-electrodes to the peripheral nerves.* 2007 3rd International Ieee/Embs Conference on Neural Engineering, Vols 1 and 2, 2007: p. 44-+.

81. Shew, W.L., T. Bellay, and D. Plenz, *Simultaneous multi-electrode array recording and two-photon calcium imaging of neural activity.* Journal of Neuroscience Methods, 2010. **192**(1): p. 75-82.

82. Gage, G.J., et al., *Surgical Implantation of Chronic Neural Electrodes for Recording Single Unit Activity and Electrocorticographic Signals.* Jove-Journal of Visualized Experiments, 2012(60).

83. Kondo, Y., et al., *Temporal relation between neural activity and neurite pruning on a numerical model and a microchannel device with micro electrode array.* Biochemical and Biophysical Research Communications, 2017. **486**(2): p. 539-544.

84. Yang, J., et al., *Fast multispectral diffuse optical tomography system for in vivo three-dimensional imaging of seizure dynamics.* Appl Opt, 2012. **51**(16): p. 3461-9.

85. Zhang, T., et al., *Pre-seizure state identified by diffuse optical tomography.* Sci Rep, 2014. **4**: p. 3798.

86. Chen, J.W., A.M. O'Farrell, and A.W. Toga, *Optical intrinsic signal imaging in a rodent seizure model.* Neurology, 2000. **55**(2): p. 312-5.

87. Lu, R.W., Q.X. Zhang, and X.C. Yao, *Circular polarization intrinsic optical signal recording of stimulus-evoked neural activity.* Opt Lett, 2011. **36**(10): p. 1866-8.

88. Zhan, C.A., T. Ledgeway, and C.L. Baker, Jr., *Contrast response in visual cortex: quantitative assessment with intrinsic optical signal imaging and neural firing.* Neuroimage, 2005. **26**(2): p. 330-46.

89. Liu, W., et al., *OCT-Angiography for Non-Invasive Monitoring of Neuronal and Vascular Structure in Mouse Retina: Implication for Characterization of Retinal Neurovascular Coupling.* EC Ophthalmol, 2017. **5**(3): p. 89-98.

90. Bodenschatz, N., et al., *Detecting structural information of scatterers using spatial frequency domain imaging.* J Biomed Opt, 2015. **20**(11): p. 116006.

91. Singh-Moon, R.P., et al., *Spatial mapping of drug delivery to brain tissue using hyperspectral spatial frequency-domain imaging.* J Biomed Opt, 2014. **19**(9): p. 96003.

92. Lazebnik, M., et al., *Functional optical coherence tomography for detecting neural activity through scattering changes.* Opt Lett, 2003. **28**(14): p. 1218-20.

93. Yao, X.C., et al., *Rapid optical coherence tomography and recording functional scattering changes from activated frog retina.* Appl Opt, 2005. **44**(11): p. 2019-23.

94. Graf, B.W., et al., *Detecting intrinsic scattering changes correlated to neuron action potentials using optical coherence imaging.* Opt Express, 2009. **17**(16): p. 13447-57.

95. Yeh, Y.J., et al., *Optical coherence tomography for cross-sectional imaging of neural activity.* Neurophotonics, 2015. **2**(3): p. 035001.

96. Akkin, T., et al., *Detection of neural activity using phase-sensitive optical low-coherence reflectometry.* Opt Express, 2004. **12**(11): p. 2377-86.

97. Akkin, T., C. Joo, and J.F. de Boer, *Depth-resolved measurement of transient structural changes during action potential propagation.* Biophys J, 2007. **93**(4): p. 1347-53.

98. Chen, Y., et al., *Optical coherence tomography (OCT) reveals depth-resolved dynamics during functional brain activation.* J Neurosci Methods, 2009. **178**(1): p. 162-73.

99. Akkin, T., D. Landowne, and A. Sivaprakasam, *Detection of Neural Action Potentials Using Optical Coherence Tomography: Intensity and Phase Measurements with and without Dyes.* Front Neuroenergetics, 2010. **2**.

100. Tong, M.Q., et al., *OCT intensity and phase fluctuations correlated with activity-dependent neuronal calcium dynamics in the Drosophila CNS [Invited]*. Biomedical Optics Express, 2017. **8**(2): p. 726-735.

101. Bizheva, K., et al., *Imaging ex vivo healthy and pathological human brain tissue with ultra-high-resolution optical coherence tomography.* J Biomed Opt, 2005. **10**(1): p. 11006.

102. Bohringer, H.J., et al., *Time-domain and spectral-domain optical coherence tomography in the analysis of brain tumor tissue.* Lasers Surg Med, 2006. **38**(6): p. 588-97.

103. Osiac, E., et al., *Optical coherence tomography as a promising imaging tool for brain investigations.* Rom J Morphol Embryol, 2014. **55**(2 Suppl): p. 507-12.

104. Kut, C., et al., *Detection of human brain cancer infiltration ex vivo and in vivo using quantitative optical coherence tomography.* Sci Transl Med, 2015. **7**(292): p. 292ra100.

105. Fisher, R.S., et al., *Epileptic seizures and epilepsy: definitions proposed by the International League Against Epilepsy (ILAE) and the International Bureau for Epilepsy (IBE).* Epilepsia, 2005. **46**(4): p. 470-2.

106. Jiruska, P., et al., *Synchronization and desynchronization in epilepsy: controversies and hypotheses.* J Physiol, 2013. **591**(4): p. 787-97.

107. Chen, G.Y., *Automatic EEG seizure detection using dual-tree complex wavelet-Fourier features.* Expert Systems with Applications, 2014. **41**(5): p. 2391-2394.

108. Buzsaki, G., *Hippocampal sharp wave-ripple: A cognitive biomarker for episodic memory and planning.* Hippocampus, 2015. **25**(10): p. 1073-188.

109. Tzallas, A.T., M.G. Tsipouras, and D.I. Fotiadis, *Epileptic Seizure Detection in EEGs Using Time-Frequency Analysis.* Ieee Transactions on Information Technology in Biomedicine, 2009. **13**(5): p. 703-710.

110. Gotman, J. and F. Pittau, *Combining EEG and fMRI in the study of epileptic discharges.* Epilepsia, 2011. **52 Suppl 4**: p. 38-42.

111. Guo, L., et al., *Cognitive Functioning in Temporal Lobe Epilepsy: A BOLD-fMRI Study.* Mol Neurobiol, 2017. **54**(10): p. 8361-8369.

112. Salek-Haddadi, A., et al., *Hemodynamic correlates of epileptiform discharges: an EEG-fMRI study of 63 patients with focal epilepsy.* Brain Res, 2006. **1088**(1): p. 148-66.

113. Yang, H., et al., *In vivo imaging of epileptic foci in rats using a miniature probe integrating diffuse optical tomography and electroencephalographic source localization.* Epilepsia, 2015. **56**(1): p. 94-100.

114. Bahar, S., et al., *Intrinsic optical signal imaging of neocortical seizures: the 'epileptic dip'.* Neuroreport, 2006. **17**(5): p. 499-503.

115. Chen, J.W.Y. and A.W. Toga, *Optical intrinsic signal imaging of acute neocortical seizures in rats.* Epilepsia, 2005. **46**: p. 202-202.

116. Schwartz, T.H. and T. Bonhoeffer, *In vivo optical mapping of epileptic foci and surround inhibition in ferret cerebral cortex.* Nature Medicine, 2001. **7**(9): p. 1063-1067.

117. An, L., et al., *High speed spectral domain optical coherence tomography for retinal imaging at 500,000 Alines per second.* Biomed Opt Express, 2011. **2**(10): p. 2770-83.

118. Leitgeb, R., et al., *Ultrahigh resolution Fourier domain optical coherence tomography.* Opt Express, 2004. **12**(10): p. 2156-65.

119. Wojtkowski, M., et al., *Ultrahigh-resolution, high-speed, Fourier domain optical coherence tomography and methods for dispersion compensation.* Opt Express, 2004. **12**(11): p. 2404-22.

120. Yun, S., et al., *High-speed spectral-domain optical coherence tomography at 1.3 mum wavelength.* Opt Express, 2003. **11**(26): p. 3598-604.

121. Bizheva, K., et al., *Imaging ex vivo and in vitro brain morphology in animal models with ultrahigh resolution optical coherence tomography.* J Biomed Opt, 2004. **9**(4): p. 719-24.

122. Xu, C., et al., *Characterization of atherosclerosis plaques by measuring both backscattering and attenuation coefficients in optical coherence tomography.* J Biomed Opt, 2008. **13**(3): p. 034003.

123. Campbell, C.E., et al., *The transcription factor Nfix is essential for normal brain development.* BMC Dev Biol, 2008. **8**: p. 52.

124. Vermeer, K.A., et al., *Depth-resolved model-based reconstruction of attenuation coefficients in optical coherence tomography.* Biomed Opt Express, 2013. **5**(1): p. 322-37.

125. Faber, D., et al., *Quantitative measurement of attenuation coefficients of weakly scattering media using optical coherence tomography.* Opt Express, 2004. **12**(19): p. 4353-65.

126. Lee, P., W. Gao, and X. Zhang, *Performance of single-scattering model versus multiple-scattering model in the determination of optical properties of biological tissue with optical coherence tomography.* Appl Opt, 2010. **49**(18): p. 3538-44.

127. Cohen, L.B., *Changes in neuron structure during action potential propagation and synaptic transmission.* Physiol Rev, 1973. **53**(2): p. 373-418.

128. Neher, E. and B. Sakmann, *Single-channel currents recorded from membrane of denervated frog muscle fibres.* Nature, 1976. **260**(5554): p. 799-802.

129. Scanziani, M. and M. Hausser, *Electrophysiology in the age of light.* Nature, 2009. **461**(7266): p. 930-9.

130. Spira, M.E. and A. Hai, *Multi-electrode array technologies for neuroscience and cardiology.* Nat Nanotechnol, 2013. **8**(2): p. 83-94.

131. Valenza, G., et al., *Stochastic modeling of spontaneous bursting activity to simulate neural responses of in-vitro networks on multielectrode arrays.* Conf Proc IEEE Eng Med Biol Soc, 2016. **2016**: p. 1616-1619.

132. Fromherz, P. and C.O. Muller, *Voltage-sensitive fluorescence of amphiphilic hemicyanine dyes in neuron membrane.* Biochim Biophys Acta, 1993. **1150**(2): p. 111-22.

133. Hill, B.C., et al., *Laser interferometer measurement of changes in crayfish axon diameter concurrent with action potential.* Science, 1977. **196**(4288): p. 426-8.

134. Hill, D.K., *The volume change resulting from stimulation of a giant nerve fibre.* J Physiol, 1950. **111**(3-4): p. 304-27.

135. Iwasa, K., I. Tasaki, and R.C. Gibbons, *Swelling of nerve fibers associated with action potentials.* Science, 1980. **210**(4467): p. 338-9.

136. Tasaki, I. and P.M. Byrne, *Volume expansion of nonmyelinated nerve fibers during impulse conduction.* Biophys J, 1990. **57**(3): p. 633-5.

137. Tasaki, I., K. Kusano, and P.M. Byrne, *Rapid mechanical and thermal changes in the garfish olfactory nerve associated with a propagated impulse.* Biophys J, 1989. **55**(6): p. 1033-40.

138. Yao, X.C., D.M. Rector, and J.S. George, *Optical lever recording of displacements from activated lobster nerve bundles and Nitella internodes.* Appl Opt, 2003. **42**(16): p. 2972-8.

139. Akkin, T., D. Landowne, and A. Sivaprakasam, *Optical coherence tomography phase measurement of transient changes in squid giant axons during activity.* J Membr Biol, 2009. **231**(1): p. 35-46.

140. Fang-Yen, C., et al., *Noncontact measurement of nerve displacement during action potential with a dual-beam low-coherence interferometer.* Opt Lett, 2004. **29**(17): p. 2028-30.

141. Nunnemacher, R.F. and P.P. Davis, *The fine structure of the limulus optic nerve.* J Morphol, 1968. **125**(1): p. 61-70.

142. Hodgkiss, J.P. and H.M. McIlroy, *The conduction velocity, number, and diameter of unmyelinated fibers in Remak's nerve.* Experientia, 1985. **41**(7): p. 919-21.

143. Pollak, V.A., et al., *Non-invasive determination of the distribution of the conduction velocity of the large-diameter fibers in peripheral nerves. Estimate based upon a single recording of the stimulus response of the nerve.* Med Prog Technol, 1992. **18**(4): p. 217-25.

144. Park, B.H., et al., *Real-time fiber-based multi-functional spectral-domain optical coherence tomography at 1.3 mu m.* Optics Express, 2005. **13**(11): p. 3931-3944.

145. Gopal, R., et al., *Electrospun nanofibrous filtration membrane.* Journal of Membrane Science, 2006. **281**(1-2): p. 581-586.

146. Choi, S.W., et al., *Characterization of electrospun PVdF fiber-based polymer electrolytes.* Chemistry of Materials, 2007. **19**(1): p. 104-115.

147. Fang, J., et al., *Applications of electrospun nanofibers.* Chinese Science Bulletin, 2008. **53**(15): p. 2265-2286.

148. Alici, G. and N.N. Huynh, *Predicting force output of trilayer polymer actuators.* Sensors and Actuators a-Physical, 2006. **132**(2): p. 616-625.

149. Boyd TE, E.H., *Studies on cold block in nerve I. Block with and without freezing.* American Journal of Physiology, 1934. **107**(1): p. 76-84.

150. Boyd TE, G.R., *The effect of prolonged activity on the irritability of medullated nerve.* American Journal of Physiology, 1930. **92**(3): p. 656-64.

151. Belardetti, F., S. Schacher, and S.A. Siegelbaum, *Action potentials, macroscopic and single channel currents recorded from growth cones of Aplysia neurones in culture.* J Physiol, 1986. **374**: p. 289-313.

152. Gruol, D.L., T. Jacquin, and A.J. Yool, *Single-channel K+ currents recorded from the somatic and dendritic regions of cerebellar Purkinje neurons in culture.* J Neurosci, 1991. **11**(4): p. 1002-15.

153. Peres, A. and G. Mostacciuolo, *Single- and multi-channel currents recorded with patch electrodes in mouse eggs.* Cell Biol Int Rep, 1987. **11**(6): p. 487-93.

154. Rojas, L. and C. Zuazaga, *Single acetylcholine channel currents recorded from Xenopus myocytes are influenced by the glass of the patch pipette.* P R Health Sci J, 1988. **7**(2): p. 78-80.

155. Tian, L., et al., *Imaging neural activity in worms, flies and mice with improved GCaMP calcium indicators.* Nat Methods, 2009. **6**(12): p. 875-81.

156. Cardenas, D.P., et al., *Functional MRI during hyperbaric oxygen: Effects of oxygen on neurovascular coupling and BOLD fMRI signals.* Neuroimage, 2015. **119**: p. 382-9.

157. Blicher, J.U., et al., *Visualization of altered neurovascular coupling in chronic stroke patients using multimodal functional MRI.* J Cereb Blood Flow Metab, 2012. **32**(11): p. 2044-54.

158. Sander, C.Y., et al., *Neurovascular coupling to D2/D3 dopamine receptor occupancy using simultaneous PET/functional MRI.* Proc Natl Acad Sci U S A, 2013. **110**(27): p. 11169-74.

159. Hill, D.K. and R.D. Keynes, *Opacity changes in stimulated nerve.* J Physiol, 1949. **108**(3): p. 278-81.

160. Sandlin, R., et al., *Application of laser interferometry to physiological studies of excitable tissues.* Nature, 1968. **217**(5128): p. 575-6.

161. Barazany, D., P.J. Basser, and Y. Assaf, *In vivo measurement of axon diameter distribution in the corpus callosum of rat brain.* Brain, 2009. **132**(Pt 5): p. 1210-20.

162. Buzsaki, G., *Hippocampal sharp waves: their origin and significance.* Brain Res, 1986. **398**(2): p. 242-52.

163. Buzsaki, G. and E. Eidelberg, *Phase relations of hippocampal projection cells and interneurons to theta activity in the anesthetized rat.* Brain Res, 1983. **266**(2): p. 334-9.

164. Buzsaki, G., et al., *High-frequency network oscillation in the hippocampus.* Science, 1992. **256**(5059): p. 1025-7.

165. O'Keefe, J., *Place units in the hippocampus of the freely moving rat.* Exp Neurol, 1976. **51**(1): p. 78-109.

166. Ylinen, A., et al., *Sharp wave-associated high-frequency oscillation (200 Hz) in the intact hippocampus: network and intracellular mechanisms.* J Neurosci, 1995. **15**(1 Pt 1): p. 30-46.

167. Chrobak, J.J. and G. Buzsaki, *Selective activation of deep layer (V-VI) retrohippocampal cortical neurons during hippocampal sharp waves in the behaving rat.* J Neurosci, 1994. **14**(10): p. 6160-70.

168. Karlocai, M.R., et al., *Physiological sharp wave-ripples and interictal events in vitro: what's the difference?* Brain, 2014. **137**(Pt 2): p. 463-85.

169. Sullivan, D., et al., *Relationships between Hippocampal Sharp Waves, Ripples, and Fast Gamma Oscillation: Influence of Dentate and Entorhinal Cortical Activity.* Journal of Neuroscience, 2011. **31**(23): p. 8605-8616.

170. Suzuki, S.S. and G.K. Smith, *Spontaneous EEG spikes in the normal hippocampus. V. Effects of ether, urethane, pentobarbital, atropine, diazepam and bicuculline.* Electroencephalogr Clin Neurophysiol, 1988. **70**(1): p. 84-95.

171. Buzsaki, G., et al., *The grafted hippocampus: an epileptic focus.* Exp Neurol, 1989. **105**(1): p. 10-22.

172. Traub, R.D., et al., *Cellular mechanisms of neuronal population oscillations in the hippocampus in vitro.* Annu Rev Neurosci, 2004. **27**: p. 247-78.

173. Norimoto, H., et al., *Subicular activation preceding hippocampal ripples in vitro.* Sci Rep, 2013. **3**: p. 2696.

174. Ramirez-Villegas, J.F., N.K. Logothetis, and M. Besserve, *Diversity of sharp-wave-ripple LFP signatures reveals differentiated brain-wide dynamical events.* Proc Natl Acad Sci U S A, 2015. **112**(46): p. E6379-87.

175. Chu, C.J., et al., *A semi-automated method for rapid detection of ripple events on interictal voltage discharges in the scalp electroencephalogram.* J Neurosci Methods, 2017. **277**: p. 46-55.

176. Hussain, S.A., et al., *Prospective and "live" fast ripple detection and localization in the operating room: Impact on epilepsy surgery outcomes in children.* Epilepsy Res, 2016. **127**: p. 344-351.

177. Sethi, A. and C. Kemere, *Real time algorithms for sharp wave ripple detection.* Conf Proc IEEE Eng Med Biol Soc, 2014. **2014**: p. 2637-40.

178. Shimamoto, S., et al., *Utilization of independent component analysis for accurate pathological ripple detection in intracranial EEG recordings recorded extra- and intra-operatively*. Clin Neurophysiol, 2018. **129**(1): p. 296-307.

179. Yaqoob, Z., J. Wu, and C. Yang, *Spectral domain optical coherence tomography: a better OCT imaging strategy*. Biotechniques, 2005. **39**(6 Suppl): p. S6-13.